UNIVERSITY OF ZURICH

# Characterisation of Inverted Coaxial Detectors and Calibration Source Production for the GERDA Experiment

*Author:*
Michael Miloradovic

*PhD Committee:*
Prof. Dr. Laura Baudis
Prof. Dr. Nicola Serra
Dr. Roman Hiller

PHD THESIS IN PARTICLE PHYSICS

Department of Physics UZH
Faculty of Science

10th February 2020

# Characterisation of Inverted Coaxial Detectors

# and Calibration Source Production

# for the GERDA Experiment

Dissertation

zur

Erlangung der naturwissenschaftlichen Doktorwürde

(Dr. sc. nat.)

vorgelegt der

Mathematisch-naturwissenschaftlichen Fakultät

der

Universität Zürich

von

Michael Miloradovic

von

Zürich, ZH

**Promotionskommission**

Prof. Dr. Laura Baudis (Vorsitz)

Prof. Dr. Nicola Serra

Dr. Roman Hiller

Zürich, 2020

# Abstract

One of the biggest mysteries modern physics aims to solve is the dominance of matter over antimatter in our Universe. The discovery of the neutrinoless double beta ($0\nu\beta\beta$) decay would demonstrate lepton number violation and unveil the Majorana nature of neutrinos, enabling a Standard Model extension theorised to have caused the matter excess through leptogenesis induced baryonic number violation. The Germanium Detector Array (GERDA) experiment is searching for the $0\nu\beta\beta$ decay of $^{76}$Ge with an array of germanium detectors, enriched in $^{76}$Ge to $> 86\%$, underground at the Laboratori Nazionali del Gran Sasso (LNGS). GERDA has achieved the world leading median sensitivity of $1.1 \cdot 10^{26}$ yr on the $0\nu\beta\beta$ decay half-life. As part of the next generation experiment LEGEND, the goal is to employ first 200 kg and then, in the second stage, 1 t of germanium detectors to fully probe the inverted neutrino mass hierarchy and capitalise on the substantial normal hierarchy $0\nu\beta\beta$ decay discovery probability.

To meet the active mass ambition of LEGEND, a new germanium detector type was investigated, the Inverted Coaxial (IC) detector. Offering a larger mass, but equally strong Pulse Shape Discrimination (PSD) capabilities as the previous best performing type, the Broad Energy Germanium (BEGe) detector. PSD is the discerning of event topologies that deposit energy in a single location inside the detectors, such as $0\nu\beta\beta$ decay, from background events, that often interact in multiple places. For BEGe and IC detectors, this involves the ratio A/E of the maximum induced current amplitude A and the total energy E, both measured from the induced waveform pulse.

Five new IC type detectors were characterised using $^{228}$Th and $^{241}$Am radioactive sources and their Full Charge Collection Depths (FCCDs), active volumina, and active masses were determined through data comparison with Monte Carlo (MC) simulations in the framework of this thesis. FCCDs describe the part of the n+ electrode bordering the active volume, wherein interactions induce either no charge (Dead Layer) or only partial charge (Transition Layer) through diffusion into the active part.

A Pulse Shape Simulation (PSS) framework was developed, to simulate realistic induced charge and current signal waveforms. It was verified for the implemented BEGe and IC detector geometries with $0\nu\beta\beta$-signal-like events from $^{228}$Th calibration data, retrieving their electronic response parameters in the process.

Moreover, the low energy tails observed in the IC detector $^{241}$Am source measurements were reproduced, both in simulated energy histograms and simulated A/E space through PSS, to establish that it is a Transition Layer partial induction effect, validating the methods used for the FCCD determination.

A background model for the natural non-enriched detectors was created through the combined fit of separately MC simulated energy spectra for each background component onto the data spectrum. The dataset was created in a detector stability analysis, covering 799 days of data taking. The 7.6% natural abundance of $^{76}$Ge in the natural detectors and, thus, order of magnitude lowered $2\nu\beta\beta$ spectrum was exploited to extract the otherwise partially concealed specific activities of $^{39}$Ar to $(1.17 \pm 0.04\,(\text{stat.}) \pm 0.06\,(\text{sys.}))$ Bq/kg and $^{85}$Kr to $(0.84 \pm 0.12\,(\text{stat.}) \pm 0.1\,(\text{sys.}))$ mBq/l. Through a $\gamma$-line study of newly uncovered $^{214}$Bi peaks, the primary background $^{214}$Bi background source was identified to originate in the high voltage cables as an input to the main background model.

Four new custom low neutron emission $^{228}$Th calibration sources were produced in collaboration with Paul Scherrer Institute (PSI) and the University of Mainz and characterised underground at LNGS. The neutron emission was reduced through chemically depositing the $^{228}$Th inside of gold foils, which feature an $(\alpha,n)$-production energy threshold above the natural the decay chain's maximum $\alpha$ decay energy. The sources were measured with a LiI(Eu) detector to exhibit a neutron emission flux of $(7.8 \pm 0.5(\text{stat.}) \pm 1.1(\text{sys.})) \cdot 10^{-7}\,\frac{\text{n}}{\text{Bq}\cdot\text{s}}$, which is an order of magnitude lower than commercial sources. This reduces the $^{77}$Ge background from neutron activation of the detectors to a contribution to the background index of $10^{-4}$ cts/(keV·kg·yr) prior to analysis cuts, well below the background of GERDA Phase II. The $\gamma$-ray activities of the sources were determined inside the High Purity Germanium (HPGe) counting facility Gator.

The five IC detectors and the $^{228}$Th calibration sources were subsequently installed into GERDA. They will serve in the active exposure gain of the experiment and the estimation of the energy resolution from $^{228}$Th calibration data, respectively, to further improve the half-life sensitivity for the final unblinding of GERDA in 2020 and LEGEND in the future.

# Contents

# Chapter 1

# Introduction

One of the biggest mysteries modern physics aims to solve is the dominance of matter over antimatter in our Universe. While the discovery of the Higgs Boson was heralded as the last missing puzzle piece of the elementary particle table, proving the prediction power of the Standard Model (SM) of Particle Physics, an undeniable piece of evidence remained of physics beyond the SM: our very existence. According to the SM, the Big Bang should have produced an equal number of matter and anti-matter, eventually leading to the complete annihilation of the matter in the perfectly symmetrical early universe [1]. The observed matter dominance of today, however, is the remnant of a slight asymmetry introduced in its early stages. All the galaxies and stars descend from a $6.19 \cdot 10^{-10}$ initial relative excess of baryonic matter, estimated from the Cosmic Microwave Background (CMB) baryon to photon ratio [2].

The answer to the origin of this asymmetry, and thus of our own existence, could lie in the special nature of the neutrino [3]. It is theorised to be a Majorana fermion and therefore its own anti-particle [4]. This property could introduce massive right-handed neutrinos as an extension to the Standard Model, generating the matter excess through leptogenesis induced baryonic number violation [3]. Hence, determining the nature of the neutrino is of fundamental importance to modern physics [5]. These concepts are further explained in Sections 1.3–1.5.

The Germanium Detector Array (GERDA) experiment, located underground at the Laboratori Nazionali del Gran Sasso (LNGS) in Italy, searches for the neutrinoless double beta decay ($0\nu\beta\beta$) of $^{76}$Ge with germanium diodes directly

submerged in a liquid argon cryostat [6, 7]. The discovery of the decay would not only demonstrate lepton number violation, but also prove that the neutrino has a Majorana mass component [8]. Crucial information on the neutrino mass hierarchy and the absolute values of the neutrino masses could be gained as well. The details of GERDA, the $0\nu\beta\beta$ sensitivity results from Phase I and Phase II in comparison to other leading experiments, and its future as part of the LEGEND experiment are described in Chapter 2.

The sensitivity on the $0\nu\beta\beta$ half-life scales linearly with exposure if the product of the background index and the energy resolution are sufficiently small in comparison to the exposure, given as

$$T_{1/2}^{0\nu\beta\beta} \propto \sqrt{\frac{\mathcal{E}}{BI \cdot \Delta E}} \overset{BI \cdot \Delta E \ll \mathcal{E}}{\propto} \frac{\mathcal{E}}{BI \cdot \Delta E} , \tag{1.1}$$

where $T_{1/2}^{0\nu\beta\beta}$ is the half-life in units of [yr], BI the background index in [event counts/(keV $\cdot$ kg $\cdot$ yr)], $\Delta E$ the energy resolution in [keV], and $\mathcal{E}$ the exposure in [kg$\cdot$yr]. This concept is discussed at more length in the next chapter. The key elements of the experiment are thus the understanding and reduction of the background in the region of interest around the $0\nu\beta\beta$ decay peak at $Q_{\beta\beta}$, the best estimate of the energy resolution, and the determination of the active exposure as a measure of gathered data by the germanium detector active mass. The work in the scope of this thesis lead to advancement in all of these three areas.

Chapter 3 describes the background model and the contribution in the framework of this thesis. The background model is used to predict a flat background and thus enables the background estimation prior to unblinding, as explained in Section 2.6. The identification of specific background source locations, realised through the creation of a background model for the non-enriched natural detectors, was performed as an input to the main background model. This lead to a better understanding of the background and potentially will improve the background index after the latest upgrade for the final unblinding and next generation experiments.

To meet the ambitious goal of 200 kg for the LEGEND-200 experiment and eventually one ton for LEGEND-1000, new germanium detector types were investigated. Five germanium detectors of the new Inverted Coaxial (IC) type were characterised and their active volumina and active masses were determined in Chapter 4

to employ them for active exposure gain directly in GERDA and in the future in LEGEND.

The detectors are capable of discerning $0\nu\beta\beta$ event topologies, that deposit energy in a single location inside the detectors, from background events, that often interact in multiple locations. This is called Pulse Shape Discrimination (PSD), as described in Section 2.4, and involves for certain detector types the ratio A/E of the maximum induced current amplitude A and the total energy E, both measured from the induced charge pulse waveform. Chapter 5 covers the development of a Pulse Shape Simulations framework to facilitate the characterisation of new detectors and the determination of key detector parameters, such as A/E capabilities. In addition, a better understanding of the Transition Layer was achieved by reproducing, both in simulated energy histograms and simulated A/E space, the low energy tail shape of peaks observed in data, thus verifying the methods of the IC detector active mass determination. The Transition Layer is the part of the n+ electrode, wherein interactions only induce a fraction of the charge, lowering the reconstructed energy and producing low energy tails in the energy spectrum.

Chapter 6 reports on the production and the characterisation of four new low neutron emission $^{228}$Th sources, now employed as the primary calibration sources inside the GERDA experiment. The neutron flux was determined to ensure a minimal induced $^{77}$Ge background from the neutron activation of the detectors. The determined source activities will serve to scale calibration simulations to judge the background model accuracy and Pulse Shape Discrimination efficiencies. Most importantly, the energy resolution of the detectors in the final unblinding of GERDA will be estimated with calibration data gathered using these sources.

At the end of this work, a conclusion and an outlook are presented in Chapter 7.

## 1.1   The Standard Model of Particle Physics

All known elementary particles in the Standard Model of modern particle physics are divided into two distinct groups: 12 fundamental matter *fermions* and 4 force transmitting *bosons*, as shown in Figure 1.1 [9]. The strong force is propagated

through gluons, the electromagnetic force through $\gamma$-particles, and the weak force through the heavy $W^{\pm}$ and $Z^0$ bosons. On the fermion side, there are 6 different quarks that, in combination with each other, form the spectrum of known three-quark hadrons and two-quark mesons. In addition, there are 6 more elementary particles in the fermion group, namely the 3 generations of charged leptons, paired in weak isospin doublets with their neutral neutrino flavour counterparts. Neutrinos carry no electric or colour charge and thus do not interact electromagnetically or via the strong force. They are produced in interactions mediated by the weak force, e.g. beta decays (explained further in the next section). This fact makes them hard to observe and thus they are often detected indirectly, for example by missing energy in the final state.

In recent years, tensions between the results of neutrino experiments and the Standard Model have appeared that hint at physics beyond the Standard Model, motivating a strong effort in the uncovering of the neutrino properties.
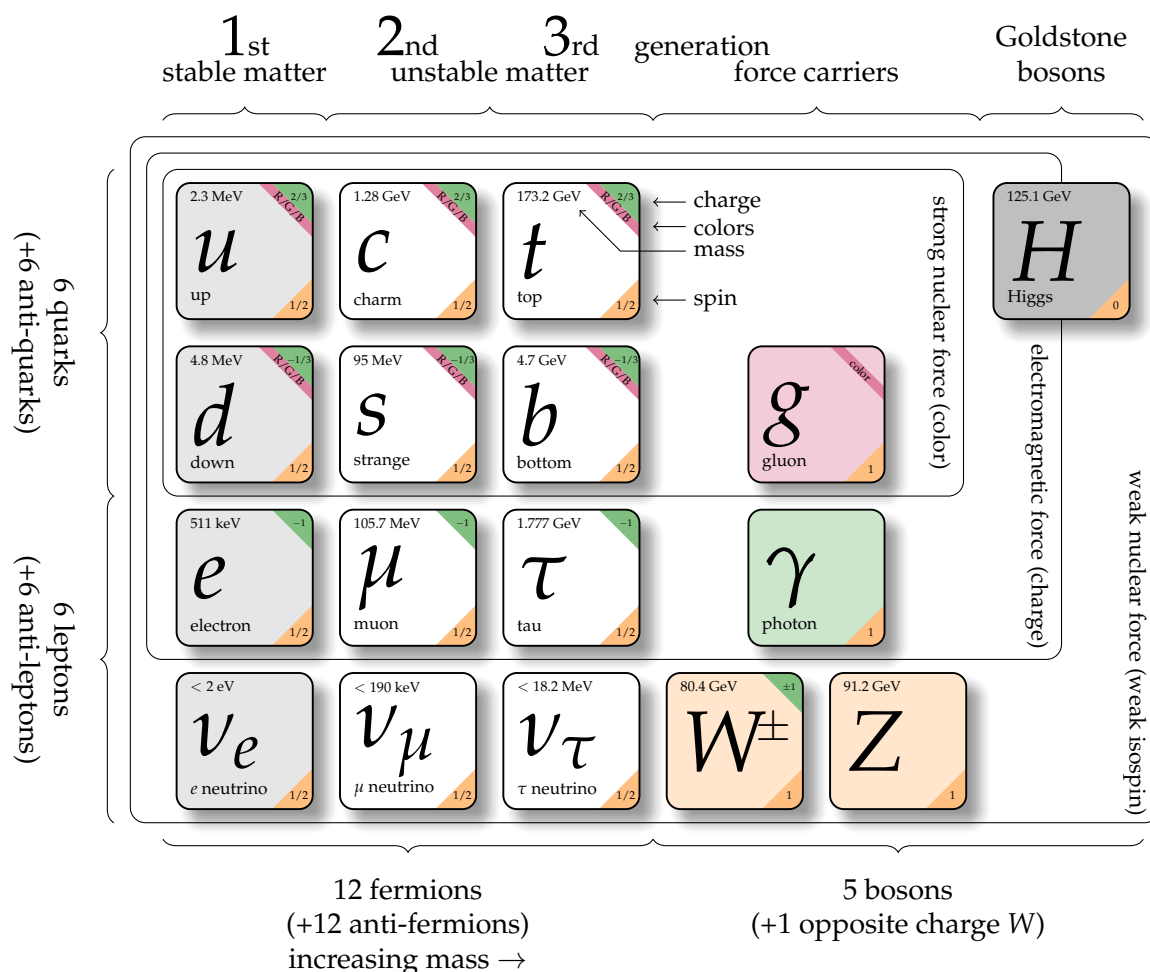


FIGURE 1.1: The Standard Model of Particle Physics. Figure from [10].

## 1.2 Leptons and the Weak Interaction

Inspired by Wilhelm Conrad Röntgen's discovery of X-rays in 1896, Henri Becquerel found unstable atomic nuclei like uranium to lose energy through radiation [11]. Exploring this phenomenon of radioactivity further, Ernest Rutherford discovered two types of radiation that differed from X-rays in their penetration depth: alpha- and beta-rays [12]. The latter originating from a *beta decay*; the spontaneous decay of a neutron in the nucleus to a proton under the emission of an electron and, as was discovered later, an electron anti-neutrino $\bar{\nu}_e$, as shown in Figure 1.2.
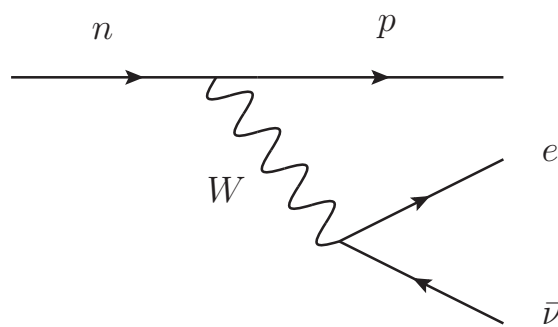


FIGURE 1.2: Feynmann diagram of a beta decay. A neutron $n$ in the nucleus decays into a proton $p$ under the weak interaction emission of an electron $e^-$ and an electron anti-neutrino $\bar{\nu}_e$

Wolfgang Pauli predicted the existence of the neutrinos in 1930 as completely new, undetected elementary particles to maintain the conservation of energy and momentum in beta decays [13]. The electron is emitted to conserve charge, but the electron anti-neutrino conserves the lepton number and lepton flavour. The concept of lepton number conservation was introduced in 1953 to explain the non-existence of certain decays [14]. In a similar vein, lepton flavour conservation originated from the lack of $\mu \rightarrow e + \gamma$ observation in experiments [15]. There is however no fundamental symmetry in the mathematical foundation of the Standard Model that predicts this conservation law through Noether's theorem. This is unlike the SU(3)×SU(2)×U(1) gauge symmetries that predict the conservation of the colour charge, weak isospin, and electric charge (in the electroweak regime as weak hypercharge). The violation of lepton number conservation is thus a real possibility to be explored, as explain in Section 1.5.

In 1953, the electron anti-neutrino $\bar{\nu}_e$ was discovered in a nuclear reactor assisted scintillator experiment, measuring the inverse beta decay $\bar{\nu}_e + p \rightarrow n + e^+$ [16]. In the Wu experiment in 1956, the conservation of parity, previously established for the strong and electromagnetic forces, was found to be violated in weak interactions [17]. This was accomplished through the comparison of the emission anisotropies in a uniform magnetic field of $^{60}$Co beta decay electrons in relation to the subsequent excited state $\gamma$-ray emissions. Just a year later, the Goldhaber experiment exploited the electron capture reaction of the $^{152m}$Eu isomere to produce a photon in the decay of the subsequent excited state $^{152}$Sm$^*$ with the same helicity as the initially emitted electron neutrino $\nu_e$. It was thus shown that neutrinos maximally violate parity and that they are exclusively left-handed $\nu_L$, while anti-neutrinos are exclusively right-handed $\bar{\nu}_R$ [18].

Preceding all of these experiments, Ettore Majorana suggested in 1937 that the neutrinos could be their own anti-particles and introduced a Majorana mass term for the neutrinos [4]. He parametrised the right-handed anti-neutrinos $\bar{\nu}_R$ as functions of the left-handed neutrinos $\nu_L$, implying that all phenomena later observed in experiments attributed to these two different particles could simply be due to the two different chirality states $L$ and $R$ of a single particle $\nu$ [17, 18]. This mathematical formulation allows, as discussed in the following sections, a new understanding of the origin of the special neutrino properties and physics beyond the Standard Model.

## 1.3   Neutrino Oscillation and Neutrino Mass

In the Standard Model, the neutrinos are massless. In recent years however, the discovery of neutrino oscillations by a large number of different experiments has established neutrino mixing and thus a non-zero mass of the neutrinos [19, 20]. This is due to the mixing mechanism of the neutrino flavour states ($\nu_e$, $\nu_\mu$, $\nu_\tau$) as superpositions of neutrino mass eigenstates ($\nu_1$, $\nu_2$, $\nu_3$), as shown in Equation 1.2, through the Pontecorvo-Maki-Nakagawa-Sakata (PMNS) matrix [21]. This in turn requires the neutrinos to have a mass. This explanation is an analogy to the Cabibbo-Kobayashi-Maskawa (CKM) matrix for the quark flavour mixing [22–24].

$$\begin{pmatrix} \nu_e \\ \nu_\mu \\ \nu_\tau \end{pmatrix} = \underbrace{\begin{pmatrix} U_{e1} & U_{e2} & U_{e3} \\ U_{\mu1} & U_{\mu2} & U_{\mu3} \\ U_{\tau1} & U_{\tau2} & U_{\tau3} \end{pmatrix}}_{\mathbf{U}_{\text{PMNS}}} \begin{pmatrix} \nu_1 \\ \nu_2 \\ \nu_3 \end{pmatrix} \tag{1.2}$$

The PMNS matrix, given in Equation 1.3 with $c_{ij} = cos\theta_{ij}$ and $s_{ij} = sin\theta_{ij}$, is parametrised by the three mixing angles $\theta_{12}$, $\theta_{23}$, and $\theta_{13}$. It also contains the Dirac phase factor $\delta$ and two Majorana phases $\alpha_1$ and $\alpha_2$ for the case of Majorana neutrinos. The Charge Conjugation Parity (CP) symmetry violating nature of these phases has been hypothesized, but not yet observed [5]. Recently, the experiment T2K has found $2\,\sigma$ evidence for CP violation in the lepton sector [25].

$$\mathbf{U}_{\text{PMNS}} = \begin{pmatrix} c_{12}c_{13} & s_{12}c_{13} & s_{13}e^{-i\delta} \\ -s_{12}c_{23} - c_{12}s_{23}s_{13}e^{i\delta} & c_{12}c_{23} - s_{12}s_{23}s_{13}e^{i\delta} & s_{23}c_{13} \\ s_{12}s_{23} - c_{12}c_{23}s_{13}e^{i\delta} & -c_{12}s_{23} - s_{12}c_{23}s_{13}e^{i\delta} & c_{23}c_{13} \end{pmatrix} \begin{pmatrix} e^{i\alpha_1/2} & 0 & 0 \\ 0 & e^{i\alpha_2/2} & 0 \\ 0 & 0 & 1 \end{pmatrix}$$
$$\tag{1.3}$$

Oscillation experiments measure the squared neutrino mass difference $\Delta m_{ij}^2$ from the neutrino flavour change probability containing the PMNS matrix. They are however not able to distinguish between the Dirac or Majorana nature of the neutrinos and are not sensitive to the absolute neutrino mass scale. This leaves the problem of the neutrino mass hierarchy, i.e. whether the $\nu_3$ neutrino mass eigenstate is heavier or lighter than the other two. The normal hierarchy is given by $m_1 < m_2 << m_3$, whereas the inverted hierarchy ordering is $m_3 << m_1 < m_2$ [5]. The discovery probability of the neutrinoless double beta decay strongly depends on the neutrino mass hierarchy, as shown in Figure 1.3. Already next generation experiments will be able to fully probe the inverted hierarchy region, while for normal hierarchy the discovery probability can reach up to 50% or more in the leading experiments [26]. The current constraints are shown and discussed further in Section 2.2.

The Standard Model can be extended by including right-handed neutrinos $\nu_R$ to account for the occurrence of neutrino oscillations and masses. This avoids the introduction of a bare mass term and preserves renormalisability. In parity violation experiments, such as the Wu and Goldhaber, however, neutrinos were found to be exclusively left-handed [17, 18]. Right-handed neutrinos $\nu_R$ must
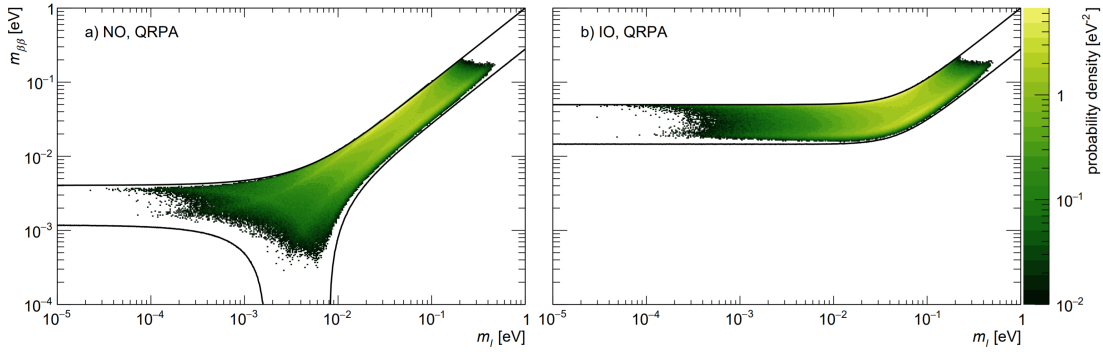
FIGURE 1.3: The neutrino mass hierarchy for normal ordering (left) and inverted ordering (right) as a probability density marginalized posterior distributions dependent on achieved $m_{\beta}\beta$. Allowed parameter space (solid lines) from current $3\sigma$ intervals of the neutrino oscillation observables from NuFIT [27]. The nuclear matrix elements are from [28]. Figure from [26].

therefore be *sterile* singlets and cannot interact weakly [29, 30]. With this extension, neutrinos gain a Dirac mass term $\mathcal{L}_D$ directly from the Higgs mechanism in an analogy to the quark and charged lepton masses [31]. Mass $m_{\nu}$ is thereby generated by the Yukawa coupling $f_{\nu}$ to the Higgs field vacuum expectation value $\langle \phi \rangle_0$ and the interactions of the left-handed fermions with their right-handed chirals as follows [9, 30]

$$\mathcal{L}_D = -f_{\nu}\phi\bar{\nu}_L\nu_R \tag{1.4}$$

$$= -f_{\nu}\langle\phi\rangle_0\bar{\nu}_L\nu_R \tag{1.5}$$

$$= -m_{\nu}\bar{\nu}_L\nu_R , \tag{1.6}$$

Unless the corresponding Yukawa coupling $f_{\nu}$ is unusually low, the result would logically be on a mass scale similar to that of other fermions and therefore several orders of magnitude higher than the three neutrino mass sum predicted by cosmology [5].

## 1.4 Majorana Mass and the See-saw Mechanism

A popular theory to explain the unparalleled low masses of the left-handed neutrinos is the see-saw mechanism. Sterile neutrinos can hold a bare mass term, such as the one predicted by Majorana, due to their weak isospin singlet nature. The left-handed pure states thus receive a Majorana mass component $\mathcal{L}_N$ through mixing with the sterile neutrinos in addition to their Dirac mass

term $\mathcal{L}_D$ as follows

$$\mathcal{L}_D + \mathcal{L}_N = -m_D \bar{\nu}_L \nu_R - m_N \bar{\nu}_R \nu_R \ . \tag{1.7}$$

These Dirac and Majorana components can be rewritten to form a neutrino mass matrix given by

$$\mathbf{M}_\nu = \begin{pmatrix} 0 & M_D \\ M_D^T & M_N \end{pmatrix} \tag{1.8}$$

$$\Rightarrow \lambda_+ \approx M_N \,, \quad \lambda_- \approx \frac{M_D^2}{M_N} \ .$$

Sterile neutrinos could be very heavy as their mass is completely unknown. In that case, one of the eigenvalues of the neutrino mass matrix ($\lambda_+$) would become approximately equal to the large Majorana mass component, while the other ($\lambda_-$) would be drastically reduced by it. As a result, the high mass of the sterile neutrinos could be responsible for the very low scale of the light neutrinos through mass mixing [9, 24, 29, 30].

The extension of the Standard Model by heavy sterile neutrinos offers another advantage. In the CP violating decays of sterile neutrinos, leptons can be spontaneously generated. The increased number of leptons in comparison to anti-leptons results in a lepton asymmetry in the early universe. A conversion of leptogenesis into baryogensis could then lead to the observed baryon asymmetry, which in turn would be responsible for the matter dominated universe of today it [3, 30, 32].

In consequence, exploring the Majorana nature of the neutrinos could help reconcile major cosmological issues of modern physics and lead to the discovery of physics beyond the Standard Model. The prime avenue to directly probe this fundamental neutrino characteristic and simultaneously obtain information on the absolute neutrino masses is the neutrinoless double beta decay [8].

## 1.5 Neutrinoless Double Beta Decay

The radioactive isotope $^{76}$Ge contains 32 protons and 44 neutrons in its nucleus. In order to achieve a more optimal ratio of nucleons, neutrons would need to spontaneously decay into protons under the emission of an electron and an electron anti-neutrino to conserve charge and lepton number. In reality, the nucleus of $^{76}$As, that would be attained by a beta decay, has a lower binding energy than the original one. The even numbered protons and neutrons of $^{76}$Ge make the nucleus more stable due to the spin-coupling than the odd-odd numbered $^{76}$As. This interaction channel is thus energetically forbidden, as shown in Figure 1.4.
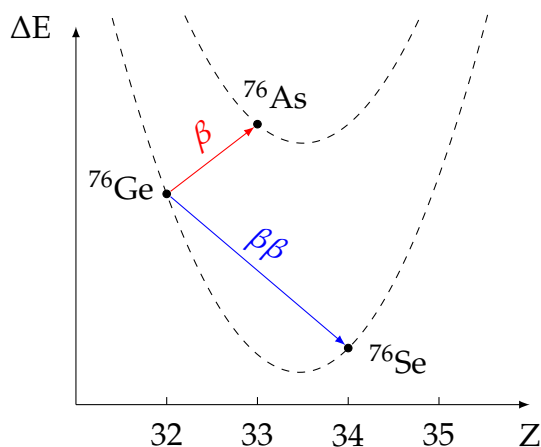


FIGURE 1.4: Mass parabola for the nuclei with atomic mass 76. A beta decay (red) from $^{76}$Ge to $^{76}$As cannot occur, because the binding energy of the daughter nucleus would be lower than the energy of the parent nucleus. Double beta decay (blue) to $^{76}$Se is allowed.

A *double beta decay* ($2\nu\beta\beta$) to $^{76}$Se is however energetically possible. Two neutrons are simultaneously converted to two protons, emitting two electrons and two electron anti-neutrinos. Figure 1.5a depicts the Feynmann diagram of the described interaction mediated by the weak force. As a higher order process, it has an extremely low decay rate. It is one of the rarest decays observed in an experiment. The half-life of the double beta decay of $^{76}$Ge is measured to be $T_{1/2}^{2\nu\beta\beta} = (1.926 \pm 0.094) \cdot 10^{21}$ yr [33].

The idea of a Majorana neutrino gives rise to an additional, theoretical decay channel. A neutrino that is its own anti-particle would allow for the annihilation of the two involved anti-neutrinos. In this *neutrinoless double beta decay* ($0\nu\beta\beta$), shown in Figure 1.5b, the decaying nucleus would emit only two electrons. The

(a) $2\nu\beta\beta$                    (b) $0\nu\beta\beta$
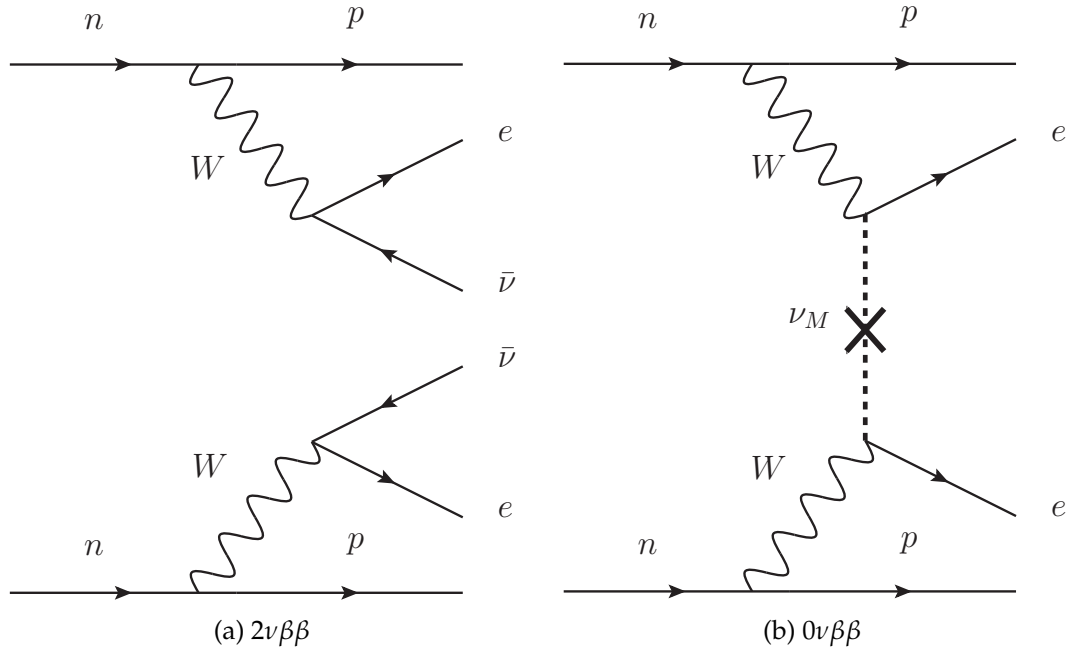
FIGURE 1.5: Feynmann diagrams of the double beta decay (a) and the neutrinoless double beta decay (b). The simultaneous decay of two neutrinos into two protons emits – mediated by two charged weak gauge bosons – two electrons and two electron anti-neutrinos. In the neutrinoless case, the two Majorana neutrinos annihilate off-shell.

neutrinos are virtual. This interaction violates lepton number conservation by two units [8, 30].

The theoretical $0\nu\beta\beta$ decay half-life is given by [24]:

$$T_{1/2}^{0\nu\beta\beta} = \frac{m_e^2}{G^{0\nu}|M^{0\nu}|^2|m_{\beta\beta}|^2} \tag{1.9}$$

with the phase space integral $G^{0\nu} = 2.36 \cdot 10^{-15} yr^{-1}$ [34], the nuclear matrix element $|M^{0\nu}| = 2.8$–$5.2$ [28, 35], and the effective Majorana mass $|m_{\beta\beta}|$. The high uncertainty on the nuclear matrix elements from nuclear physics measurements induce a high uncertainty on the half-life, as seen in the large uncertainty band in Figure 1.3. Since the planning of ton-scale experiments in recent times, efforts have increased to determine the nuclear matrix elements more accurately [28]. The neutrino masses of the mass eigenstates ($\nu_1$, $\nu_2$, $\nu_3$) are connected to the elements of the PMNS lepton mixing matrix. The equation for light neutrino exchange takes the form of [24]

$$|m_{\beta\beta}| = |\sum_{i=1}^{3} U_{ei}^2 m_{\nu_i}| \,. \tag{1.10}$$

In this way, the observation of the $0\nu\beta\beta$ decay would be a direct confirmation of the Majorana nature of the neutrinos and would allow the study of the Majorana phases in the PMNS matrix and the absolute neutrino mass scale [8].

## 1.6  Current Status of the Field

Due to its high importance for modern physics, there are several leading experiments searching for neutrinoless double beta decay using different experimental set-ups and isotopes that undergo double beta decay. Their isotope, background rate and energy resolution product, total exposure, lower limits and half-life sensitivites are given in the next chapter in Table 2.2.

Even though KamLAND-Zen and EXO-200 both use $^{136}$Xe, they are based on two different approaches: EXO-200 exmploys a cylindrical time projection chamber, equipped with wires and avalanche photodiodes, and is filled with 200 kg of liquid xenon enriched to 80.6% [36]. KamLAND-Zen, on the other hand, consists of 13 t of xenon loaded liquid scintillator inside a 1.5 m radius spherical nylon balloon in the centre of the KamLAND detector, filled with 1000 t of liquid scintillator as an active shield [37]. These huge quantities of $^{136}$Xe provide high exposures for these experiments.

There are also bolometers probing the Majorana nature of neutrinos, measuring incident radiation via crystal heating: As examples, CUPID and CUORE, both at LNGS in Italy, employ $^{82}$Se and $^{130}$Te, respectively [38, 39]. While CUPID utilised scintillating bolometers with 24 enriched ZnSe crystals, CUORE is a ton-scale cryogenic bolometer array.

Aside from GERDA, which is explained in detail in the next chapter, there exists also the Majorana Demonstrator based on high purity germanium detectors enriched to $> 86\%$ in $^{76}$Ge [40]. At the Sanford Underground Laboratory in the USA, at a 4300 m water equivalent depth, the experiment consists of 29.7 kg of enriched detectors in vacuum cryostats surrounded by copper shields and lead bricks, a radon enclosure, and veto panels to minimise the background. The GERDA and Majorana Collaborations are now working together as part of LEGEND in the search for the neutrinoless double beta decay [41].

# Chapter 2

# The GERDA Experiment

The Germanium Detector Array (GERDA) experiment at the Laboratori Nazionali del Gran Sasso (LNGS) has been built by an international collaboration of 16 institutions for the high sensitivity search of the neutrinoless double beta decay of $^{76}$Ge [6]. It employs high-purity germanium diodes isotopically enriched in $^{76}$Ge to $> 86\%$, acting simultaneously as the detector and source material. The detection mechanism and the expected signal are described in Section 2.4. The germanium diodes are operated directly submerged in high purity Liquid Argon (LAr) in a 64 m$^3$ cryostat of 4.2 m diameter. This provides the necessary operational temperature for the detectors, as well as shielding against environmental radioactivity.

The cryostat is surrounded by a 590 m$^3$ with 10 m diameter purified water tank, suppressing $\gamma$-radiation and absorbing neutrons. In addition, cosmic muons are detected by a Cherenkov veto system, described in Section 2.8, using 66 8-inch Photomultiplier Tubes (PMTs) installed inside the tank. The experiment is located in an underground laboratory, 1400 m (3500 m water equivalent) below the surface to suppress cosmic rays. These shielding and veto layers ensure a substantial reduction of the background and the highest possible sensitivity for the experiment. Figure 2.1 depicts a schematic dissection of the GERDA experiment. Further literature, describing the experiment in full detail, can be accessed in the publications of the GERDA Collaboration [6, 7, 42–46].

The physics program of GERDA set its goal to achieve a median sensitivity of $10^{26}$ yr on the $0\nu\beta\beta$ half-life by gathering a total exposure of 100 kg · yr, divided into two main phases: Phase I and Phase II [7, 42]. The following Sections 2.1

and 2.2 report the upgrades and achievements of each phase, while Table 2.1 summarises the results, as well as the goals for the future.

a) GERDA Overview          b) LAr veto system     c) Detector array
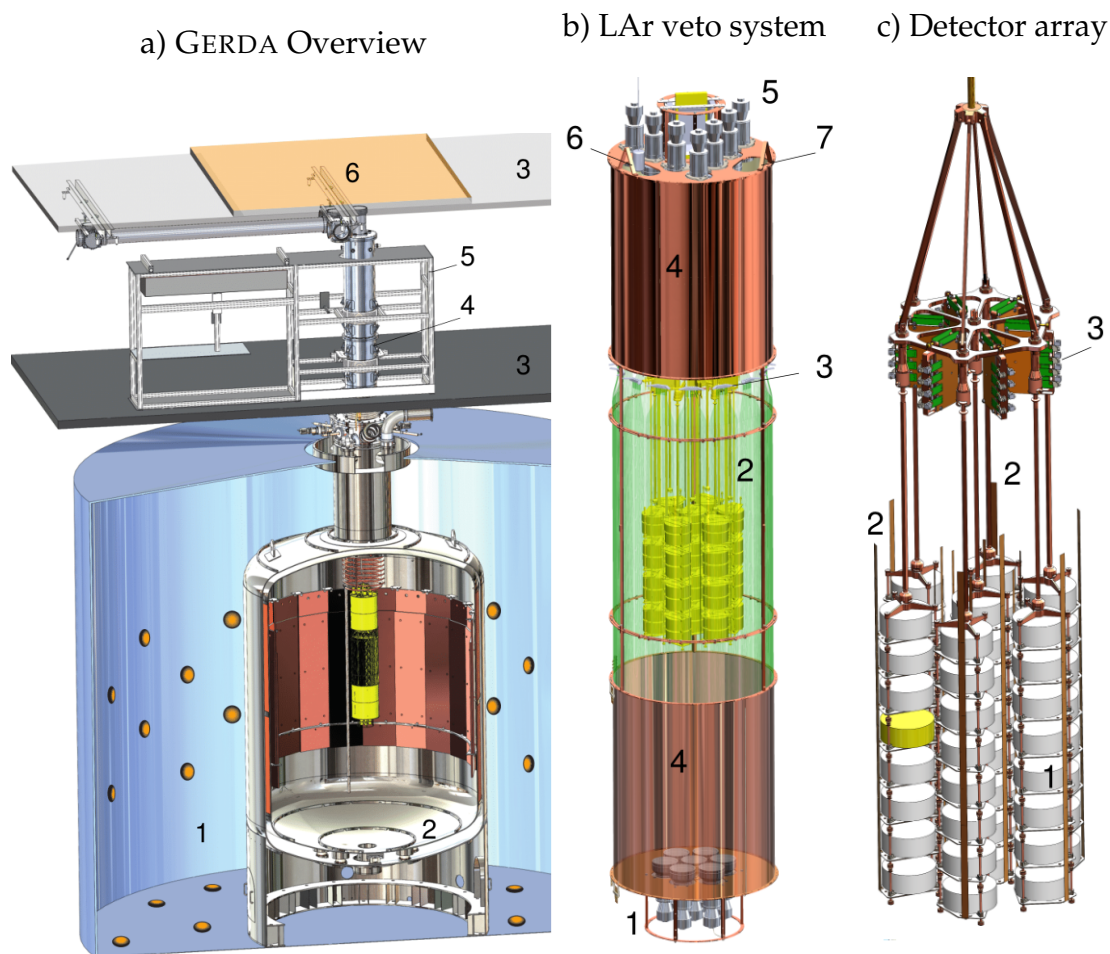


FIGURE 2.1: GERDA experiment schematic view divided into three zoom levels:
a) Overview of the GERDA experiment surrounded by a water tank Cherenkov muon veto equipped with PMTs (1), LAr cryostat (2), and clean room (3) from where the germanium detector array is lowered into the LAr cryostat on strings via a lock and suspension system (4). The glove box (5) allows the clean handling of the materials. The top muon incident angle is controlled by a plastic muon veto system (6).
b) LAr veto system, installed in Phase II, has its bottom (1) and top (5) equipped with 7 and 9 PMTs, respectively. The fibre curtain (2) coated with wavelength shifter leads the scintillation light to the SiPMs (3). Surrounding the veto are copper shrouds (4) with entry points for the calibration sources (6, 7).
c) Germanium detector array arranged on 7 strings held in place by copper support rods with readout cables and high voltage cables (2) going through to the amplifiers (3). Figure from [45].

## 2.1  Phase I

Between November 2011 and June 2013, Phase I of the experiment acquired data with 12 kg of coaxial and 3 kg of Broad Energy germanium (BEGe) detectors on four strings for a total exposure of 21.6 kg·yr. Thanks to the innovative shielding system, an order of magnitude lower background index than previous germanium experiments, such as HDM [47] and IGEX [48], was obtained with a background index of $1.1^{+0.2}_{-0.2} \cdot 10^{-2}$ event counts/(keV · kg · yr) at $Q_{\beta\beta}$. Due to this progress, Phase I yielded the most stringent lower limit of $T^{0\nu\beta\beta}_{1/2} > 2.1 \cdot 10^{25}$ yr at a 90% Confidence Level (CL) [44] for the $0\nu\beta\beta$ half-life of $^{76}$Ge. The median sensitivity for the 90% CL limit was $2.4 \cdot 10^{25}$ yr.

## 2.2  Phase II

To further reduce the background, the experiment received a substantial upgrade moving to Phase II [7, 42]. One of the two main improvements was the installation of a LAr veto system. It consists of a cylindrical volume with 2.2 m height and 0.5 m diameter located at the center of the LAr cryostat. It contains a total of 16 PMTs at its ends and, at this stage, a curtain of 810 fibres connected to Silicon Photomultipliers (SiPMs). This hybrid anti-coincidence system detects wavelength shifted scintillation light, induced by radioactive background contamination outside the germanium crystals, as explained in Section 2.7.

The second major change was the installation of 20 kg of additional BEGe detectors, increasing the active mass to 35 kg, on a total of seven strings. A photo of such a Phase II BEGe detector string is shown in Figure 2.2. The data taking for Phase II started in December 2015 and remained blinded in the region of interest until June 2016 for the Ringberg GERDA Collaboration Meeting. The blinding method and its importance for an unbiased analysis are explained in Section 2.6. After collecting a total exposure of 10.8 kg·yr, resulting in a combined 34.4 kg·yr of exposure, the data was unblinded and a new 90% CL lower limit was found for a half-life of $5.3 \cdot 10^{25}$ yr. With the enhanced PSD properties of the BEGe detectors for background reduction, and the LAr veto system in place, a tenfold lower background index was achieved with $1.0^{+0.6}_{-0.4} \cdot 10^{-3}$ counts/(keV·kg·yr). These results were subsequently published in *Nature* [45]. The following unblinding

FIGURE 2.2: Photo of GERDA Phase II BEGe detector string (left) and the LAr veto fibre shroud (right) that guides the scintillation light to the Silicon Photomultipliers. The picture is taken after its upgrade in April 2018 to make it denser and thus increase its light yield by a factor two.

events at the Cracow GERDA Meeting (Phase IIb) in June 2017 and GERDA Meeting at LNGS (Phase IIc) in May 2018, each introduced another year of data, thus improving the exposure, lower limit, and median sensitivity progressively, as shown in Table 2.1.

| | | Mass | $\mathcal{E}$ | BI (BEGe/Coax) | $\mathcal{L}$ | $\mathcal{S}$ |
|---|---|---|---|---|---|---|
| | | | total | $10^{-3}$ | $10^{26}$ | $10^{26}$ |
| Phase | Publication (year) | [kg] | [kg·yr] | [counts/(keV·kg·yr)] | [yr] | [yr] |
| I | Phys. Rev. (2013) [44] | 17.9 | 21.6 | $5^{+4}_{-3}$ / $11^{+2}_{-2}$ | 0.21 | 0.24 |
| IIa | Nature (2017) [45] | 35.6 | 34.4 | $0.7^{+1.1}_{-0.5}$ / $3.5^{+2.1}_{-1.5}$ | 0.53 | 0.40 |
| IIb | Phys. Rev. (2018) [46] | 35.6 | 46.7 | $1.0^{+0.6}_{-0.4}$ / $3.5^{+2.1}_{-1.5}$ | 0.80 | 0.58 |
| IIc | Science (2019) [49] | 35.6 | 82.4 | $0.6^{+0.4}_{-0.3}$ / $0.6^{+0.3}_{-0.2}$ | 0.9 | 1.1 |
| Goal | *Projected* [50] | 45.1 | 100 | | | 1.4 |

TABLE 2.1: GERDA Phase I and Phase II results for different unblinding events and publications in terms of active detector mass, exposure $\mathcal{E}$, Background Index (BI), $T^{0\nu\beta\beta}_{1/2}$ lower limit $\mathcal{L}$ on, and $T^{0\nu\beta\beta}_{1/2}$ median sensitivity $\mathcal{S}$.

As a result of these advancements, GERDA achieved the world's best median sensitivity on the $0\nu\beta\beta$ decay half-life of $1.1 \cdot 10^{26}$ yr, published in *Science* [49]. The unblinded combined spectrum for with the best fit of no event reconstructed

within $Q_{\beta\beta} \pm 2\sigma$ is given in Figure 2.3. This lead to the most stringent $^{76}$Ge $0\nu\beta\beta$ half-life limit of $0.9 \cdot 10^{26}$ yr at 90% CL.
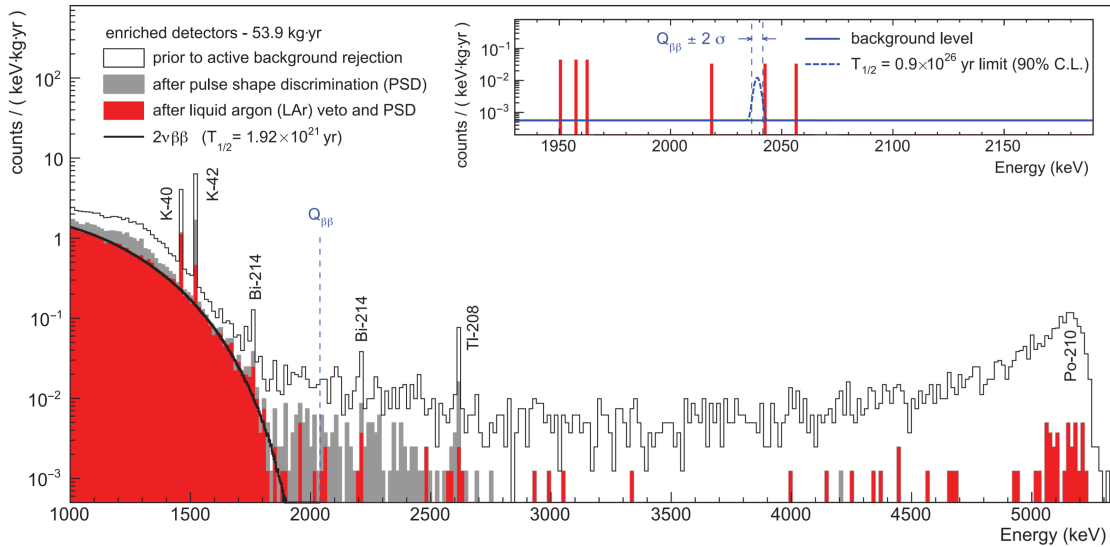


FIGURE 2.3: Latest unblinded results of GERDA Phase II as a combined spectrum of enriched detectors for 53.9 kg·yr of exposure prior to active background rejection analysis cuts (white), after Pulse Shape Discrimination (grey), and LAr veto and PSD combined (red). The main background contributions are labelled. The background indices around $Q_{\beta\beta}$ (small graphs, solid blue lines) are shown for each detector type separately. The best fit is of no event reconstructed within $Q_{\beta\beta} \pm 2\sigma$ with the $0\nu\beta\beta$ signal limit (dashed blue curve) of $T_{1/2} = 0.9 \cdot 10^{26}$ yr at 90% CL. The blinding method is explained in Section 2.6. Figure from [49].

The current leading experiments in the field, presented in Section 1.6, are listed in Table 2.2 sorted by their double beta decaying isotopes. Notably, while $^{136}$Xe experiments collect a lot of exposure, the $^{76}$Ge experiments excel in energy resolution and background suppression.

| Experiment | Isotope | $\mathcal{B}$·FWHM [counts/(t·yr)] | $\mathcal{E}$ [kg·yr] | $\mathcal{L}$ $10^{26}$ [yr] | $\mathcal{S}$ $10^{26}$ [yr] |
|---|---|---|---|---|---|
| GERDA [49] | $^{76}$Ge | 2 | 82.4 | 0.9 | 1.1 |
| Majorana [40] | $^{76}$Ge | 15 | 23 | 0.27 | 0.48 |
| KamLAND-Zen [37] | $^{136}$Xe | 96 | 540 | 1.07 | 0.56 |
| EXO-200 [36] | $^{136}$Xe | 114 | 234 | 0.35 | 0.50 |
| CUORE [39] | $^{130}$Te | 108 | 24 | 0.15 | 0.07 |
| CUPID [38] | $^{82}$Se | 83 | 2 | 0.02 | 0.02 |

TABLE 2.2: Comparison of leading $0\nu\beta\beta$ decay experiments ordered by isotope, showing listing product of background rate $\mathcal{B}$ and FWHM energy resolution, exposure $\mathcal{E}$, lower limit of the $0\nu\beta\beta$ decay half-life $\mathcal{L}$ at 90% CL, as well as median sensitivities $\mathcal{S}$ at 90% CL
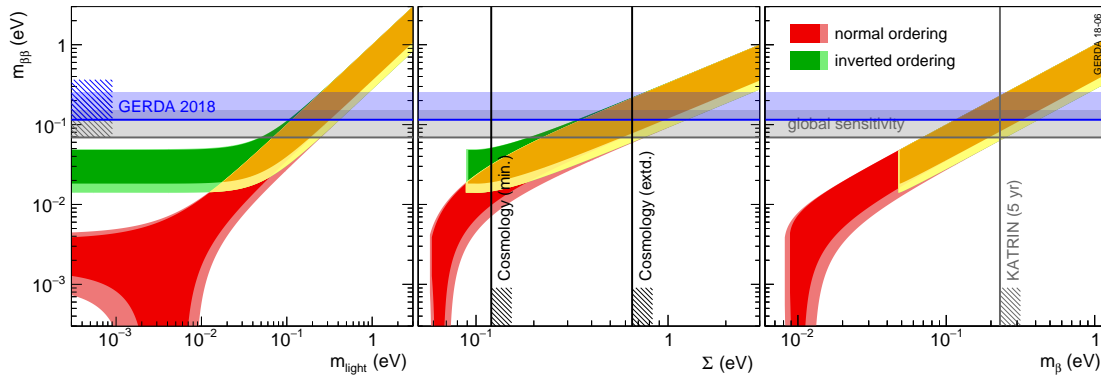
FIGURE 2.4: Current Limits on $m_{\beta\beta}$ parameter space for three light Majorana neutrinos plotted against lightest neutrino mass $m_{light}$ (left), the sum of neutrino masses $\Sigma$ (centre), and the effective neutrino mass $m_\beta$ (right). The horizontal bands show the upper limits obtained by GERDA (blue) and the combination with all leading experiments (grey), which are listed in Table 2.2. The width is given by the unknown CP-violating Majorana phases (dark shading) and by the current $3\sigma$ intervals of the neutrino oscillation observables from NuFIT [27] (light shading). The vertical limits come from cosmology, an extended model bound, and the KATRIN experiment [51–53]. The nuclear matrix elements to deduce the limits are from [28]. Figure from [49].

Together, these state-of-the-art experiments have set progressively stronger constraints on the $m_{\beta\beta}$ parameter space to 66–155 meV, getting closer to the unveiling of the true nature of the neutrino [49]. Figure 2.4 shows the upper limits on $m_{\beta\beta}$ obtained by GERDA and the complementary combination of its results with all leading experiments in the field. A large part of the degenerate region has been excluded and modern physics is on the brink of probing the inverted neutrino ordering.

After setting the standard in median sensitivity, GERDA underwent a month-long upgrade, starting in April 2018. The central string containing non-enriched natural detectors, that are the topic of Chapter 3, was lifted up and the natural diodes were replaced with five new Inverted Coaxial detectors, which are described in Chapter 4. As a result, the active mass was increased by 9.5 kg, allowing for an even faster exposure build-up. The exposure history of GERDA is reported in Figure 2.5, depicting the achieved exposure, the upgrade break, and the projection into the future.

Moreover, a denser fibre shroud was installed, as shown on the right in Figure 2.2, increasing the light yield two-fold. In addition, the high voltage and signal cables were replaced with lower activity ones in an effort to reduce the $^{214}$Bi influence on the experiment established in a $\gamma$-line study, reported in Section 3.2.5. This
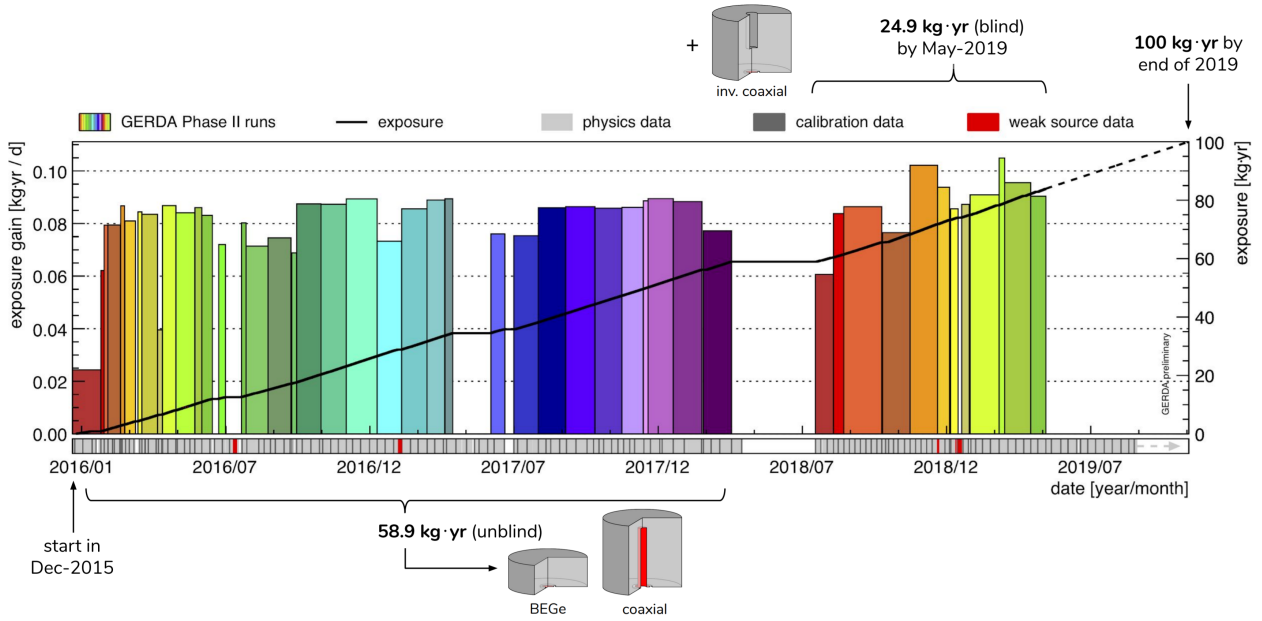
FIGURE 2.5: GERDA Phase II exposure history, starting in December 2015 and acquiring 59.8 kg·yr (81.4 kg·yr combined with Phase I) until the last unblinding in May 2018. Afterwards the experiment received an upgrade in form of additional germanium detectors: Inverted Coaxial detectors of Chapter 4. The experiment is predicted to achieve 100 kg·yr exposure by the end of 2019. Figure from [54].

leads to the prediction that GERDA will be able to further improve upon its background index around $Q_{\beta\beta}$ for its final unblinding with 100 kg·yr of exposure. Already, the mean expected background with this design exposure of 100 kg·yr is below one event at $Q_{\beta\beta}$, making GERDA the first *background-free* experiment in the field [45]. The sensitivity of such a background-free experiment with excellent energy resolution grows linearly with the exposure, as evidenced by Equation 2.3, unlike competing experiments, whose sensitivities exhibit a square root proportionality.

This effect is due to the calculation of the half-life $T_{1/2}^{0\nu\beta\beta}$ sensitivity as an expression of the time to collect a number of signal events $n_{sig}$ equal to the uncertainty on the background event count $n_{bkg}$, with [24]

$$n_{sig} = \frac{1}{T_{1/2}^{0\nu\beta\beta}} \frac{N_A \cdot \ln 2}{m_a} \cdot f_{enr} \cdot f_{AV} \cdot \varepsilon_{0\nu\beta\beta} \cdot \mathcal{E} ,$$

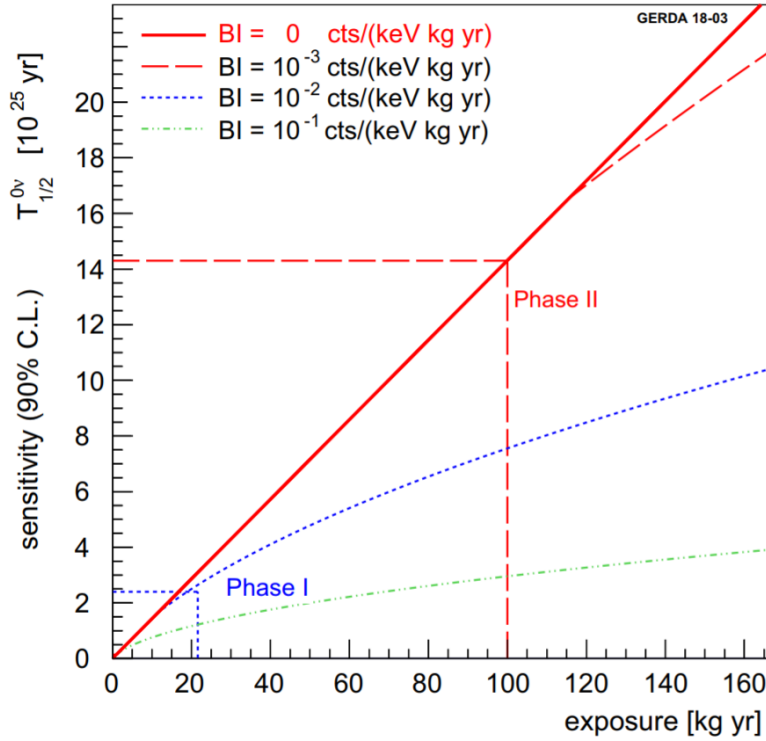$$n_{bkg} = BI \cdot \Delta E \cdot \mathcal{E} ,$$

$$(2.1)$$

FIGURE 2.6: Projection of the Gerda median sensitivity depending on Background Index (BI). The reason for the upgrade from Phase I to Phase II was the need for an order of magnitude lower background index to remain in the linearly scaling regime. By achieving such a $10^{-3}$ counts/(keV · kg · yr) background index at $Q_{\beta\beta}$, the experiment will stay in the linear regime until its design exposure of 100 kg·yr is attained. Figure from [42]

and, given the Poisson distribution of $n_{bkg}$, substituting

$$n_{sig} = \sqrt{n_{bkg}} , \tag{2.2}$$

amounting to

$$T_{1/2}^{0\nu\beta\beta} = \frac{N_A \cdot \ln 2}{m_a} \cdot f_{enr} \cdot f_{AV} \cdot \varepsilon_{0\nu\beta\beta} \cdot \sqrt{\frac{\mathcal{E}}{BI \cdot \Delta E}} \overset{BI \cdot \Delta E \ll \mathcal{E}}{\propto} \frac{\mathcal{E}}{BI \cdot \Delta E} , \tag{2.3}$$

where $T_{1/2}^{0\nu\beta\beta}$ is the half-life, $N_A$ the Avogadro number, $m_a$ the atomic mass, $f_{enr}$ the detector enrichment fraction, $f_{AV}$ the detector active volume fraction, $\varepsilon_{0\nu\beta\beta}$ the $0\nu\beta\beta$ detection efficiency after analysis cuts, BI the background index, $\Delta E$ the energy resolution, and $\mathcal{E}$ the exposure.

Figure 2.6 depicts how the median sensitivity scales linearly up to the goal exposure due to the low background index of GERDA. This background-free
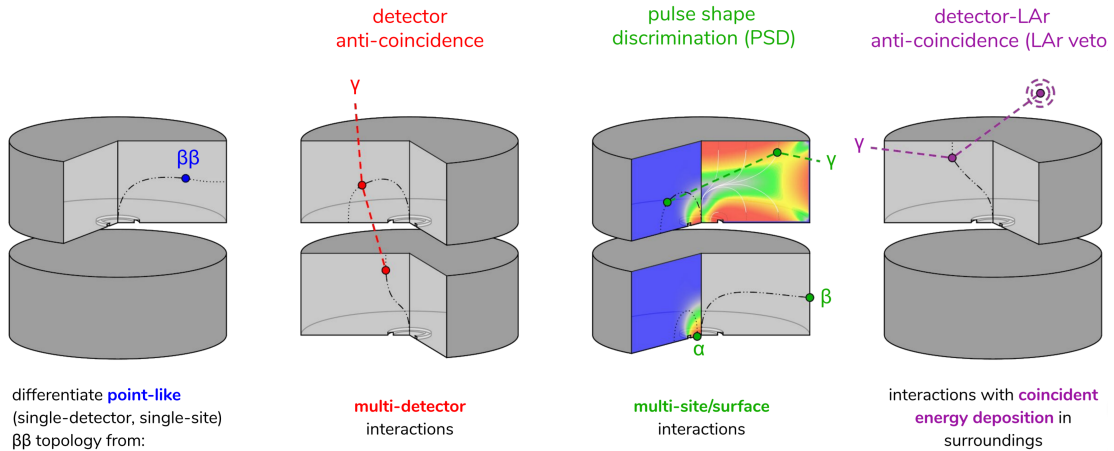
FIGURE 2.7: Active background reduction techniques employed in GERDA: SSE (left) event topology discrimination from MSEs through detector anti-coincidence (second from left), PSD (second from right), and detector LAr anti-coincidence veto (right). Figure from [54].

environment was achieved through several techniques: The first was the minimisation of the radioactivity in close proximity to the detectors by meticulous material selection based on screening results. The detectors assist each other through anti-coincidence, while PSD significantly lowers the remaining background after analysis cuts. Last but not least of the techniques is the underground operation with additional water and LAr shielding and active vetoing through light detection. Figure 2.7 shows a schematic of the active background reduction techniques.

Phase II has thus proven that the techniques of background suppression through direct immersion in LAr, the detection of the LAr scintillation light, and the excellent pulse shape performance of the BEGe type germanium detectors lead to an order of magnitude superior background index at $Q_{\beta\beta}$, normalised by energy resolution, in comparison to experiments using other isotopes.

## 2.3 The LEGEND Project

The success of the GERDA concept inspired the formation of LEGEND (Large Enriched Germanium Experiment for Neutrinoless $\beta\beta$ Decay), a new global collaboration designing the next generation germanium detector array with the goal of reaching one ton of germanium directly submerged in LAr [41]. The GERDA Collaboration, the Majorana Collaboration (with the Majorana Demonstrator

as one of the leading experiments listed in Table 2.2), and many additional institutions, based all over the world, have decided to join forces to build a more sensitive germanium-based detector array. In its first phase, 200 kg of germanium detectors will be deployed inside the GERDA cryostat at LNGS with the aim to reach a median sensitivity of $10^{27}$ yr. In the second phase, the goal is to build an experiment featuring one ton of $^{76}$Ge detectors, unlocking a discovery potential at a half-life beyond $10^{28}$ yr. Table 2.3 summarises the achievement of GERDA in relation to the goals of LEGEND. In order to achieve these sensitivities in a background-free regime, the background indices have to be lowered by around an order of magnitude in each phase. This highlights the significance of improving the background reduction techniques, such as background source location identification, as presented in Chapter 3.

| Experiment | Active Mass [kg] | BI [counts/(keV·kg·yr)] | $O(\mathcal{S}(T_{1/2}^{0\nu\beta\beta}))$ [yr] |
|---|---|---|---|
| GERDA (current) | 45 | $10^{-3}$ | $10^{26}$ |
| LEGEND-200 (projected) | 200 | $2 \cdot 10^{-4}$ | $10^{27}$ |
| LEGEND-1000 (projected) | 1000 | $3.5 \cdot 10^{-5}$ | $10^{28}$ |

TABLE 2.3: Comparison of GERDA and projected goals of LEGEND in terms of background indices to scale linearly with exposure, enabling the order of median sensitivity on the $0\nu\beta\beta$ decay half-life of $^{76}$Ge [42, 49, 55].

To obtain such a large germanium detector mass, a new detector type with equally outstanding PSD capabilities, but much larger size was explored. Five of these new Inverted Coaxial detectors were characterised for GERDA and their active volume fraction and active mass were determined in the framework of this thesis in Chapter 4. In the future, these new detectors will serve as the backbone of the search for the $0\nu\beta\beta$ decay.

## 2.4   Particle Detection with Germanium Diodes

The germanium detectors in GERDA are crystal diodes operated with an applied reverse bias high voltage to deplete them. They feature a groove, separating the positively biased inner p+ readout electrode from the outer grounded n+ electrode. Charged particles and photons ionise the germanium crystals, producing charge carriers in the conduction band proportional to the incident energy.

Under an applied reverse bias voltage on the semiconductor, the electrons and holes drift towards the electrodes. The resulting current can be measured by the readout electrode [56].
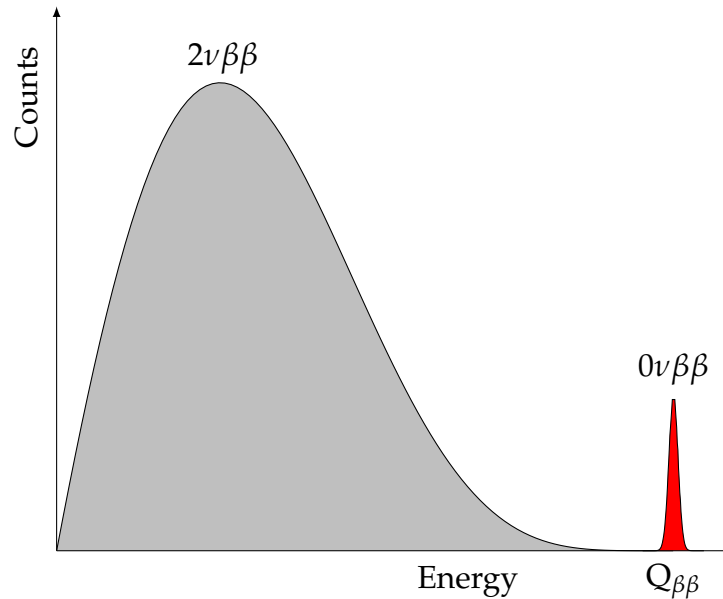


FIGURE 2.8: Theoretical spectrum of the summed energy of the detected electrons separating double beta decay (gray continuum, $2\nu2\beta$) and neutrinoless double beta decay (red peak, $0\nu2\beta$). The maximum energy peak is only observed for the neutrinoless case and is located at $Q_{\beta\beta} = (2039.006 \pm 0.050)$ keV [57].

A double beta decay produces two electrons, which can then be detected by the germanium diodes. The neutrinos leave the detector without energy deposition. A continuum is observed for the case of two neutrinos additionally carrying away a variable amount of the total energy produced in the decay. If the neutrinos however annihilate off-shell, the maximum energy is fully distributed to the electrons. The measured energy sum of the two electrons thus appears differently in the spectrum, depending on the event topology, as visualised in Figure 2.8. In the energy sum, the $0\nu\beta\beta$ decay would thus be measured as a sharp peak at the total reaction energy $Q_{\beta\beta}$ [6]. For $^{76}$Ge, it is located at $(2039.006 \pm 0.050)$ keV [57].

This peak is the signature that the GERDA experiment is searching for. The background in that region needs to be perfectly understood and minimised, as described in Section 2.6. The germanium diodes play the parts of the sources – by being isotopically enriched in $^{76}$Ge to $> 86\%$ – and the detectors simultaneously [7, 42].

Thermal excitations introduce electrons from the valence band into the conduction band, which can result in a leakage current. This effect needs to be

minimised as it mimics a real signal [56]. In GERDA, the germanium diodes are thus kept at temperatures of around 86 K by the LAr in the cryostat. Their measurement signals are guided to radio-pure low-noise cryogenic pre-amplifiers that are located approximately 50 cm above the array. On the outside, they are passed into Flash ADC (FADC) channels, where they are converted for digital processing [6, 7, 42, 43].
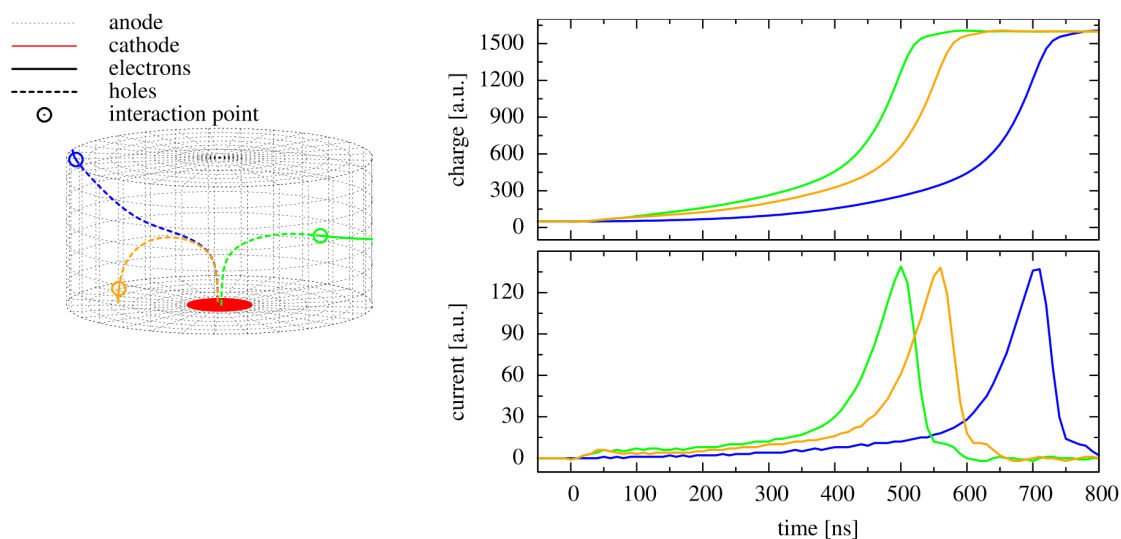


FIGURE 2.9: Three trajectories (blue, yellow, green) inside a Broad Energy Germanium (BEGe) detector are shown (left) stemming from interactions (circle) in the bulk volume. The produced holes (dashed lines) drift towards the p+ readout electrode (red disk). The electrons (continuous line) move towards the n+ electrode (surface of the cylinder, dotted). Induced charge and current time evolution (right) for the different paths are of identical characteristic shape, but differ in rise time. Figures from [58].

There are three types of high-purity germanium detectors employed in GERDA: Coaxial, the more advanced Broad Energy Germanium (BEGe), as well as the new Inverted Coaxial (IC) detectors. They are all cylindrical in shape, but the first have a central hole almost as long as the detector height, acting as the readout electrode, while the other two have a small concentric circle as the cathode, called a point contact readout electrode, that collects the drifting holes produced in the interactions. The left side of Figure 2.9 shows the schematic view of three electron-hole trajectories inside a BEGe detector. Their characteristic paths follow the applied electric field. The field strength increases dramatically in the vicinity of the readout electrode as the p+ contacts of BEGe and IC detectors are small when compared to the outer dimensions. Independent of event topology, a characteristic pulse shape is induced. The identical shape is observed for the time evolution of the induced signals, on the right of Figure 2.9. The charge and

current pulses, which correspond to the three trajectories, are shown on the top and bottom respectively. Far away from the cathode, the induction is much more attenuated and the different drift paths differ only in a variation of their rise time depending on the drift length.

The uniformity of the measured sharp signal peaks can be exploited with the help of PSD. Double beta decay events are a very local phenomenon. In germanium, the range of an electron with 1 MeV kinetic energy is around 1 mm [59]. The two involved electrons thus deposit their energies in the bulk volume of the detector close to the original decay, which makes them Single-Site Events (SSEs). Background events are often depositing energy in multiple locations, such as $\gamma$-rays undergoing multiple Compton scattering inside the detector volume, resulting in Multiple-Site Events (MSEs). Figure 2.10 illustrates the concept with a schematic top-down view of a germanium detector for different event topologies and the corresponding induced charge and current waveform pulses. The distinction of SSEs and MSEs is exploited to effectively reduce the background [43, 58, 60]. MSEs yield separated measured current peaks in the germanium detector, while SSEs create only a single dominant one. From the shape of the signal pulse, the original event topology can be inferred. In practice, the maximum measured current amplitude A is taken in the ratio to the total energy E, leading to the A/E classifier. For MSEs, where the current signal is divided up into multiple peaks, a lower A/E classifier is obtained than for SSEs.

Fast pulses with a higher A/E classifier are obtained when $\alpha$- or $\beta$-particles deposit energy on the p+ electrode. Slow pulses are produced due to charge diffusion processes into the Transition Layer when $\beta$-particles enter the outer n+ electrode, which is much thicker, such that $\alpha$-particles cannot penetrate. The Transition Layer is created during the production of the n+ electrode through thermal diffusion with lithium. The topic of Section 4.3.2 is the Transition Layer found in IC detectors, while Section 5.3.3 simulates the A/E classifier of said Transition Layer. Due to the point contact electrode, BEGe and IC detectors possess superior SSE to MSE discrimination properties and thus provide a major background reduction [58, 60].
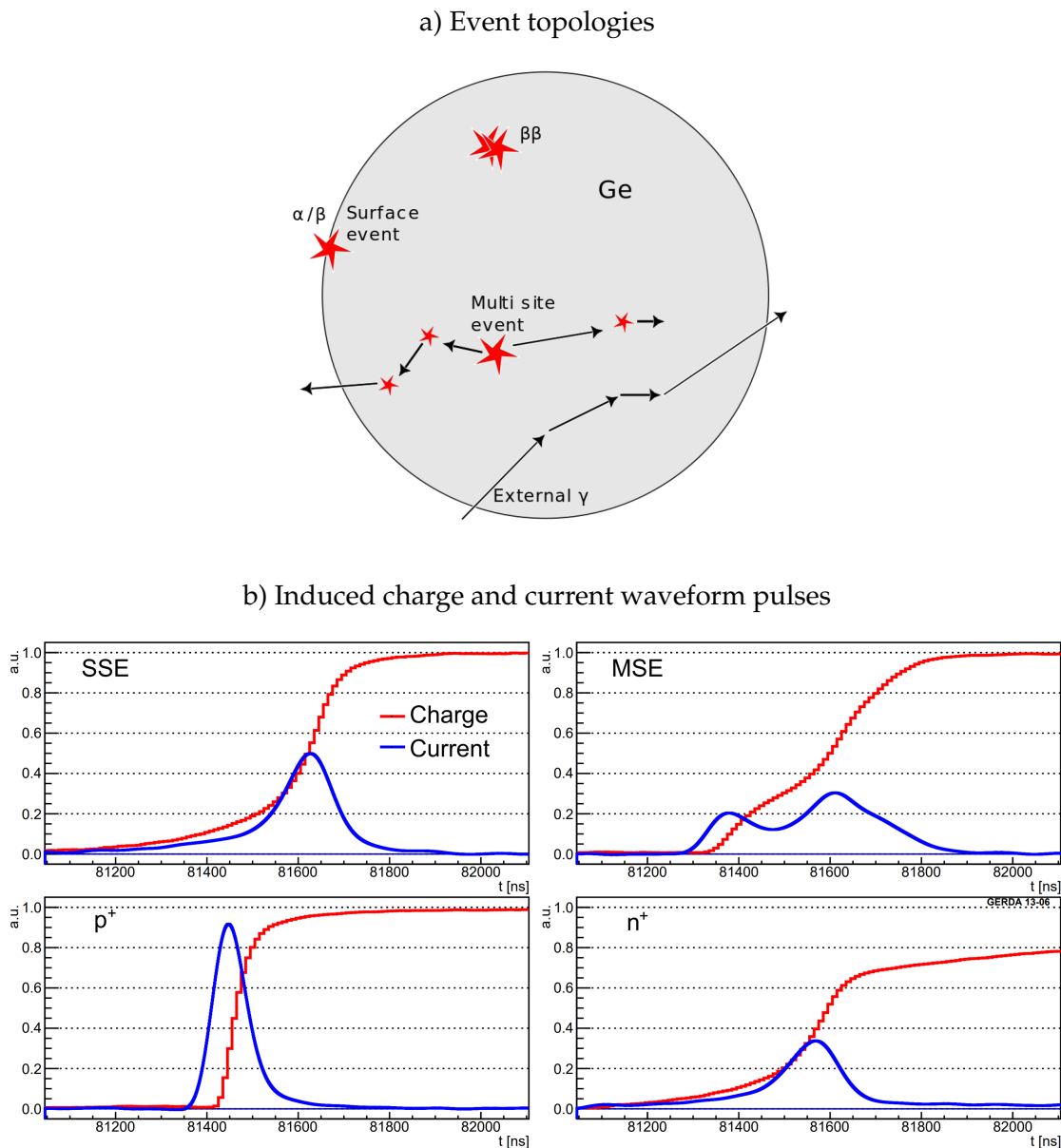
a) Event topologies



b) Induced charge and current waveform pulses



FIGURE 2.10: Event topology discrimination: The double beta decay ($\beta\beta$) of $^{76}$Ge is a bulk Single-Site Event (SSEs) that induces a single current peak. Single $\alpha/\beta$ decays are surface events on the n+ electrode (slow pulses) and p+ electrode (fast pulses), respectively. Multiple-Site Events (MSEs) can originate from outside or inside the germanium and interact in multiple locations in the detector, inducing multiple current peaks. Additionally, they can travel into another diode or the LAr and can be vetoed through anti-coincidence. Figure from [60].

## 2.5 Calibration of Germanium Detectors

In the GERDA Collaboration, the main responsibility of the University of Zurich group is the calibration of the germanium detectors. Sealed radioactive sources are lowered during calibration runs from above into the LAr on a motorised steel band using the Source Insertion System (SIS) in the clean room [61, 62]. Table 2.4 summarises the calibration procedure.

| Action | Source location |
| --- | --- |
| Deactivate PMTs | 0 m (initialised; clean room) |
| Start calibration run | 0 m (clean room) |
| Lower source | -8.570 m (bottom of array) |
| Raise source | -8.415 m (centre of array) |
| Raise source | -8.220 m (top of array) |
| Raise source | 0 m |

TABLE 2.4: Calibration procedure showing an individual source's chronological location in respect to the initialised position in the clean room (at 0 m) and order of performed actions. At each calibration location, the array is exposed for 20 minutes to the source, making a calibration run last 3 hours in total.

The main calibration is performed weekly, employing three low neutron emission $^{228}$Th sources. $^{228}$Th exhibits several strong peaks around the region of interest and throughout the energy spectrum, while offering an adequately long half-life of 1.91 yr [63]. Due to the precise knowledge of the $\gamma$-line energies from literature, the energy spectrum can be accurately interpolated throughout the full range [63]. Another benefit of the regular calibrations is the monitoring of the energy scale stability by $\gamma$-line position evolution comparison between ADC and calibrated energy throughout runs. In addition, the energy resolution of the detectors at $Q_{\beta\beta}$ for the $0\nu\beta\beta$ decay analysis is estimated from calibration data.

A key factor of the $^{228}$Th usage is the exploitation of the $^{208}$Tl peak at 2615 keV and the detector effects it creates. Since their initial energy is above the 1022 keV electron and positron rest mass sum, these $\gamma$-particles can undergo pair production inside the germanium. While the produced electron deposits its energy directly, the positron immediately annihilates with an electron in the crystal, releasing a photon pair with 1022 keV total energy. The highest probability is that both photons are reabsorbed, creating the large Full Energy Peak (FEP) at 2615 keV. If one or both photons escape the finite detector, 511 keV is lost for each photon, forming the Single Escape Peak (SEP) at 2104 keV and Double

Escape Peak (DEP) at 1593 keV, respectively. As a consequence, the DEP topology provides a large library of SSEs. This fact is used in several analyses that require pure SSE events, such as the verification of simulated SSE waveforms in Chapter 5.

To measure enough events in the calibration time frame, the $^{228}$Th sources need to possess an activity of at least 8 kBq or more to allow for low uncertainty peak fits. Activities above 40 kBq can lead to a high amount of pile-up events. Chapter 6 reports the production and characterisation of new low neutron emission $^{228}$Th sources with suitable activities. They are consequently in use as the main calibration sources of the GERDA experiment.

## 2.6  Background Prediction prior to Blinding

The $0\nu\beta\beta$ decay is evidenced by a peak at $Q_{\beta\beta}$ of energy 2039 keV, thus the primary goal of the experiment is to achieve the lowest possible background particularly in that region. The GERDA Collaboration blinded a range of $Q_{\beta\beta} \pm$ 20 keV for each new dataset to ensure an unbiased analysis of the background before revealing the region of interest. Figure 2.11 shows a representation of these defined energy windows. The blinded window is displayed in yellow. The background outside the window was used to fix the calibration parameters, the quality cuts, and the background model [43, 64]. The GERDA background model is explained further in Chapter 3.
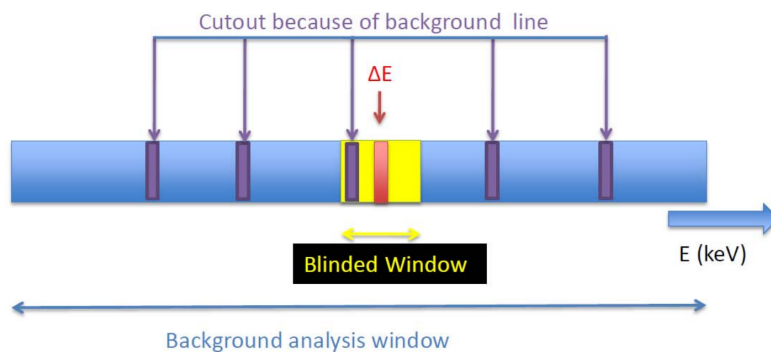


FIGURE 2.11: Representation of the energy windows used in the blind analysis of the GERDA Phase I energy spectra. The size of the blinded window (yellow) is 40 keV. The full energy range (blue) covers 100–7500 keV. Purple cutouts of size 10 keV are excluded due to known $\gamma$ lines in the background model. Figure from [43].

The background index in the blinded window was estimated by an interpolation of the adjacent domains. This prediction for the background index inside the window was then successfully tested for consistency after unblinding two 15 keV broad sidebands. A region of $Q_{\beta\beta} \pm 5$ keV remained blinded (the red region labelled $\Delta E$ in Figure 2.11) [43]. The latest unblinded results of GERDA are shown in Figure 2.3.

## 2.7 Liquid Argon Veto System

The high purity LAr, surrounding the germanium detector array, greatly decreases the $\gamma$-ray background from environmental radioactivity with a suppression factor on the order of $10^3$ at $Q_{\beta\beta}$ [65]. The cryostat is additionally reinforced with an inner copper shield that reduces the amount of $^{42}$K ions coming from $^{42}$Ar decays [7, 42].

In Phase II, a cylindrical volume of LAr inside the cryostat is used as an active veto. A schematic illustration of the veto surrounding the germanium detector array is shown in Figure 2.1. In response to energy deposits by $\gamma$-rays or electrons, LAr generates scintillation light. The scintillation light wavelength of 128 nm is in the VUV spectrum and therefore below the threshold of the radiative transmissibility of PMT windows. Two copper shrouds lined with wavelength shifting reflector foils made from TPB coated Tetratex are installed around the top and bottom PMT array [66]. The scintillation light is hence converted to a higher wavelength before reaching the PMTs. Nine low radioactivity 3-inch PMTs detect light from the top and seven from the bottom of the array [43, 65, 66].

The central part of the cylinder features a curtain of 810 wavelength shifting fibres, also coated with TPB, that are connected to SiPMs for optimal light detection efficiency. Events observed by this hybrid system in coincidence with the germanium detectors can therefore be vetoed. This reduces the background greatly, as external events and even a fraction of germanium MSEs traverse the LAr [43, 65].

## 2.8   Cherenkov Detector Muon Veto System

The mountains of Gran Sasso provide an overburden of 1400 m deep rock. This corresponds to around 3500 m of water equivalent shielding. The purified water around the experiment moderates and absorbs neutrons and suppresses external $\gamma$-radiation. High energy cosmic ray muons, that arise from $\pi$ and *K* decays in the atmosphere, however, can penetrate the rock and concrete surrounding the experiment and interact with the used materials. The muons traverse the tank with a velocity faster than the speed of light in water. The resulting Cherenkov radiation along their paths is then observed by 40 8-inch PMTs on the walls of the tank, and additional 20 on the bottom, and 6 beneath the cryostat for a total of 66 PMTs. Incoming muons from the top above the cryostat are detected by a layer of plastic scintillators above the clean room. The purified water tank and the outside of the cryostat are lined with a wavelength shifting reflector foil, which shifts the Cherenkov light from the UV into the optical range [6].



FIGURE 2.12: Inside the empty GERDA Cherenkov muon veto system water tank of 10 m diameter. 66 PMTs on the outer walls detect the Cherenkov light produced by incoming muons. The LAr cryostat is located in the center.

In conjunction with the LAr veto system, such events can be tagged as muons. The muon detection efficiency for Phase I with only the Cherenkov detector muon veto was around 98% [6]. Germanium detector events in coincidence can be rejected with a muon quality cut.

# Chapter 3

# GERDA Enriched and Natural Detector Background Model

The goal of GERDA was to achieve a background-free regime for its region of interest over the full acquired exposure to allow for linear scaling of the sensitivity on the half-life of the $0\nu\beta\beta$ decay. The prediction of the spectral shape of the background in the blinded region of interest to conclude the background index necessitated the prior modelling of all background sources through MC simulation performed by a team of collaboration members. Then followed a combined fit of these backgrounds to the full energy spectrum prior to analysis cuts, as explained in Section 3.1.

In the process, the precise background source locations were identified, such as in the $\gamma$-line study presented in the framework of this thesis, as described in Section 3.2.5 for the case of the $^{214}$Bi source origin. The knowledge of the location of these residual impurities will enable LEGEND to develop background reduction techniques to reach a background index of $0.6\,\text{counts}/(\text{FWHM} \cdot \text{t} \cdot \text{yr})$ and thus a background-free regime [41]. The $^{214}$Bi source origin identification of this work was made possible by the creation of a background model for the natural non-enriched Coaxial type germanium detectors in Section 3.2.2, capitalising on their order of magnitude lower natural abundance of $^{76}$Ge. Prior to that, their detector stability had to be investigated to produce a high quality dataset, as explained in Section 3.2.1. In addition, the activities of $^{39}$Ar and $^{85}$Kr were obtained with the model in Section 3.2.3 and Section 3.2.4, respectively. In the last part, a conclusion and the impact on other analyses are presented.

## 3.1 GERDA Background Model

For the background model of GERDA, all interactions depositing energy in the germanium detectors which did not stem from the $0\nu\beta\beta$ decay signature of $^{76}$Ge at 2039 keV were regarded as experimental background. This included for example natural radioactivity of parts in the vicinity of the detectors, such as $^{214}$Bi and $^{214}$Pb stemming from the decay chain of $^{238}$U. Another set of $\beta/\gamma$-induced background events originated from the $^{232}$Th decay chain, namely $^{212}$Bi, $^{212}$Pb, $^{208}$Tl, and $^{228}$Ac. In a study by the GERDA Collaboration, only upper limits were found for the $^{238}$U and $^{232}$Th bulk content of the detectors [67]. Furthermore, the $^{60}$Co background from cosmogenic activation of copper components of the experiment, chosen for their high radiopurity, needed to be considered. Any significant cosmogenic production of $^{60}$Co and $^{68}$Ge in the detectors themselves had been avoided through underground storage with only brief windows of transportation, making their contributions to the background model negligible. Another source of background was posed by the omnipresent $^{40}$K in all materials and $^{42}$K as a decay product of the cosmogenically induced $^{42}$Ar in the LAr of the cryostat. The germanium detectors were shielded from the majority of the $\alpha$-background through their lithium diffused n+ electrode on the order of around 1 mm thickness on almost the entire outer surface. Chapter 4 describes this concept further. The only penetrable surface for $\alpha$-particles was the boron doped p+ readout electrode of around 0.5 μm thickness. In the process, the inevitable energy loss lead to a strong low energy tails in the $\alpha$-model consisting of daughter decays of the $^{226}$Ra chain in the $^{238}$U series, such as $^{222}$Rn and predominantly $^{210}$Po.

The range of the background model was set on the lower end to 565 keV, just above the $^{39}$Ar $\beta$ spectrum, to exclude the influence of $^{39}$Ar and $^{85}$Kr [64]. On the upper end, the $^{210}$Po $\alpha$-peak at 5304 keV coincides with the highest measured event energies.

The experimental backgrounds were modelled independently and with varying source locations through MC simulations of the full germanium detector array using the MaGe framework based on Geant4 [68]. The resulting GERDA Phase II background model, shown in Figure 3.1, consists of 8 main background component groups and was a joint effort of the collaboration [64]. The contribution in the framework of this thesis was the simulation of the high voltage cable
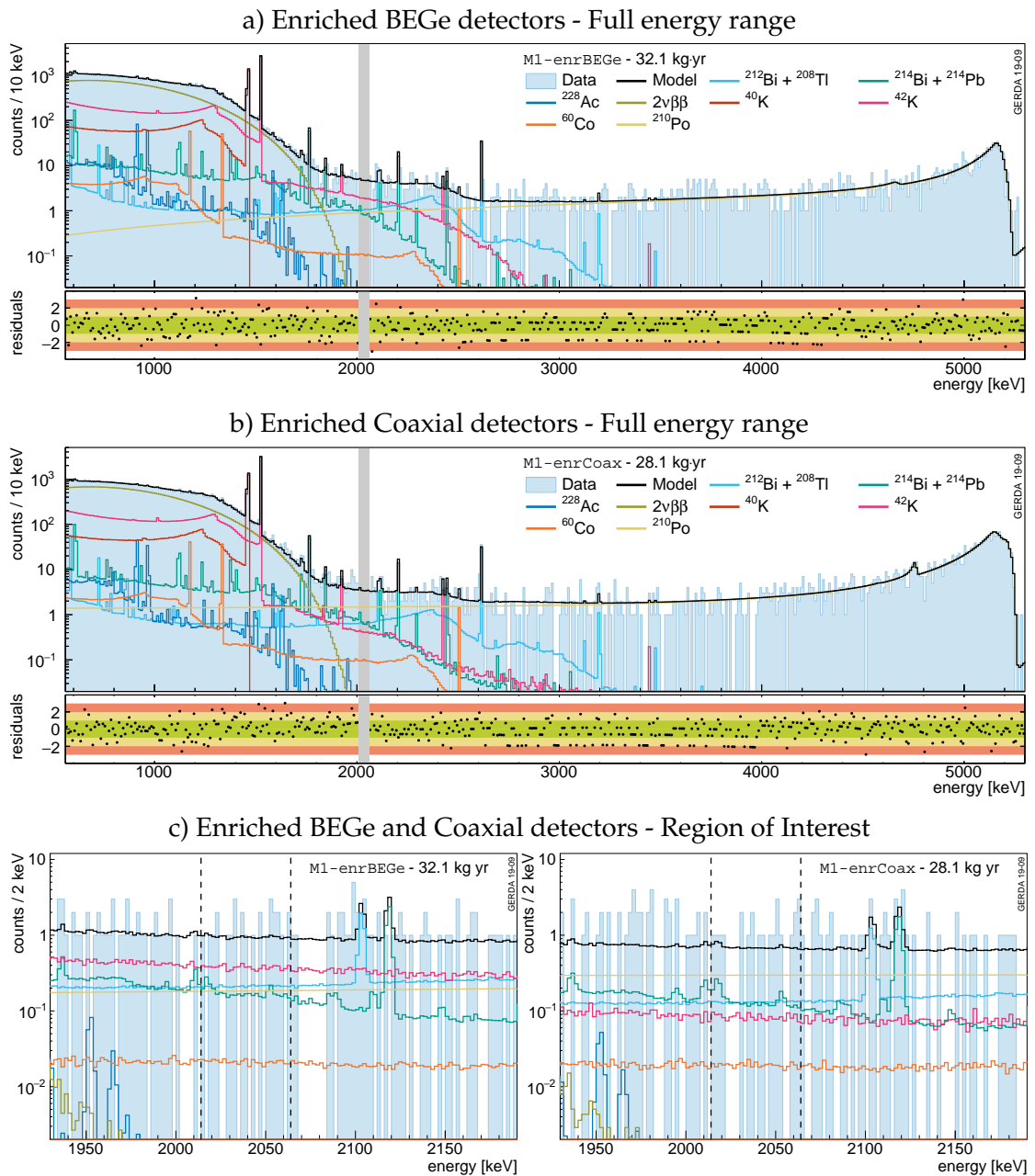
FIGURE 3.1: GERDA Phase II main background model (black) for the two different enriched detector types divided into different components (coloured). The model is a global fit to the blinded full energy spectra (a, b) that lead to a flat background prediction in the region of interest (c). The contributions were grouped by association, for example the $^{210}$Po group contains also $^{226}$Ra and its daughter nuclei emissions. The high voltage cable and mini-shroud components of the $^{214}$Bi & $^{214}$Pb background (green) were simulated in the framework of this thesis. [64].

and mini-shroud components of the $^{214}$Bi & $^{214}$Pb background sources and the determination of the $^{214}$Bi source origin through a $\gamma$-line study, described in Section 3.2.5. In addition, the MaGe framework was updated for the usage with the newest stable version of Geant4 (release 10.4 with CLHEP 2.3.4.4) which included several internal physics improvements for more accurate results [69].

The relative contributions of the simulated background sources were determined through a combined binned Bayesian fit to the experimentally measured energy spectrum with BAT (Bayesian Analysis Toolkit) [70]. The fit was performed for 32.1 kg·year of enriched BEGe and 28.1 kg·year of enriched Coaxial germanium detector type data. In the region of interest, the background model before analysis cuts yielded a background index of $16.04^{+0.78}_{-0.85} \cdot 10^{-3}$ counts/(keV·kg·yr) for the enriched BEGe and $14.68^{+0.47}_{-0.52} \cdot 10^{-3}$ counts/(keV·kg·yr) for the enriched Coaxial detector datasets [64]. The spectral shape in an energy range of $\pm 100$ keV around Q$_{\beta\beta}$ was determined to be flat, which lead to the final GERDA background index after PSD and LAr cuts of $0.4^{+0.6}_{-0.3} \cdot 10^{-3}$ counts/(keV·kg·yr) for enriched BEGe and $0.7^{+1.0}_{-0.5} \cdot 10^{-3}$ counts/(keV·kg·yr) for enriched Coaxial detectors [71].

## 3.2 Natural Detector Background Model and Analysis Avenues

In the 7 string set-up of the GERDA array, the 3 natural non-enriched coaxial type detectors GTF112, GTF32, and GTF45 were located in the central string, shown in Figure 3.2. Due to their lack of enrichment, they exhibited a 7.6% and thus an order of magnitude less natural abundance of $^{76}$Ge than the enriched detectors [6, 72]. This meant that they could not be used directly for the $0\nu\beta\beta$ analysis, but at the same time the $2\nu\beta\beta$ background was strongly suppressed. This opened up an avenue to study other background components in this energy range in more detail without their energy lines being covered up by the otherwise dominant continuum.

Since there were a number of background source spectra, each with their individual footprint, indiscernibly layered together, a background model for the natural detectors needed to be developed to determine their exact relative contributions. This was also a chance to extend the range of the background model

FIGURE 3.2: Left: Central string of the GERDA array, featuring the 3 natural non-enriched coaxial type detectors GTF112, GTF32, and GTF45. Right: Position of the central string surrounded by the other 6 strings in the clean room before lowering into the cryostat.

below 565 keV to the low energy region and retrieve accurate results of the cosmogenically produced $^{39}$Ar activity. On the upper end, the model ranges up to 5.5 MeV to cover the most important $\alpha$-contributions as well.

Another interesting, but so far neglected, low energy background dissolved in the LAr is the anthropogenic $^{85}$Kr. Its half-life is 10.8 yr and its signature is partly from a $\beta$ decay of maximum energy 687 keV, resulting in a continuum strongly degraded by the electrode thickness at this low energy [63]. The second decay channel is by $\beta$ emission of 173 keV followed by a $\gamma$-particle of energy 514 keV, creating the single large peak barely visible in the enriched detector spectrum [63]. Therefore the natural detector background model had the potential for much improved fits with lower uncertainties for both of these background sources. In the following, two analyses are presented: First, the specific activities of $^{39}$Ar and $^{85}$Kr were extracted. Secondly, the $\gamma$-lines of $^{214}$Bi were studied to identify its primary source location as an input for the enriched background model.

A better grasp of the low energy region became crucial as several analyses needed input on the previously not well understood low energy backgrounds below the background model lower threshold and below the artificially set 500 keV PSD one. For example, the estimation of the distortion of the $2\nu\beta\beta$ continuum

shape through other hypothetical decay channels, such as Majorons, is the most accurate if all backgrounds in the same energy range are well constrained [33].

For the main GERDA background model, an analysis was performed on the basis of the natural detector spectra to identify the background source location of $^{214}$Bi through a comparison of MC simulated peak ratios to data peak ratios.

### 3.2.1   Detector Stability Study and Quality Dataset Production

In order to create the natural detector background model, the natural detector dataset needed to be studied first, its times of detector energy instability removed, and then its data formats produced. Unlike the BEGe and Coaxial detectors, for which the collaboration had a designated data quality team, the natural detectors were omitted and waveforms and spectra had not been thoroughly investigated before. In the framework of this thesis, the natural detector stabilities were studied, using previously gained data quality expertise gathered with the other detector types. Starting from the beginning of Phase II with Run 53 in December 2015 and ending with the milestone Run 92 in February 2018, the study encompassed 799 days of data. The study enabled the optimisation of the dataset through the creation of new run configuration files (RunConfig) for each run. These files accounted for all times of instability signified through either pulser jumps, pulser drifts, or unstable $\gamma$-lines. This drastically reduced effects, such as peak broadening, that could significantly affect analysis results.

In total, 1.8 kg·yr of unstable natural detector exposure was identified, as illustrated in Figure 3.3, leaving a cleaner dataset of 9.1 kg·yr down from a raw 10.9 kg·yr to be analysed. This was subsequently implemented into the official GERDA data production cycle v04.00.

### 3.2.2   Natural Detector Background Model Combined Fit

The next step were surveys of the low energy region for continua and $\gamma$-lines stemming from contributions disregarded in the main background model and their locations. This entailed comparisons of LAr coincidence and anti-coincidence of direct line searches crossed with the correlation of detector positions. Additional MC simulations of $^{39}$Ar and $^{85}$Kr with $10^9$ events each were performed
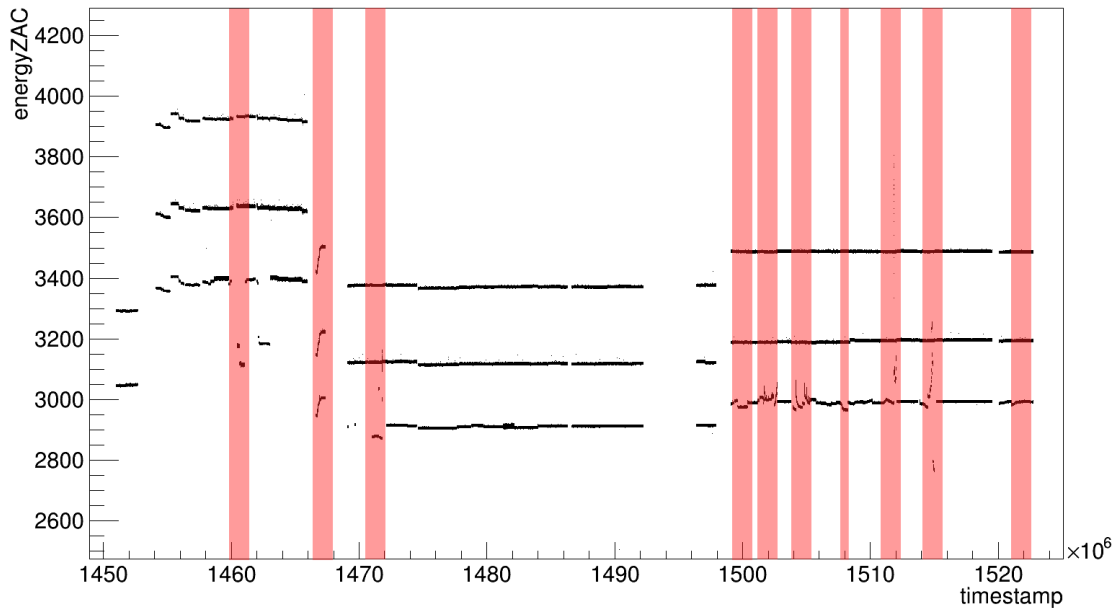
FIGURE 3.3: Natural detector dataset evolution through all of runs 53 – runs 92 signified by energy scale stability on the y-axis in units of reconstructed pulser energy and identifying times (red bars) that any of the natural detectors were set to anti-coincidence mode and thus taken out of the total dataset. This enabled the optimisation of the dataset and the removal of instability artifacts such as peak broadening.

with MaGe, assuming a uniform distribution within the LAr. For the minimal background model, shown in Figure 3.4, the following component groups were identified in the combined fit to the new natural detector dataset: $2\nu\beta\beta$, $^{214}$Bi, $^{214}$Pb, $^{212}$Bi, $^{208}$Tl, $^{228}$Ac, $^{40}$K, $^{42}$K, $^{39}$Ar, $^{85}$Kr, and an $\alpha$-model. The latter is comprised of $^{210}$Po and $^{226}$Ra chain daughter nuclei emissions on the p+ contacts. The $^{60}$Co component was of low significance and proved redundant in the minimal model, mainly because of the high bulk-to-surface ratio of the natural detectors and less copper in the vicinity of each detector due to the larger distance between diodes in the central string, as seen in Figure 3.2.

## 3.2.3   $^{39}$Ar Specific Activity Determination

The $^{39}$Ar $\beta$ spectrum clearly dominates the region below its endpoint at 565 keV in the natural detector background model due to the immersion of the germanium detectors in LAr. An effect to be noted is the artificial peak at exactly 150 keV in the spectrum, originating from a reduction of the trigger threshold starting in Run 87 from 150 keV down to 16 keV. The recording of this low energy
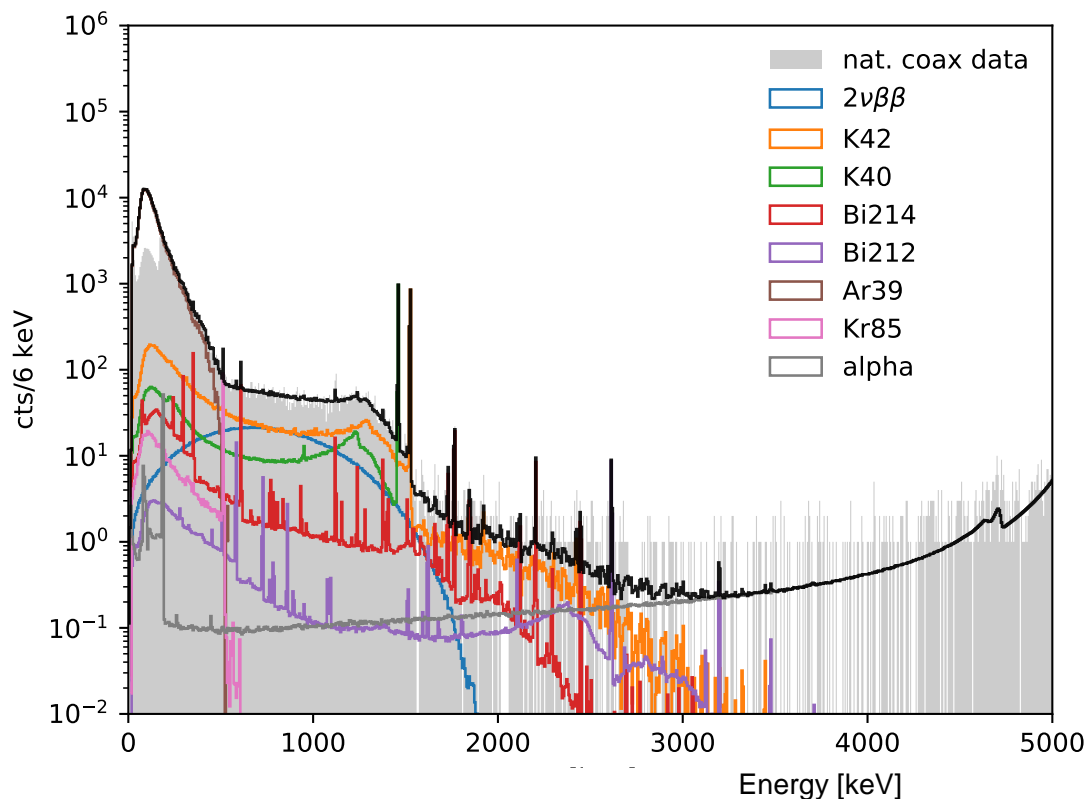
FIGURE 3.4: GERDA Phase II natural detector background model fit to data (light grey) with 8 components from Monte Carlo simulations over the whole energy range. For better visibility, some component groups are grouped together, such as $^{212}$Bi, $^{208}$Tl, and $^{228}$Ac or $^{214}$Bi and $^{214}$Pb. The $\alpha$-model is composed of $^{210}$Po, $^{226}$Ra, and daughter nuclei emissions. The artificial peak at 150 keV is due to the reduction of the trigger threshold starting in Run 87 down to 16 keV.

data together lead to even more accuracy on the $^{39}$Ar activity and a better fit of $^{39}$Ar with a lower p-value extracted from the dataset starting from Run 87 to Run 92. The $^{39}$Ar component extracted in this manner was then scaled and used as a set point in the final natural detector model over the full dataset. The natural detectors were found to be ideally suited for the activity estimation of $^{39}$Ar in the LAr of the experiment due to their large surface leading to a significantly higher event rate of $^{39}$Ar decays in comparison to BEGe detectors. The order of magnitude lower $2\nu\beta\beta$ component, however, was the main reason that lead to very stable $^{39}$Ar fits.

Since the range of an electron with 1 MeV energy in germanium is around 1 mm, the same order of the n+ electrode Dead Layer of the detectors, explained in Chapter 4, needed to be considered for the $\beta$ decay spectrum shape of $^{39}$Ar [73]. The n+ Dead Layer in the MC simulations was varied through geometrical fiducialisation in 0.2 mm steps and thus revealed to be the dominant factor for

the $^{39}$Ar activity uncertainty. Below 150 keV, the $^{39}$Ar spectrum is increasingly degraded by the Dead Layer as shown in Figure 3.5. The p+ Dead Layer variation had virtually no effect on the shape. Differences in fit range and bin count were small in comparison to the uncertainty induced by the n+ Dead Layer.
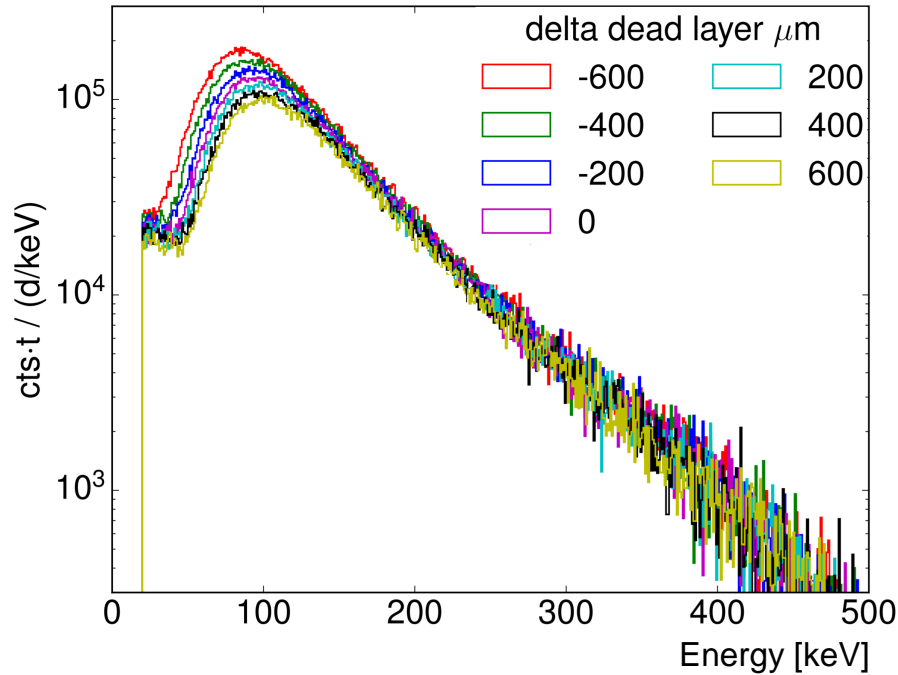


FIGURE 3.5: Variation of the n+ Dead Layer in 0.2 mm steps and its effect on the $^{39}$Ar spectrum shape, where 0 symbolises the initial Dead Layer size GERDA estimate. The region below 150 keV is increasingly degraded for higher Dead Layer sizes as lower energy $\beta$-particles deposit a majority of their energy without inducing a current.

The specific activity of $^{39}$Ar, averaged throughout data taking, was calculated by applying Equation 3.1.

$$A^{^{39}Ar} = \frac{w \cdot N_{sim}}{\rho \cdot V_{sim}} \, , \tag{3.1}$$

where $w$ is the fitted weight from the multiplication of the simulated spectrum with the uptime, $N_{sim}$ the number of simulated events to obtain the spectrum, $V_{sim}$ the simulated volume, and $\rho$ the density to retrieve the activity in units of Bq/kg. The statistical uncertainty was estimated from the free $^{39}$Ar component variation in the combined fit of the natural detector background model. The systematic uncertainty stems from the resimulation of $^{39}$Ar with detector Dead Layer thicknesses variation.

The analysis thus resulted in the estimation of the current specific activity of $^{39}$Ar in the LAr as

$$A^{^{39}Ar} = (1.17 \pm 0.04 \text{ (stat.)} \pm 0.06 \text{ (sys.))} \text{ Bq/kg} . \tag{3.2}$$

This result was compared after the fact to literature of a published $^{39}$Ar estimate by the WARP Collaboration and an earlier estimate based on GERDA Phase I data from Run 10 to Run 13 with a total live time of 100 days [74, 75]. The WARP experiment was a prototype two-phase argon drift chamber equipped with PMTs, searching for WIMP Dark Matter at LNGS [76]. As such, the WARP energy spectrum observed by the PMTs inside the 2 l detector featured a much lower energy resolution and, thus, individual components were much harder to identify. In addition, the energy thresholds of both literature studies were chosen to be higher, possibly decreasing the $^{39}$Ar fit accuracy, as evidenced by Figure 3.5. The Phase I result was based on a simplified approach with a fit model consisting of only an approximated flat distribution replacing the other backgrounds. The analysis presented in this work is consistent within 1 $\sigma$ significance with the values found in literature featuring the lowest systematic uncertainty. The activity estimates of GERDA and WARP are collected in Table 3.1.

| Dataset | Year | Threshold | $^{39}$Ar Specific Activity [Bq/kg] |
|---|---|---|---|
| This work | 2019 | 16 keV | 1.17 $\pm$ 0.04 (stat.) $\pm$ 0.06 (sys.) |
| GERDA Phase I | 2014 | 100 keV | 1.15 $\pm$ 0.05 (stat.) $\pm$ 0.10 (sys.) |
| WARP | 2007 | 100 keV | 1.01 $\pm$ 0.02 (stat.) $\pm$ 0.08 (sys.) |

TABLE 3.1: Overview of the results of the $^{39}$Ar specific activity analysis and earlier estimates based on Phase I data, as well as the results of the WARP Collaboration [74, 75].

For the dark matter detector DEAP-3600, using 3600 kg of natural atmospheric argon, a PhD thesis has recently reported a preliminary specific activity of 0.95 $\pm$ 0.03 Bq/kg, hinting that the $^{39}$Ar specific activity could be slightly lower [77].

Since the $^{39}$Ar originated from cosmogenic production in the atmospheric $^{40}$Ar that the LAr was derived from, the argon abundance ratio was compared to atmospheric measurements in literature [78]. The reported result was converted

into the corresponding $^{39}$Ar concentration in $^{40}$Ar, as follows

$$C = \frac{A^{\text{meas Ar}}}{A^{\text{pure Ar}}} = \frac{A^{\text{meas Ar}} \cdot T_{1/2} \cdot m}{N_A \cdot \ln(2)} \, , \qquad (3.3)$$

with C as the isotopic concentration, $A^{\text{meas Ar}}$ the measured specific activity of $^{39}$Ar in atmospheric argon, $A^{\text{pure Ar}}$ the specific activity of pure $^{39}$Ar, $N_A$ the Avogadro number, $T_{1/2}$ the known half-life, and m the mass. The values of these quantities are given in Table 3.2. This yielded an isotopic concentration of $^{39}$Ar in atmospheric argon as

$$C = (8.6 \pm 0.6) \cdot 10^{-16} \, , \qquad (3.4)$$

in good agreement with a previously established $(8.1 \pm 0.3) \cdot 10^{-16}$ value in atmospheric measurement literature [78].

| Parameters | Values |
|---|---|
| m | $38.964313 \pm 0.000005 \, \frac{\text{g}}{\text{mol}}$ [79] |
| $T_{1/2}$ | $(269 \pm 3)$ yr [63] |

TABLE 3.2: Parameters for the calculation of the isotopic concentration in Equation 3.3.

### 3.2.4  $^{85}$Kr Specific Activity Determination

When taking a closer look at the region between 400 keV to 1400 keV in the natural detector background model, as displayed in Figure 3.6, the $^{85}$Kr peak at 514 keV towers above the other contributions. For the enriched detector, in contrast, the peak was hard to discern from background fluctuations of the $2\nu\beta\beta$ component. At the same time, the zoom into spectrum highlights other previously buried peaks, such as from the $^{214}$Bi and $^{40}$K components. The clear visibility of the $^{85}$Kr peak in the natural detector spectrum was essential to estimate the specific activity of $^{85}$Kr.

In the first step of the analysis process, the simulated $^{85}$Kr spectrum had been found devoid of the 514 keV peak. The issue lay within MaGe, inside the Geant4 SteppingAction class that had been originally set to flag and kill daughter nuclei with a lifetime longer than 1 μs, without triggering their decay, to improve
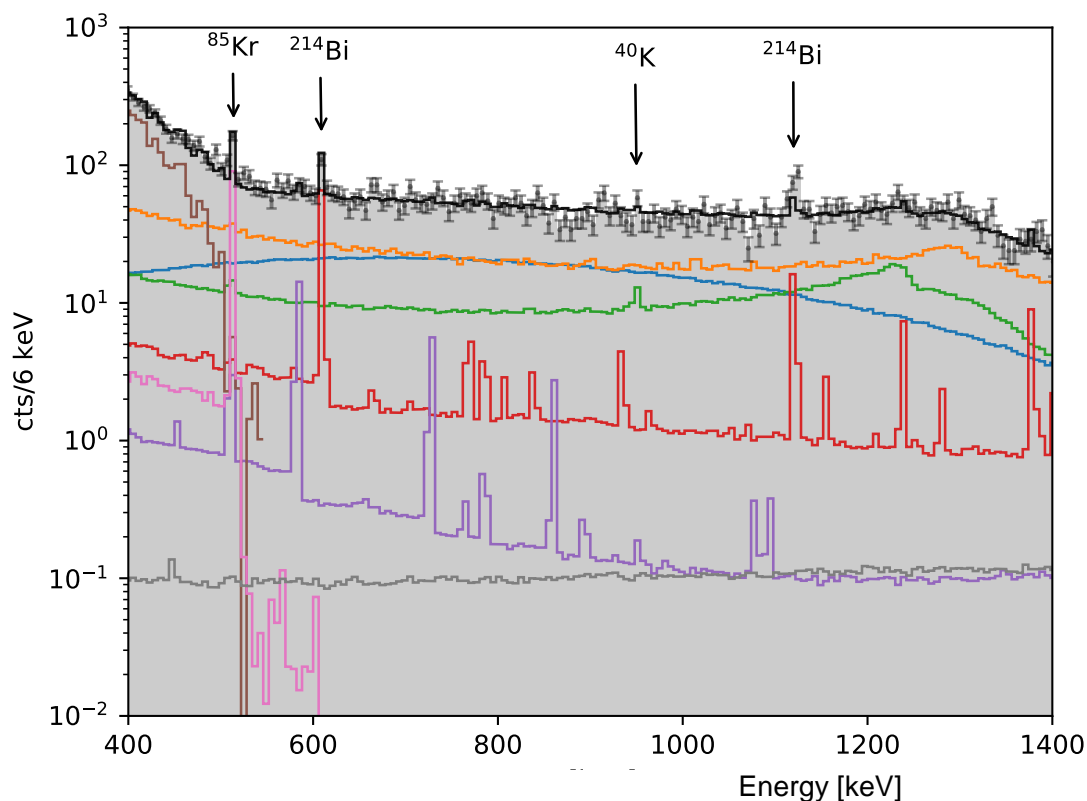
FIGURE 3.6: Zoom into natural detector background model combined fit to data (light grey) in the energy window of 400 to 1400 keV, highlighting $\gamma$-lines visible in the natural detector spectrum stemming from different background sources: 514 keV of $^{85}$Kr, 609 keV and 1120 keV of $^{214}$Bi, and the $^{40}$K escape peak at 950 keV from the 1461 keV main peak.

simulation performance. The $\beta$ decay of $^{85}$Kr to $^{85}$Rb, responsible for the 514 keV peak with a BR of 0.0043, however, takes 1.015 µs [63]. By increasing the flag threshold, the problem was thus resolved.

After creating the natural detector background model, the 514 keV $^{85}$Kr peak fit resolution was checked against the influence of the close-by 511 keV positron annihilation peak. By studying the spectrum after applying the LAr veto cut, the $^{208}$Tl peak was identified through its strong suppression by the cut. The survival rate of the 514 keV peak, on the other hand, is much higher due to the dissolution of $^{85}$Kr in the LAr, which is due to the increased likelihood of detector surface vicinity emission without inducing scintillation light on the way. Figure 3.7 depicts the natural detector data spectrum in relation to the spectrum after LAr cut. The peak was thus shown to be the real, well resolved $^{85}$K decay. This enabled the setting of a small 3 keV energy window to fit the $^{85}$Kr peak. This peak fit and its Gaussian variation was then used as in input into
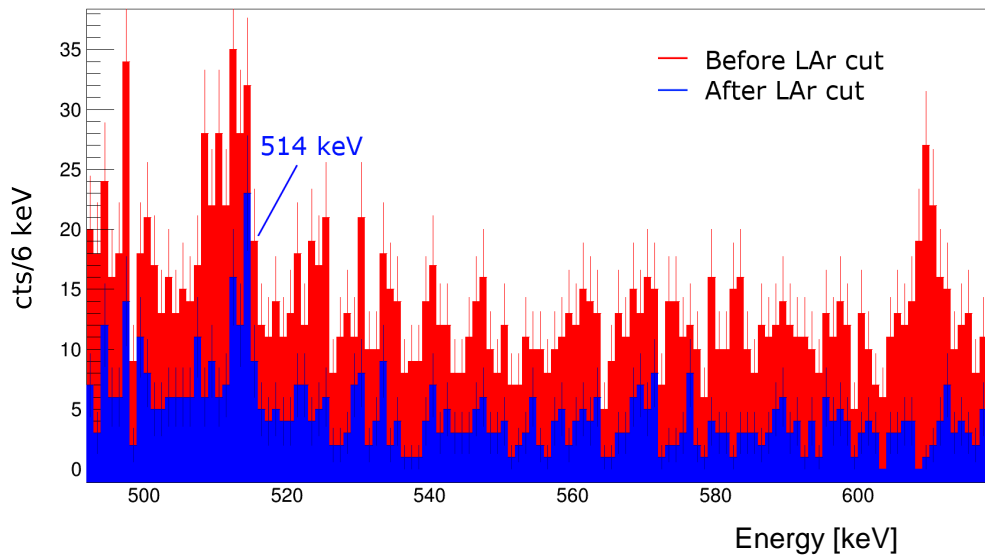
FIGURE 3.7: Comparison of the natural detector data spectrum before (red) and after LAr veto cut (blue). The identification of the 514 keV peak as $^{85}$Kr is aided by its increased survival ratio by the LAr cut in relation to the strongly suppressed positron annihilation peak at 511 keV.

the natural detector background model, constraining the statistical uncertainty for the variation in the free constrained $^{85}$Kr component in the natural detector background model combined fit. The systematic uncertainty on the $^{85}$Kr was calculated from Geant4 simulation effects mentioned previously and simulated volume to be 12%.

This allowed, thanks to the natural detector background model and by adapting Equation 3.1, the calculation of the current $^{85}$Kr specific activity in the LAr, averaged throughout data taking, resulting in

$$A^{^{85}Kr} = (0.84 \pm 0.12 \text{ (stat.)} \pm 0.1 \text{ (sys.)}) \text{ mBq/l} . \tag{3.5}$$

In comparison to the WARP result of $(160 \pm 0.130)$ mBq/l, a much lower uncertainty was achieved [76]. The $^{85}$Kr specific activity result of the DARKSIDE-50 experiment for underground argon lead to and estimate of $2.86 \pm 0.18$ mBq/l, but it is mentioned however that their source of $^{85}$Kr in the underground argon is not yet understood [80]. The result of this work suggests around $10^6$ atoms/l or a relative abundance of $10^{-19}$ in the LAr of the GERDA experiment. Since $^{85}$Kr is mainly anthropogenic, with a relative abundance in natural krypton from literature of around $10^{-11}$ (equal to 10 ppt) [81], this results in a $10^{-8}$ (equal to 10 ppb) contamination with natural krypton.

### 3.2.5 $^{214}$Bi Background Source Origin $\gamma$-line Study

In the main background model of GERDA Phase II, the origin of the $^{214}$Bi component was initially inconclusive. While the p+ electrode and nylon mini-shrouds were found in screening to be low significance locations, the high voltage cables, copper shrouds coated with Tetratex, and the SiPMs (Silicon Photomultipliers) were all indiscernibly dominant [64]. The screening results prior to the upgrade of GERDA to Phase II had yielded slightly higher activity numbers for the mean activity of the high voltage cables than for the other two, as evidenced by the screening entry in Table 3.3. However, due to the large uncertainty on the measurement, it remained unclear which of the locations was truly dominant [64].

| Location | Screening μBq/kg | Result | Global Mode μBq/kg |
|---|---|---|---|
| High voltage cables | $660 \pm 210$ | dominant | 560 |
| Tetratex coated copper shroud | $532 \pm 53$ | | 533 |
| SiPMs | $351 \pm 97$ | | 353 |
| Nylon mini-shroud | $43 \pm 13$ | | 45 |
| p+ (Coax) | – | | 1.05 |
| p+ (BEGe) | – | | 0.36 |

TABLE 3.3: Result of the $^{214}$Bi background component location $\gamma$-line study after inconclusive screening results and initial background modelling. The identification of the dominant influence of the high voltage cables served as a prior to induce the final global mode of the GERDA Phase II main background model [64].

For this purpose, a $^{214}$Bi $\gamma$-line study on the natural detector dataset was performed. All $^{214}$Bi $\gamma$-lines known from literature were studied through Bayesian fitting, employing the BAT library [63, 70]. Four $^{214}$Bi peaks, otherwise buried underneath the $2\nu\beta\beta$ continuum, were uncovered in the study of the natural detector energy spectrum and are partly shown in Figure 3.6. The ratios of the fit results with subtracted continuum background in relation to the most stable peak fit of the 609 keV line in the $^{214}$Bi spectrum were calculated. In the next step, the same ratios were extracted from the MC simulated $^{214}$Bi spectra originating in different source locations: High voltage cables, Tetratex coated copper shroud, and SiPMs. These ratios were then related in the analysis, as shown in Figure 3.8, to determine the dominant component location. The peak ratios from the $^{214}$Bi

MC simulations with the background source origin in the high voltage cables coincided the best to data for all uncovered $^{214}$Bi $\gamma$-lines. This $\gamma$-line analysis thus independently verified the cables in GERDA as the dominant $^{214}$Bi source location.
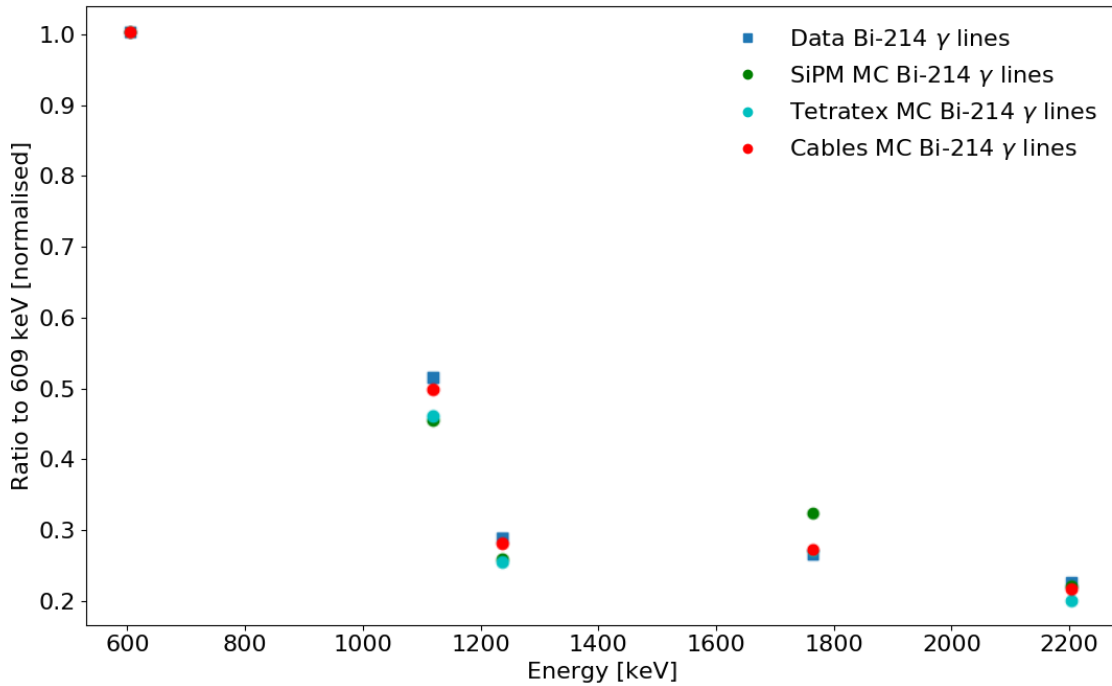


FIGURE 3.8: Ratios of $^{214}$Bi peaks in the optimised natural detector data energy spectrum (blue square) identified by a Bayesian fit to the 609 keV peak in relation to ratios from MC simulated origins (circles) to determine the dominant $^{214}$Bi source location: Contamination stemming from either SiPMs (green circle), Tetratex coated copper shroud (cyan circle), or high voltage cables (red circle). The high voltage cable source (red circle) exhibited the best match to data for each $\gamma$-line.

The identification in the natural detector dataset of the high voltage cables as the dominant background source location of $^{214}$Bi as a prior helped determine the $^{214}$Bi source origin hierarchy in the GERDA Phase II main background model. As a result, the background model predicted a BI at Q$_{\beta\beta}$ of $2.63 \cdot 10^{-3}$ counts/(keV·kg·yr) induced by the high voltage cables component of $^{214}$Bi before LAr veto and PSD cuts [64]. This is a substantial part of the total background index estimation of the background model at Q$_{\beta\beta}$ of $16.04^{+0.78}_{-0.85} \cdot 10^{-3}$ counts/(keV·kg·yr) before analysis cuts.

## 3.3   Conclusion and Outlook

In this chapter, the natural detectors' low natural abundance of $^{76}$Ge of only 7.6% and thus order of magnitude lowered $2\nu\beta\beta$ spectrum was exploited to extract a set of new information from topologies otherwise fully or partially obstructed by the continuum [72]. First, a high quality natural detector dataset was produced through an analysis of the detector stability over 799 days of data, starting from Run 53 in December 2015 to Run 92 in February 2018. This enabled the creation of the background model of the natural non-enriched detectors, exploring the energy region below the 565 keV threshold of the enriched detector background model. Consequently, competitive $^{39}$Ar specific activity results were determined in comparison to previous findings of GERDA Phase I and the WARP Collaboration [74, 75]. The uncovering of the 514 keV peak in the spectrum allowed for a stable fit of the $^{85}$Kr component and thus extraction of the specific activity in the LAr. In addition, the resulting LAr contamination with natural krypton was calculated in comparison to the relative abundance in natural krypton.

The dominant background source location of $^{214}$Bi was identified to be the high voltage cables through a $\gamma$-line study and ratio analysis as an input for the main GERDA background model. The MC modelling of all background sources and the combined fit lead to the prediction of a flat background in the blinded region of interest. This served to predict the background index from the side-bands around the blinded region in data, resulting in the achievement of the background-free regime in the region of interest and thus linear scaling of the $0\nu\beta\beta$ decay half-life sensitivity. With the better knowledge on the precise origin of background sources, LEGEND will be able to develop new techniques to tackle these impurities, such as even lower activity high voltage cables, before assembly of the experiment and thus reduce its background index even further to a predicted $0.6\,\mathrm{counts}/(\mathrm{FWHM}\cdot\mathrm{t}\cdot\mathrm{yr})$, reaching once again a background-free regime [41].

Following the $^{214}$Bi $\gamma$-line study, the high voltage cables were replaced with lower activity cables in an upgrade of GERDA to minimise their background. The natural detector dataset produced in this work is the final dataset for these detectors, as the central string was subsequently lifted up in the course of the latest upgrade and the natural detectors were removed. In their place, five new

detectors of a brand-new detector type were introduced into the experiment. Their characterisation campaign follows in the next chapter.

# Chapter 4

# Characterisation and Active Mass of Inverted Coaxial Detectors

The demand for high mass detectors to reach the active mass goals for LEGEND-200 and later LEGEND-1t has inspired the characterisation of five new enriched germanium diodes of a new detector type called Inverted Coaxial (IC) [82, 83]. This chapter describes the attributes and specifications of these detectors and explains the characterisation campaign (Section 4.1), in particular the determination of their active mass through the comparison of relative $\gamma$-line intensities of MC simulations to radioactive source data (Section 4.2–4.4). After gathering as much information as possible from the natural detectors, as presented in the last chapter, the central string has been replaced by these new IC detectors in the course of an upgrade to the experiment. Following the successful results in the active mass determination, described in Section 4.4, the data gathered by the IC detectors are to be used directly in the precise exposure calculation for the $0\nu\beta\beta$ analysis, effectively adding more enriched mass to the experiment and proving their value for LEGEND.

## 4.1   IC Detector Characterisation Campaign

The $0\nu\beta\beta$ survival fraction of the latest BEGe dataset was estimated to be $(87.6 \pm 2.5)\%$, while the Coaxial one was $(71.2 \pm 4.3)\%$ [84]. The superior Pulse Shape Discrimination (PSD) performance of the BEGe type detectors, as a result of

their point contact readout electrode, lead in the search for new detector types for LEGEND to the consideration of the Inverted Coaxial (IC) detectors [82, 83]. These detectors, while also featuring a point contact readout electrode, are substantially bigger in dimension – from an average of 135 cm$^3$ for BEGes to 400 cm$^3$ for ICs. The bored detector well on the top enables optimatal PSD field lines in the fully depleted detector throughout the larger detector bulk, as shown in in the next Chapter in Figure 5.11 [82]. By reducing the surface to volume ratio, while increasing the detector mass in comparison to the number of cables, an even lower background index of the experiment can be achieved. This will help substantially in retaining a background-free regime for all of the exposure of LEGEND. Figure 4.1 shows the schematic of an IC detector.
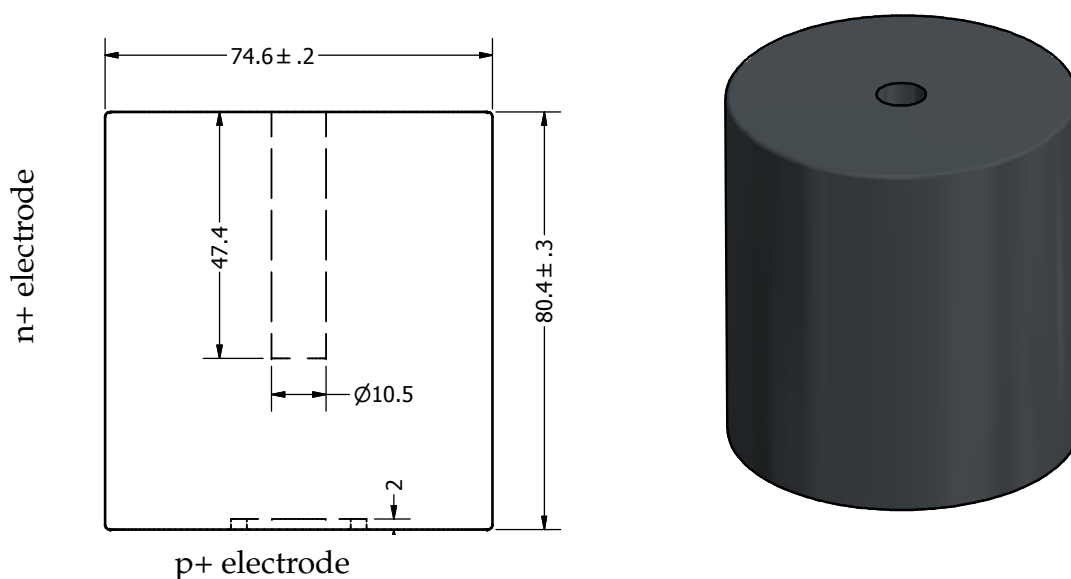


FIGURE 4.1: Inverted coaxial (IC) detector schematic for IC48A: Precise dimensions and uncertainties (left), and as an illustration (right). The dimensions are in mm. The schematics for all other IC detectors in GERDA can be found in Appendix A in Figure A.1.

In 2017, the company Mirion in Olen, Belgium, produced out of an initial 20 kg of enriched germanium five IC detector of about 1.9 kg each for the GERDA Collaboration : IC48A, IC48B, IC50A, IC50B, and IC74A. After transporting them to the nearby HADES Underground Research Laboratory at a depth of 225 m (500 m water equivalent) in Mol, Belgium, the detectors were tested inside a measurement set-up depicted in Figure 4.2.

The aim was to confirm their depletion voltages and the energy resolutions provided by the manufacturer, validate the expected PSD performances, and
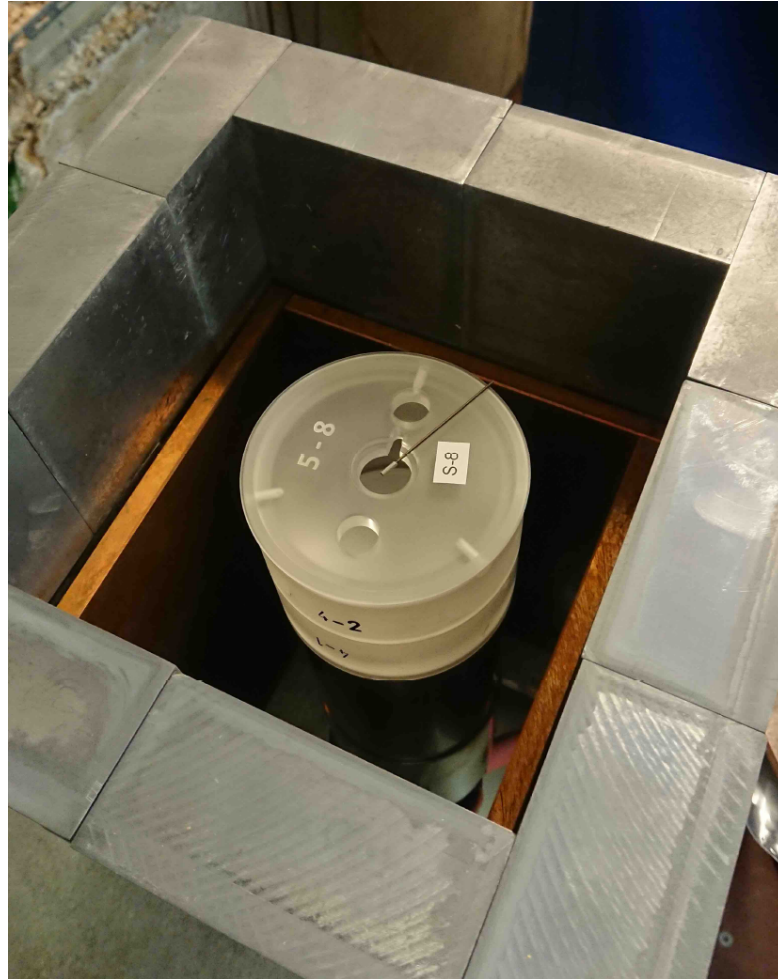
FIGURE 4.2: Measurement set-up at the HADES facility in Mol, Belgium. It consists of a lead castle surrounding a cryostat consisting of an aluminum cap and a copper holder which carries an IC detector cooled by a coldfinger from below. Here, the $^{228}$Th source is in a radially centered position 10 cm above the cryostat.

determine their active masses. As important parameters for the $0\nu\beta\beta$ analysis, the active masses had to be calculated from the estimated active volumina, in detail described in this work. While their outer geometry, and therefore raw mass, can be easily measured, there was a remaining uncertainty about the thickness of the outer n+ electrode, as shown in Figure 4.3. Energy deposits in this electrode volume, strongly doped with lithium thermal diffusion, are not detected, hence do not contribute to the active volume of the detector. Additionally, this barrier consists not only of a Dead Layer (DL) with no induced charge, but also of a Transition Layer (TL) in which a fraction of the charge is induced. Only in the inner volume beneath the Full Charge Collection Depth (FCCD) – the sum of the Dead Layer and the Transition Layer – is the full charge of an incident
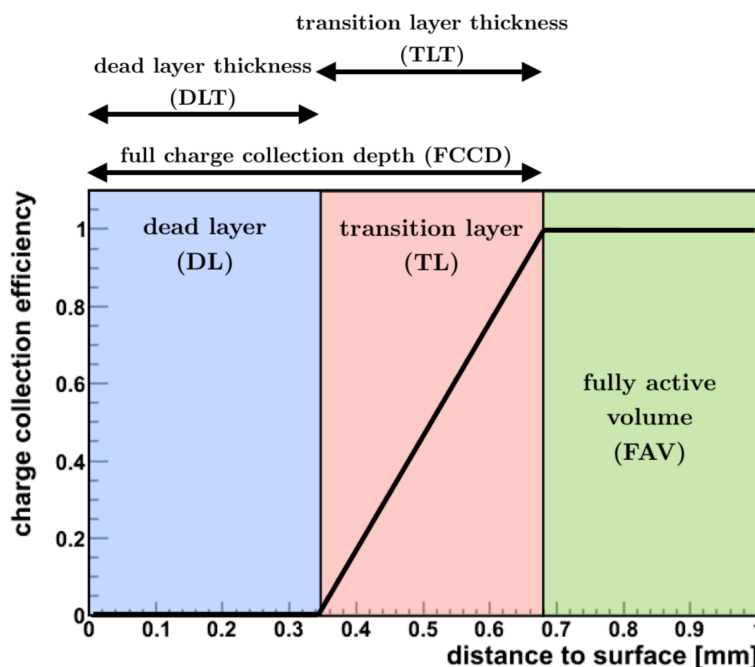
FIGURE 4.3: Layers of the n+ Electrode on the IC Detector Surface: Model split of the FCCD into Dead Layer with zero charge collection and Transition Layer with partial charge collection assumed to increase linearly with distance. Only the Active Volume, starting after the FCCD, features full charge collection. Figure from [85].

particle induced to properly determine its energy, thus comprising the active volume. The inner p+ electrode, on the other hand, is boron doped and thus negligible in thickness. The size of the n+ FCCD is about 1 mm and can be deduced from exposing the detector to radioactive sources and measuring either relative or absolute $\gamma$-line intensities – making use of the energy dependence of the $\gamma$-particle attenuation length.

For this purpose, measurements were performed using [228]Th and [241]Am sources with activities of 19 kBq and 4.3 MBq respectively. For the [228]Th top position measurements, the non-collimated source was chosen to be fixed in a radially centered static position 10 cm above the cryostat to minimise pile-up. This lead to a high geometrical acceptance, but to a still relatively large dead time of $(17.5 \pm 0.5)\%$ for all detectors and measurements. Section 4.3.1 describes the analysis using [228]Th to retrieve the active mass. A scanning table was used to position the [241]Am source, which allowed for the pinpointing of the $\gamma$-emissions onto the detector surfaces through the 1 mm hole of the 30 mm thick collimator. In order to estimate the active mass of the detectors using the [241]Am source, special High Statistics measurements were performed, wherein the sources were
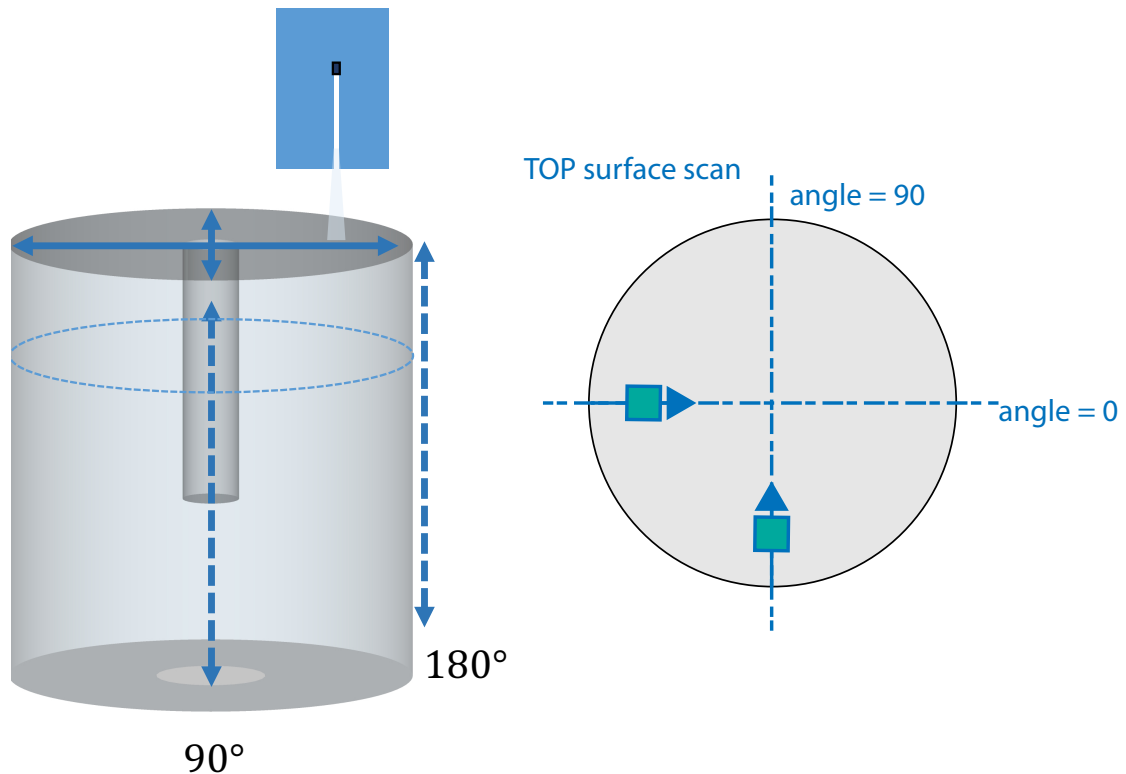
FIGURE 4.4: Schematic of the $^{241}$Am scan set-up at HADES with a side view (left) and a top view (right): Each IC detector was iteratively scanned by collecting data for 300 s at each of the 84 points along angles 0° and 90° with the $^{241}$Am source at constant height.

positioned around 15 mm above the detector for 5 h. Due to complications at measurement time, the high statistics measurements were taken only for IC48B and IC50B. However, all the detectors were iteratively scanned over in two perpendicular angles for 300 s at each of the 84 points, as shown in Figure 4.4. These scan measurements were subsequently summed and used to estimate the active mass, as described in Section 4.3.2, for the three other IC detectors: IC48B, IC50A, and IC74A.

## 4.2 IC Detector MC Simulations

Following the source measurements, the goal was to compare the relative $\gamma$-line intensities in the data to the ones in MC simulations of increasing simulated FCCDs to determine their real size. First, the measurement set-up was modelled

in MaGe, based on GEANT4, with detailed specifications of the detector and set-up dimensions as shown in the schematics in Figure 4.1 and Figure 4.5.
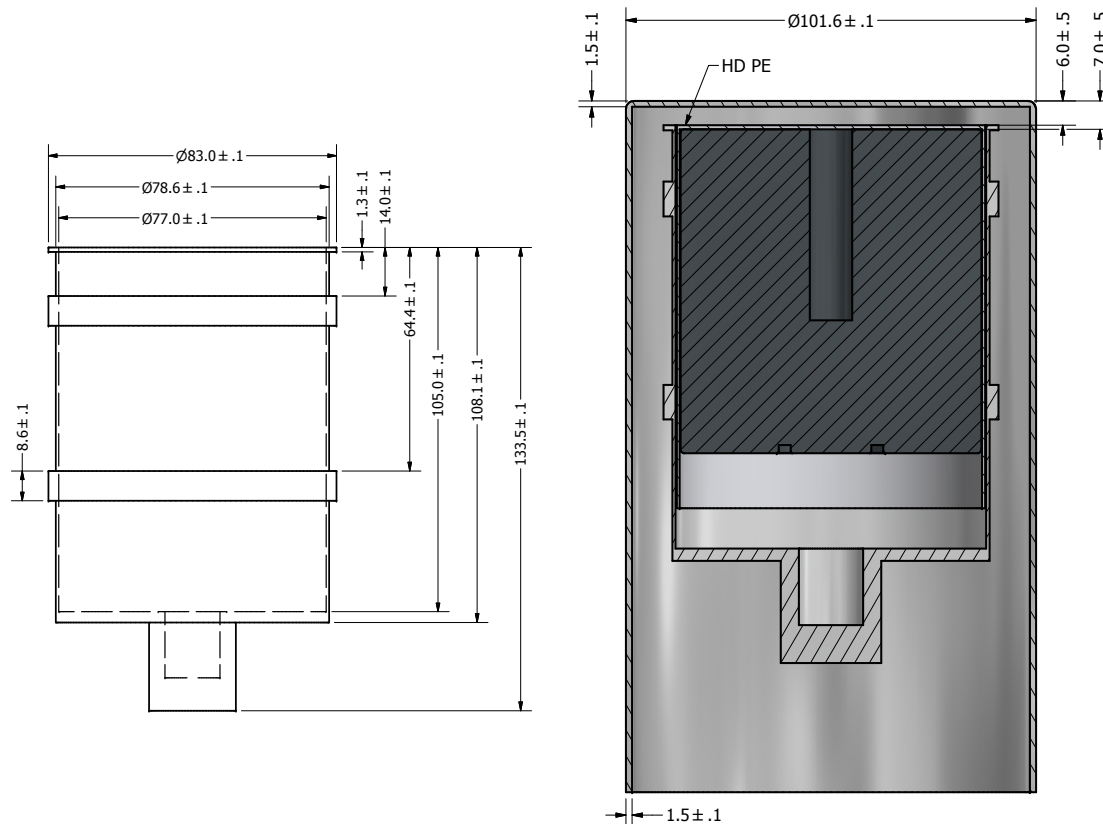


FIGURE 4.5: Schematic of the measurement set-up to test the Inverted coaxial (IC) detectors at HADES: Detailed specifications of the detector holder (left) and the whole cryostat including aluminum cap, copper holder, and detector (right) that were implemented into MaGe using Geant4 for the MC simulations. The dimensions are in mm.

The aluminum cap of 101.6 mm diameter and 170.8 mm height surrounds the detector set-up, wherein the germanium crystal is held in place by a 83.0 mm diameter and 133.5 mm height copper holder screwed directly into the cap. The germanium diodes, due to the nature of the crystal pulling process during production, vary slightly in their dimensions, ranging from 72.2 mm to 76.6 mm diameter and 80.4 mm to 85.4 mm height. The 10.5 mm radius bored holes and 26 mm diameter grooves, worked into the crystals afterwards, are known to below 0.1 mm precision. All IC detector geometries for IC48A, IC48B, IC50A, IC50B, and IC74A were implemented with their exact geometric parameters known to $\pm 0.2 - 0.3$ mm. Figure 4.6 shows the resulting complete model implemented into MaGe rendered as a wireframe visualisation using VRML driver 2.0.
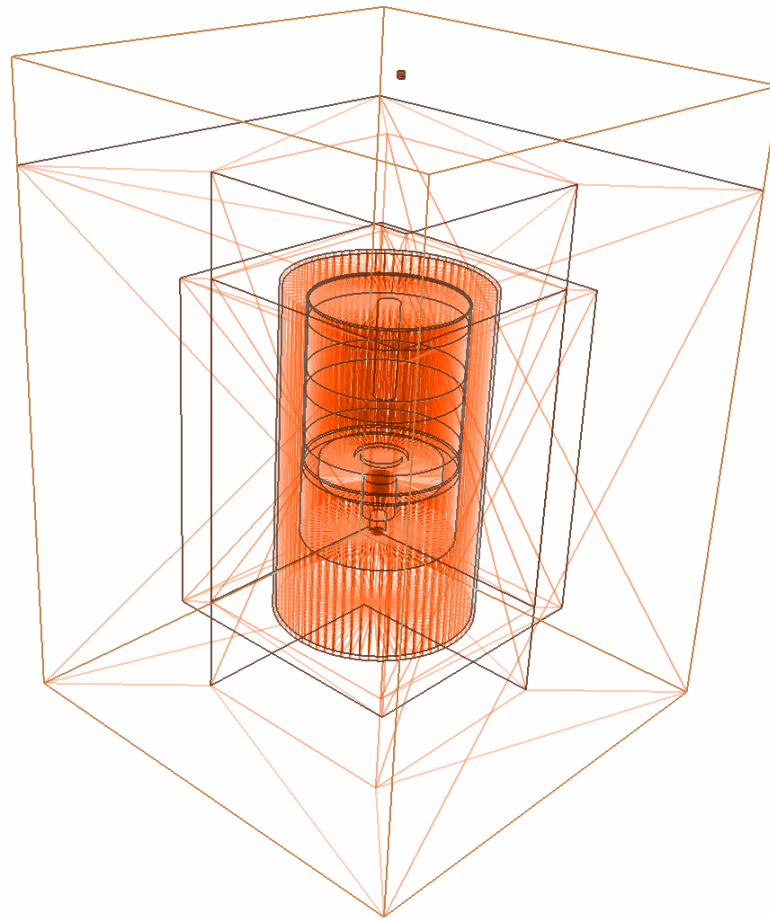
FIGURE 4.6: MaGe simulation visualisation of the $^{228}$Th measurement set-up zoomed into the central part. At its heart is the IC48 detector with its prominent detector well, placed into the copper holder and cryostat. Outer layers such as lead castle are either transparent or removed in the visualisation to display the core.

In order to simulate energy spectra of $^{228}$Th, the primary high energy daughter decay modes $^{208}$Tl and $^{212}$Bi were simulated to $10^9$ events each. In order to determine the correct FCCD for each detector by matching the data with simulations, they need to reflect different Dead Layer sizes. Due to the high amount of simulation time required to resimulate each detector with increasing Dead Layers, a more efficient approach was chosen: Each simulation of each detector was run with just a 0 mm Dead Layer for each component, saving the positions of energy deposits inside the detector. In the post-processing of the output, however, the saved energy deposits in the germanium crystal – so-called

hits – were incrementally cut depending on their position in the shape of the Dead Layer. This geometric fiducialisation helped produce simulations with Dead Layers ranging between 0 mm to 2 mm in 0.2 mm steps. For simplicity, any hit in the FCCD was assumed to induce no charge, making the FCCD an effective Dead Layer without a Transition Layer for the $^{228}$Th simulations.



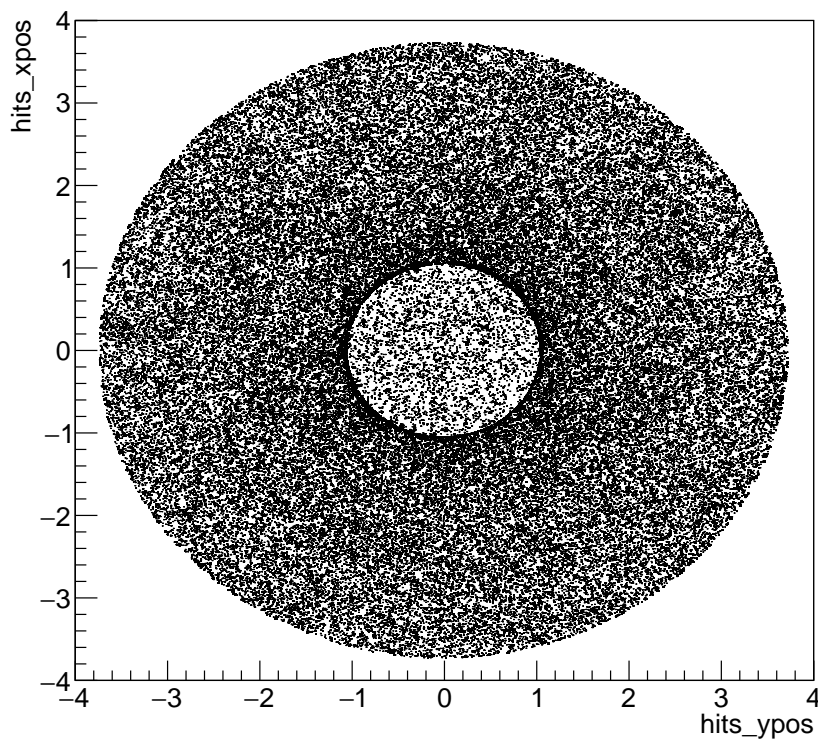FIGURE 4.7: Simulated hits in IC48A coming from a $^{208}$Tl in top position and viewed from the top into the xy-plane. The IC detector well position is visible in the center.

The deposited energies of the remaining hits are then smeared with a Gaussian function to model the detector response. The width of the Gaussian was obtained by fitting to 12 known peaks in the $^{228}$Th spectrum. The resulting energy resolution curve allowed for the interpolation of the width using the parametrisation

$$\sigma = \sqrt{a + bE} \, , \tag{4.1}$$

with energy E and fit parameters a, b. The fitting function was a combination of a Gaussian function (as the peak itself), a low energy tail accounting for phenomena such as ballistic deficits or incomplete charge collection, a constant and linear background, as well as a step function describing the background amplitude and possible difference between each side of the peak. The fitting
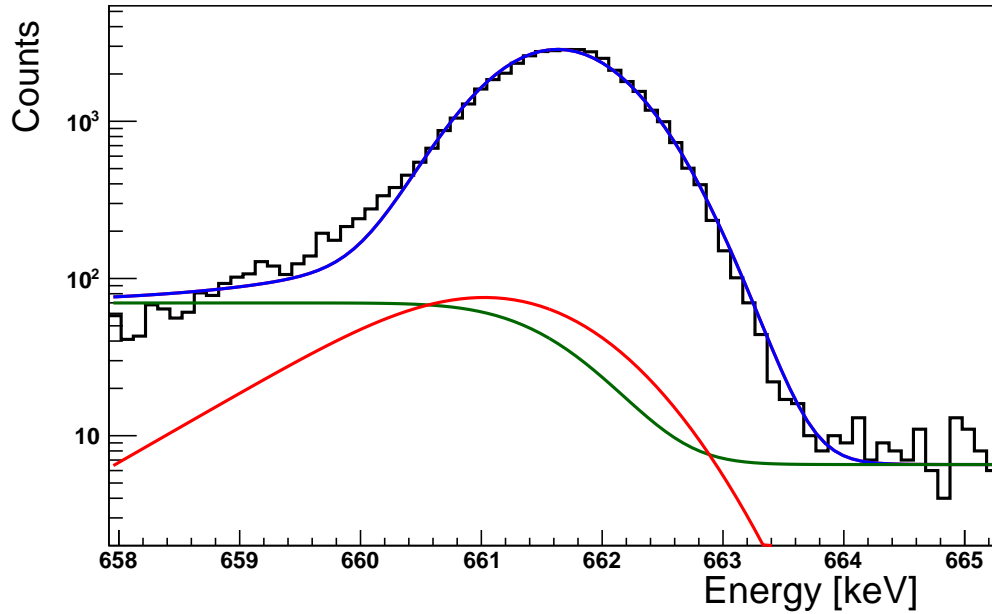
FIGURE 4.8: Example fit onto the energy histogram (black) using a Gaussian function , a linear, constant, and step function background (green), and a low energy tail (red), resulting in the the full fit function (blue). Fitting all major peaks in the data spectrum creates a resolution curve that can be used to smear the simulated spectra to imitate the detector response.

function is defined in Equation 4.2.

$$
\begin{aligned}
f(x)_{Fit} = &\frac{A_{Gauss}}{\sqrt{2\pi}\sigma}\exp\left(\frac{-(x-\mu_0)^2}{2\sigma^2}\right) \\
&+ \frac{B_{Tail}}{2C}\exp\left(\frac{x-\mu_0}{C} + \frac{D^2}{2C^2}\right) \cdot \mathrm{erfc}\left(\frac{x-\mu_0}{\sqrt{2}D} + \frac{D}{\sqrt{2}C}\right) \\
&+ \frac{E_{Step}}{2}\mathrm{erfc}\left(\frac{x-\mu_0}{\sqrt{2}\sigma}\right) \\
&+ F_{Linear} \cdot (x-\mu_0) + G_{Constant} ,
\end{aligned}
\tag{4.2}
$$

with $\mu_0$ as the mean and $\sigma$ as the standard deviation of the Gaussian function, and $A_{Gauss}, B_{Tail}$, C, D, $E_{Step}$, $F_{Linear}$, and $G_{Constant}$ as free fit parameters. Figure 4.8 shows an example of such a fit. The energy resolution curve used for the smearing, was extracted from the FWHM of the Gaussian component, calculated from the fit parameter $\sigma$, as given by
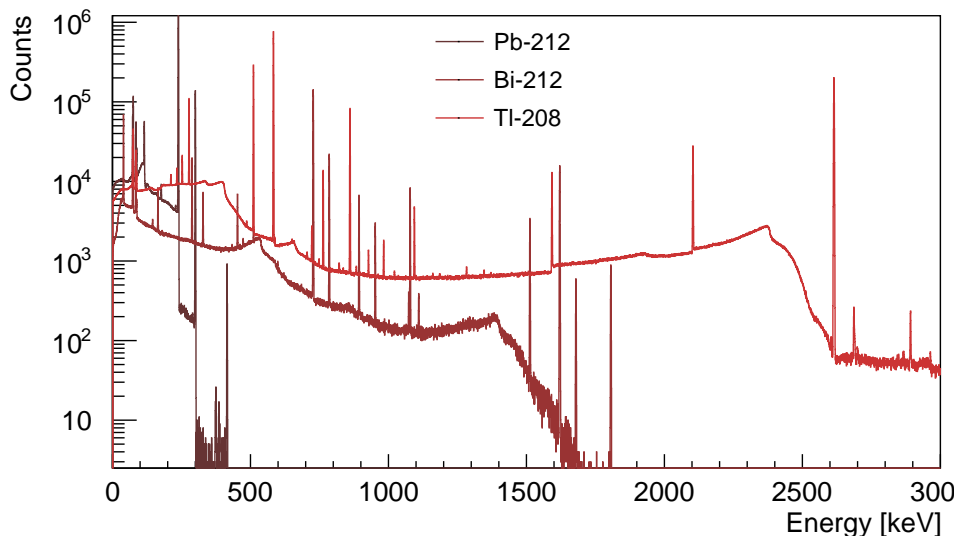
$$
\mathrm{FWHM} = 2\sigma\sqrt{2\ln2} .
\tag{4.3}
$$

FIGURE 4.9: Energy spectra of $^{208}$Tl and $^{212}$Bi as main components can be summed to create $^{228}$Th above 500 keV. The component $^{212}$Pb was initially not included as its highest $\gamma$-peak is located at 415 keV, but later on helped in matching the low energy region below 500 keV.

The event energies were then adjusted according to

$$E = E + \Delta E \,, \tag{4.4}$$

where E is the initial event energy, $\Delta E$ a number created by a random number generator constrained by the composition of a Gaussian function, centered around the origin with the FWHM from the resolution curve, and a low energy tail component with its parameters defined by the 2.6 MeV line low energy tail parameters extracted from data. As a result, the simulations featured peak widths and low energy tails, resembling the detector response and pile-up in the data.

The resulting energy histograms of $^{208}$Tl, $^{212}$Bi, and $^{212}$Pb were then weighted and combined, as shown in Figure 4.9, according to their known branching ratios, including transient equilibrium corrections, signifying the fraction of particles decaying in each mode relative to the total number of decaying particles [63].

The simulated energy spectra for various Dead Layers and thus FCCDs were directly compared to the measured data to judge their accuracy, as depicted in Figure 4.11. While the peaks and the Compton edge matched well, an inconsistency appeared in the continuum slope. The difference in the low energy tail at the 2.6 MeV line originated from a visible ballistic deficit in the data, due

to pile-up from high dead time during the measurements, not included in the smearing function and, thus, not replicated in these initial MC simulations.
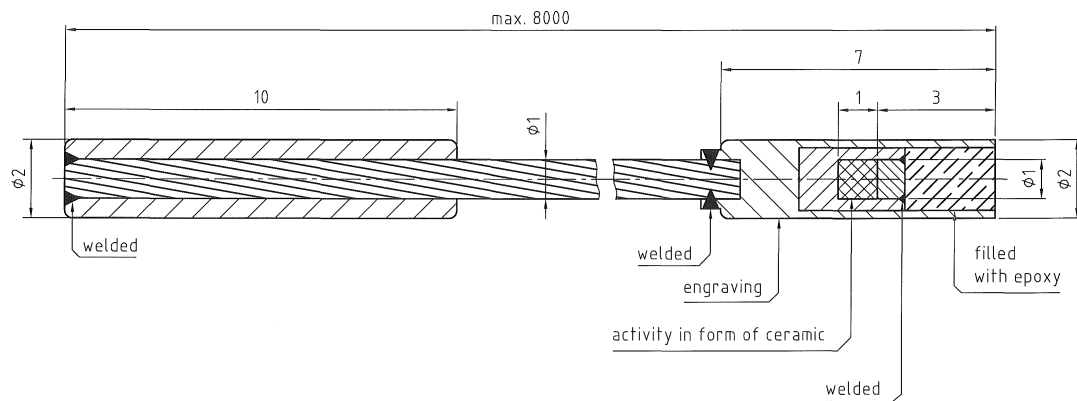


FIGURE 4.10: Schematic of the [228]Th source container, made of stainless steel, used for the IC detector measurements. The dimensions are in mm.

To solve these issues, the MC simulations and the treatment of the data underwent several improvements. Firstly, as there had been a significant pile-up rate at measurement time, more stringent quality cuts were chosen to clean up the data. Secondly, on the simulation side, the addition of [212]Pb, as an additional component of [228]Th, helped to diminish the discrepancy in the low energy range. Next, moving away from just describing a point-source, the source container and the source dimensions were precisely modelled to the specifications of the Eckert & Ziegler VZ-3258 encapsulation, as depicted in Figure 4.10. Most importantly, the surrounding lead castle, visible in Figure 4.2, was implemented into the simulation framework and fully modelled. The back-scattering off of the lead bricks decisively affected the Compton continuum slope to reflect the one of the data. No significant Transition Layer effects were observed for [228]Th that necessitated the creation of such a layer in the simulated FCCD in addition to the Dead Layer. Finally, performing the smearing with a Gaussian function and the low energy tail extracted from the 2.6 MeV line lead to a good agreement between the MC simulations and the data, as shown in Figure 4.12.
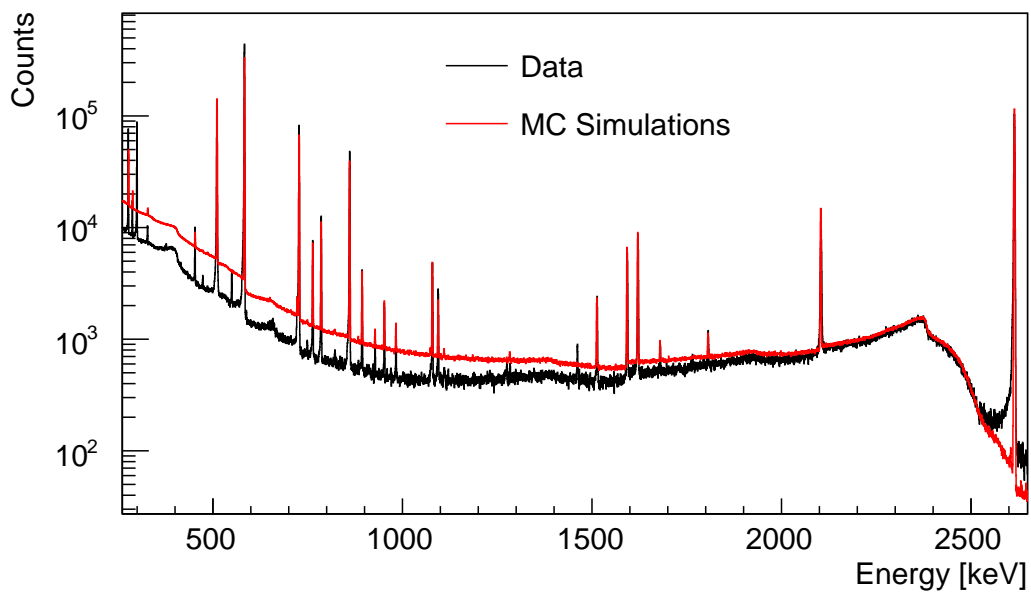
FIGURE 4.11: Initial MC simulations of $^{228}$Th (for IC48A as an example) that exhibited problems in matching the continuum slope and the low energy tail of the 2.6 MeV line. These issues were solved in Figure 4.12 by implementing $^{212}$Pb as another component, modelling the source container and the surrounding lead castle, as well as introducing a low energy tail into the smearing function.
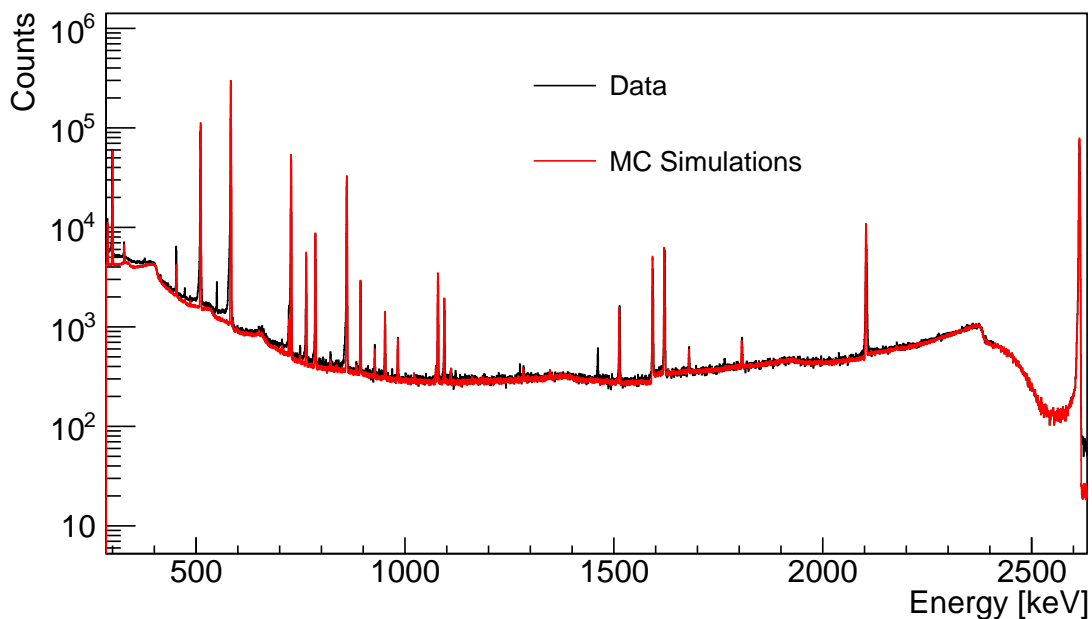


FIGURE 4.12: Optimised $^{228}$Th MC (for IC48A as an example) after introducing several improvements to the realism of the simulation. The simulated components are $^{212}$Bi, $^{208}$Tl, and $^{212}$Pb. There is a good agreement in the whole range, including the low energy tail of the 2.6 MeV line.

## 4.3 Full Charge Collection Depth Determination

The analysis was based on the assumption that the FCCD is homogeneously distributed across the entire detector surface. The active volume equals the full crystal bulk minus the surrounding volume, generated by the constant FCCD. This enables the employment of surface sensitive, low energy $\gamma$-ray sources such as $^{241}$Am to determine the FCCD. High energy sources such as $^{228}$Th are more bulk sensitive and as such probe the active volume directly, but should also allow for an estimation on the FCCD since the active volume is constraint by it. Since the measurements with the IC detectors had been performed for $^{228}$Th and $^{241}$Am, the FCCDs were determined for both source types. The $^{241}$Am FCCD determination, described in detail in Section 4.3.1, is a tried-and-tested approach, since it is ideally suited to probe close-to-surface effects with its low energy emissions. The $^{228}$Th FCCD determination in Section 4.3.1 was a novel analysis avenue, using much higher energy $\gamma$-peaks than in previous characterisation campaigns, thus allowing for the direct probing of the FCCD in the $Q_{\beta\beta}$ region at 2039 keV.

### 4.3.1 Full Charge Collection Depth $^{228}$Th Results

In order to determine the FCCD of each detector, the relative $\gamma$-line intensities in the $^{228}$Th measurement data were matched to MC simulations of different Dead Layers. For this purpose, 9 different $\gamma$-lines were chosen due to their height and prominence to other peaks and background: 2104 keV, 1593 keV, 1513 keV, 1094 keV, 952 keV, 861 keV, 786 keV, 583 keV, and 511 keV. They were fitted with a combination of a Gaussian function, a constant and linear background, a step function, and a low energy tail, as stated in Equation 4.2 as $f(x)_{Fit}$. The extracted fit parameters of function $f(x)_{Fit}$ are inserted into $g(x)_{Signal}$, defined in Equation 4.5, to subtract the full background and determine the count rate.

$$
\begin{aligned}
g(x)_{Signal} \; = & \frac{A_{Gauss}}{\sqrt{2\pi}\sigma} \exp\left(\frac{-(x-\mu_0)^2}{2\sigma^2}\right) \\
& + \frac{B_{Tail}}{2C} \exp\left(\frac{x-\mu_0}{C} + \frac{D^2}{2C^2}\right) \cdot \mathrm{erfc}\left(\frac{x-\mu_0}{\sqrt{2}D} + \frac{D}{\sqrt{2}C}\right).
\end{aligned}
\tag{4.5}
$$

with $\mu_0$ as the mean and $\sigma$ as the standard deviation of the Gaussian function and $A_{Gauss}, B_{Tail}, C$, and $D$ as free fit parameters. The low energy tail component

of g(x)$_{Signal}$ then includes signal events stemming from high dead time induced pile-up events that are underestimated in energy, but are still de facto originating from full charge collections.

The signal ratio in relation to the extracted signal of the fitted 2615 keV line was then calculated for all measurements and all MC simulations, according to Equation 4.6.

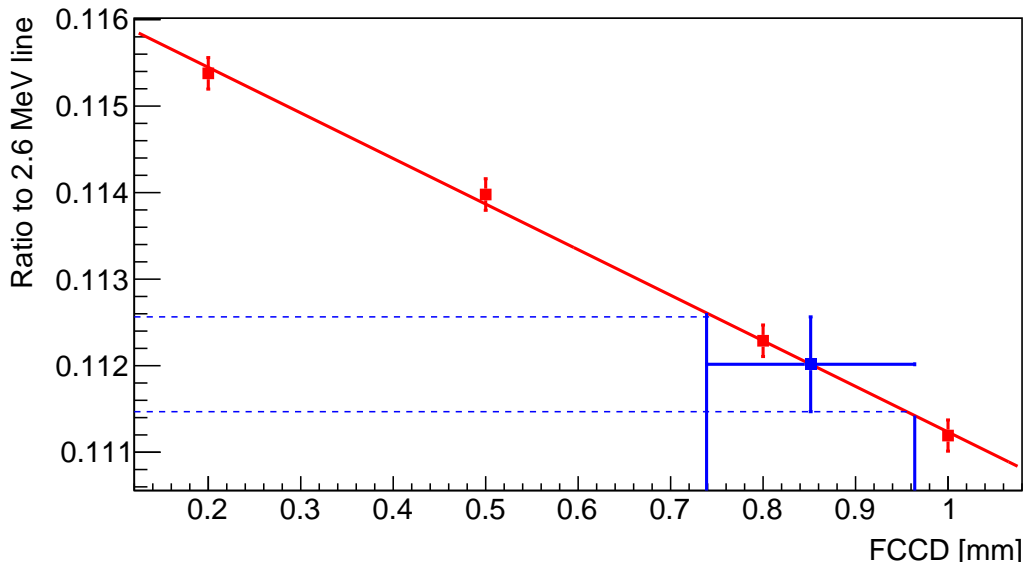$$R_{i\,keV}^{228\mathrm{Th}} = \frac{\epsilon_{i\,keV}}{\epsilon_{2615\,keV}} \quad . \tag{4.6}$$



FIGURE 4.13: Peak ratio graph for $^{228}$Th (for IC48A as an example): Extracted MC simulated peak ratios (red) at 2104 keV against the simulated Dead Layers and thus FCCDs. The data peak ratio (blue) was then interpolated to the fitted linear curve with the blue data point representing the best fit and the error bars on the y-axis consisting of the uncertainty on the peak fit. The error bars on the x-axis reflect the resulting uncertainty on the determined FCCD.

The calculated ratios of the MC simulations for different Dead Layers and thus FCCDs were then plotted for each peak independently, as shown in Figure 4.13 for IC48A. The error bars on the ratios stem from the uncertainties on the 8 fit parameters of the 4 fit components and were estimated by varying each fit parameter according to an individual Gaussian function. The mean of the Gaussian is located on the best fit value and the FWHM determined by the uncertainty on the parameter. The resulting solution space of all possible ratios was histogramised and its standard deviation represents the uncertainty on the ratio. The MC simulations exhibit lower uncertainties on their peak fits than the fits of the data. The ratio points from the MC simulations were fitted with a linear regression, exhibiting lower signal strength for increased FCCD.
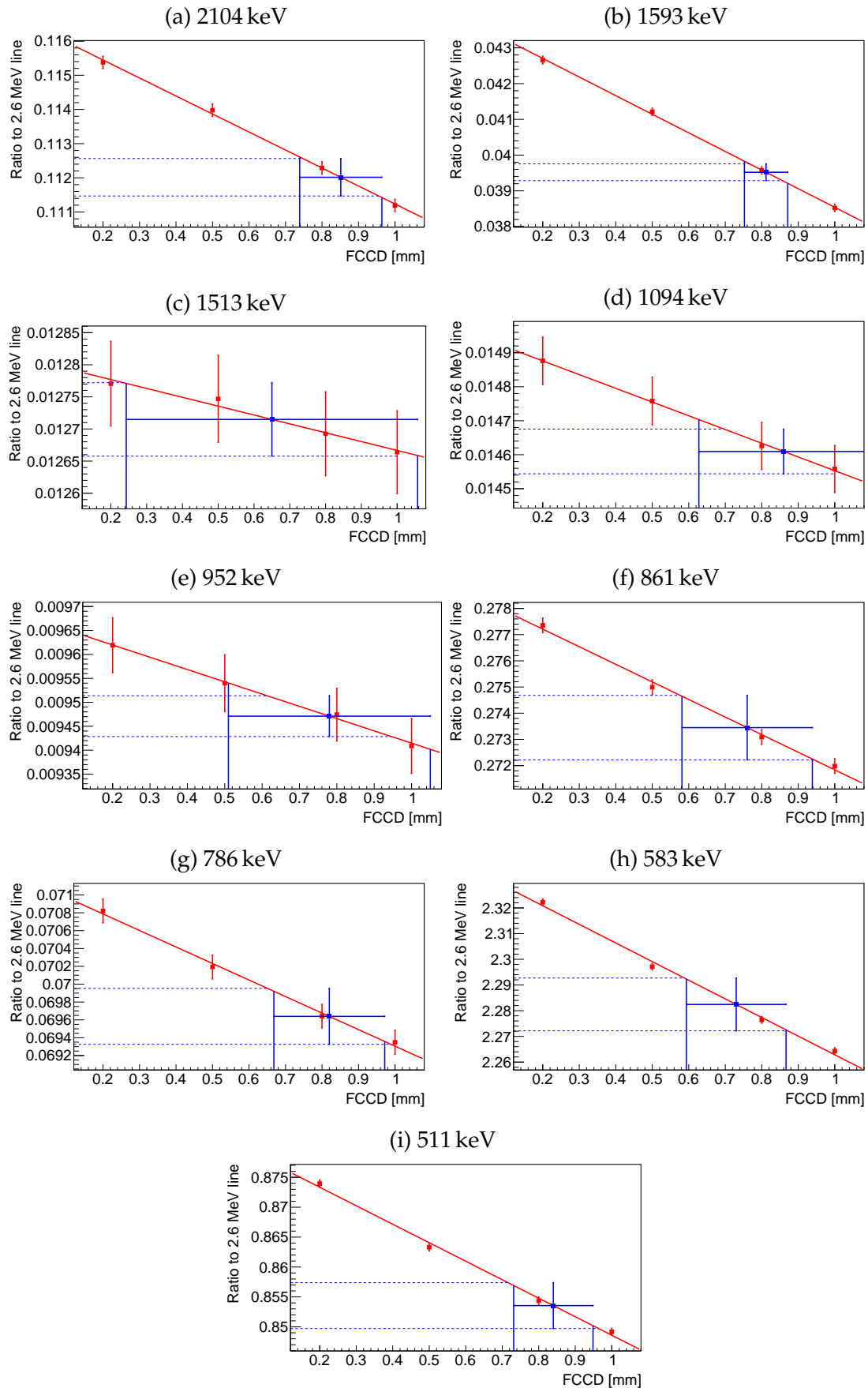
FIGURE 4.14: All IC48A $^{228}$Th peak ratio graphs (for IC48A as an example): Extracted MC simulated peak ratios (red) against the simulated FCCDs for the indicated energies. The data peak ratios (blue) were then interpolated to the fitted linear curves with the blue data points representing the best fit value and the error bars on the y-axis consisting of the uncertainties on the peak fits. The error bars on the x-axis reflect the uncertainties on the determined FCCDs.

The FCCD, corresponding best to the data, was determined from this linear regression by interpolating to the peak ratio obtained from data, leading to a best fit value on the FCCD and a statistical uncertainty on the result. This uncertainty is reflected in the error bar of the FCCD and was calculated by the Gaussian variation of the linear fit parameter uncertainties. Simultaneously, the data peak ratio was varied using a Gaussian function with its mean located on the best peak fit and the uncertainty on the peak fit ratio as the FWHM. At each step, the varied data peak fit ratio was interpolated onto the varied curve and the result is added to a histogram, whose standard deviation then represents the statistical uncertainty on the FCCD best fit value for that energy. For better visualisation, all 9 energy peak graphs of IC48A are shown in Figure 4.14.

To study the energy dependence of the FCCDs, the estimated FCCDs were visualised against energy in Figure 4.15 and fitted with a linear function. For IC48A, IC48B, and IC50B, there is no slope, whereas both IC50A and IC74A exhibit a downwards trend for effective FCCD towards higher energies. This could be due to the energy dependence of the electron-hole cloud sizes becoming more prominent in conjunction with a geometric solid angle effect for larger FCCDs.

The effective FCCD was determined by the evaluation of the best fit linear function of the FCCD over the full energy range at $Q_{\beta\beta}$, the region of interest for the $0\nu\beta\beta$ analysis of GERDA. The analysis was performed for all 5 IC detectors. The resulting FCCDs from the $^{228}$Th based analysis are collected in Table 4.1.

| Detector | FCCD at $Q_{\beta\beta}$ |
|---|---|
| IC48A | 0.81 mm $\pm$ 0.08 mm (stat.) |
| IC48B | 0.78 mm $\pm$ 0.09 mm (stat.) |
| IC50A | 0.86 mm $\pm$ 0.12 mm (stat.) |
| IC50B | 0.76 mm $\pm$ 0.09 mm (stat.) |
| IC74A | 0.88 mm $\pm$ 0.13 mm (stat.) |

TABLE 4.1: FCCD results at $Q_{\beta\beta}$ for each IC detector from peak ratio comparison to $^{228}$Th measurements. The systematic uncertainties are described in Section 4.3.3.
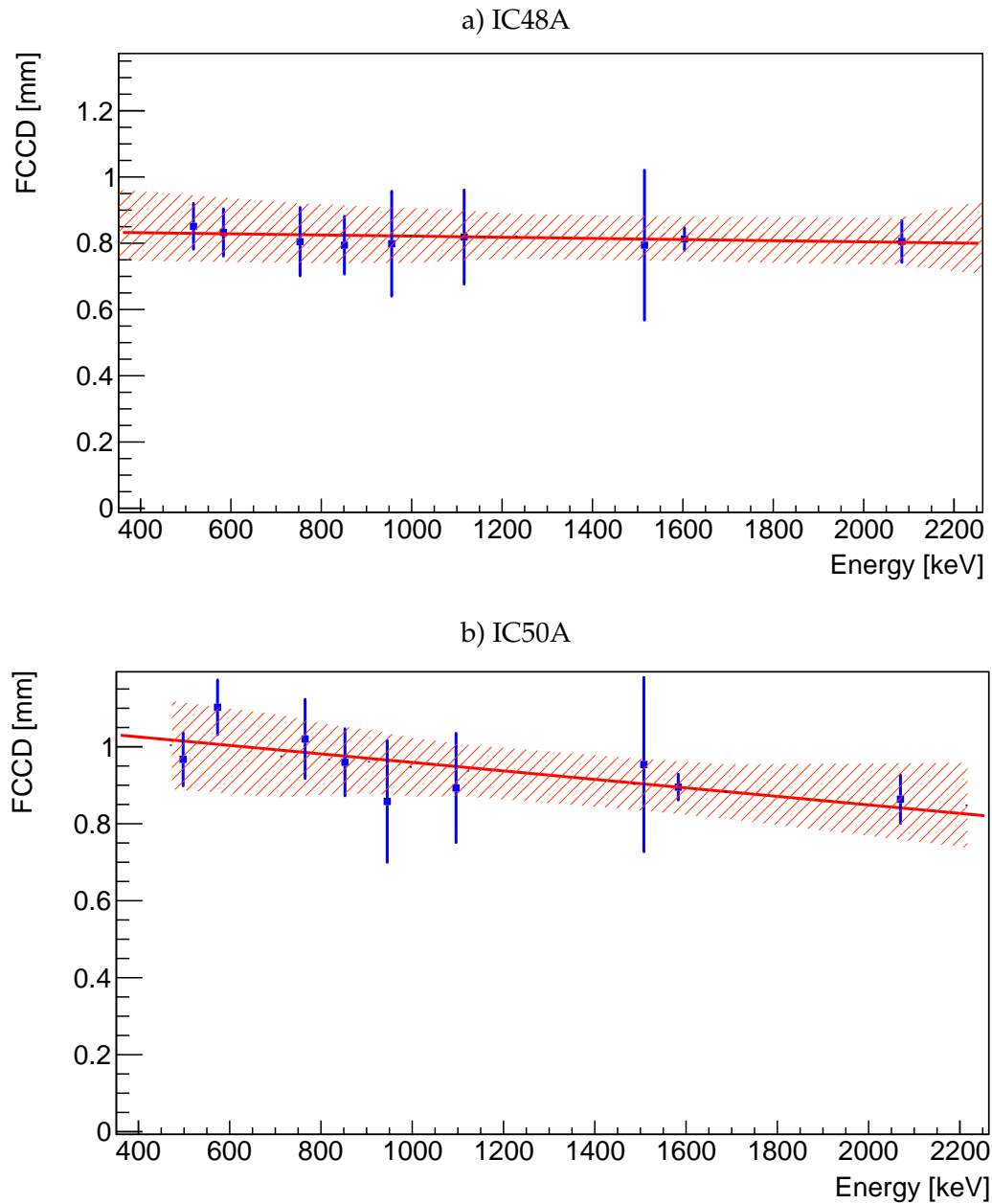
FIGURE 4.15: Energy dependence of $^{228}$Th peak ratios for IC48A (top, a) and IC50A (bottom, b): Plotting of the estimated FCCDs against the peak energies (blue): 2104 keV, 1593 keV, 1513 keV, 1094 keV, 952 keV, 861 keV, 786 keV, 583 keV, and 511 keV. The linear fit (red) through the points evaluated at $Q_{\beta\beta}$ leads to the estimate of the FCCD, e.g. $(0.81 \pm 0.08)$ mm for IC48A.

## 4.3.2   Full Charge Collection Depth $^{241}$Am Results

The measurements with the $^{241}$Am source were analysed next. In a previous characterisation campaign for the BEGe type detectors, the results from $^{241}$Am were used for the active mass, since the source features only low energy peaks, where the influence of the FCCD should be especially pronounced. The high statistics measurements, described in Section 4.1, available for IC48B and IC50B were used first to estimate the FCCD of the IC detectors.

On the simulation side, the IC detector version of MaGe was employed, as described in Section 4.2. The procedure was similar to the characterisation campaign of the BEGe [86, 87]. The $\gamma$-lines produced by the decay of $^{241}$Am were directly simulated with the correct relative intensities, including the energy peaks of 59.5 keV, 99 keV, 103 keV, 65 keV, 67.5 keV, 70 keV, 32 keV, 43 keV, 55.5 keV, 57.85 keV, and 125 keV. This allowed for a simulation to very high statistics of $10^{10}$ events. For the BEGe characterisation, $\gamma$-lines were directly simulated with the same procedure. Energy resolution smearing and geometrical fiducialisation to create FCCD simulations were performed analogously to Section 4.2.

The resulting spectrum is depicted in Figure 4.16 and features full energy peaks without the complex background seen in the data. The energy spectrum generated by the $^{241}$Am source features three prominent low energy peaks ideally suited for the FCCD extraction: The largest peak of the spectrum at 59.5 keV, and two close peaks with similar heights at 99 keV and 103 keV. These three peaks were fitted with a combination of a Gaussian function, a low energy tail, a constant and linear background, as well as a step function to subtract the full background and extract the count rate. The fitting function $f(x)_{Fit}$ is described in Equation 4.2. Inserting the extracted fit parameters of function $f(x)_{Fit}$ into $h(x)_{Signal}$, defined in Equation 4.7, yields the count rate by subtracting the full background from the peak.

$$h(x)_{Signal} = \frac{A_{Gauss}}{\sqrt{2\pi}\sigma}\exp\left(\frac{-(x-\mu_0)^2}{2\sigma^2}\right) \tag{4.7}$$

with $\mu_0$ as the mean and $\sigma$ as the standard deviation of the Gaussian function and $A_{Gauss}$ as a free parameter of the fit. The fitting procedure effectively removed the background at the peaks for simulation and data. Since there was only minimal dead time at measurement time, the few pile-ups were efficiently removed by
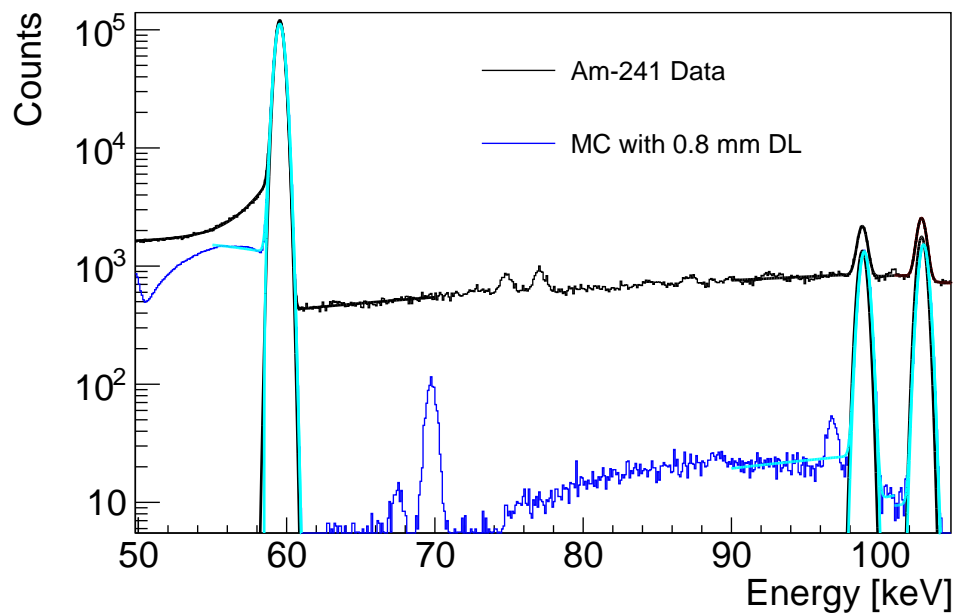
FIGURE 4.16: High statistics $^{241}$Am spectrum for IC48B: The simulated $\gamma$-lines result in a spectrum (blue) shown in comparison to the data (black) that includes non-simulated background. The fits to the 59.5 keV, 99 keV, and 103 keV are shown with a bold line (cyan) and black respectively). The peak ratio of these lines were used, according to Equation 4.12, to estimate the FCCD of the detector.
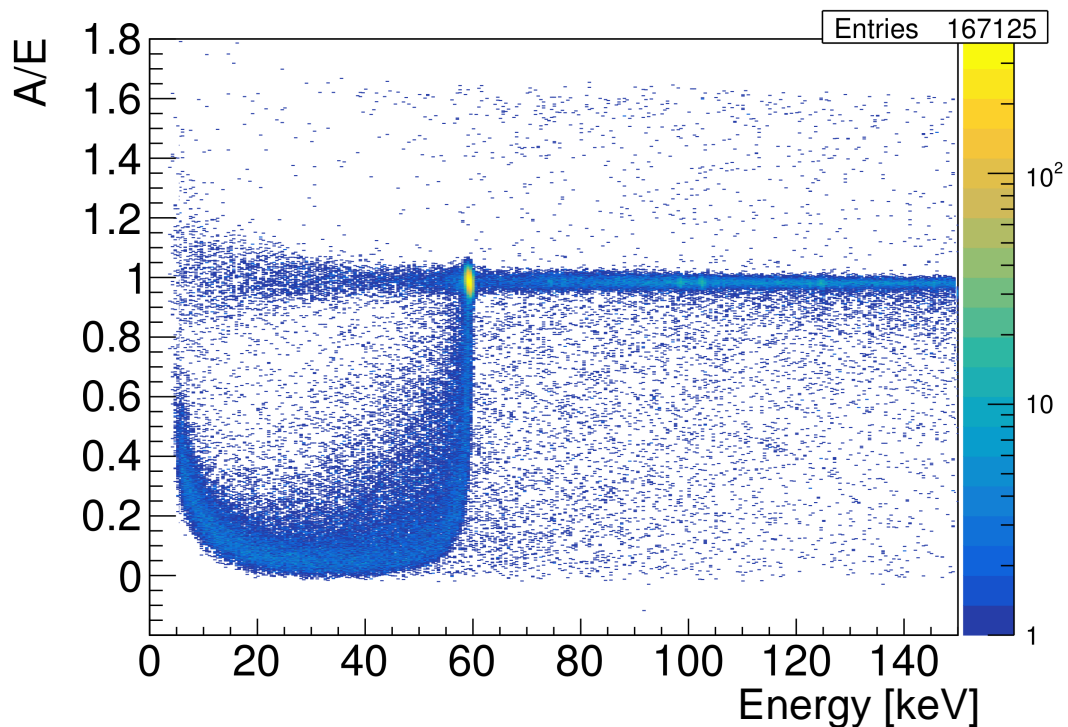


FIGURE 4.17: A/E distribution of $^{241}$Am spectrum: Many events below 59.5 keV feature a very low A/E parameter, which is characteristic of slow pulses, typically Transition Layer events. This is the explanation for the low energy tail of the 59.5 keV line in Figure 4.16.

the quality cuts. Any low energy tails in data were thus assumed to be of partial charge collection origin. The low energy tail visible below the 59.5 keV line stems most probably from the photoelectron released by the $\gamma$-ray losing some of its reconstructed energy due to the Transition Layer, which is not reproduced in the MC simulation. The A/E spectrum with respect to energy, shown in Figure 4.17, reveals that a substantial amount of events below the peak are slow pulses, long rise time events that underwent the slow diffusion process into the active volume to be registered, evidenced by a $A/E < 1$ parameter, typical for Transition Layer events. In order to replicate the Transition Layer effect in the $^{241}$Am simulation, a linear function was introduced in the geometrical fiducialisation stage to simulate a Transition Layer leading into the active volume, following an appropriately reduced Dead Layer on the outside. The hits would start contributing deposited energy linearly with the proximity to the active volume. The FCCD was thus separated into a Dead Layer and a Transition Layer part. The initial Transition Layer Thickness (TLT) was chosen to follow the Equation 4.8 with the experimentally inferred Dead Layer Fraction (DLF) of BEGes with similar FCCDs from [85].

$$TLT = FCCD \cdot (1 - DLF) \,. \tag{4.8}$$

The addition of a TLT reduces the Dead Layer Thickness (DLT), as the FCCD is the sum of the TLT and the DLT, according to

$$FCCD = DLT + TLT \,. \tag{4.9}$$

The TLT was then varied in 0.1 mm steps around that value and the best curve agreement to data was estimated from the minimal quadratic difference of the affected bins. The TLT best fit value followed Equation 4.8 up until an FCCD of 0.8 mm, where it remained constant for higher FCCD values on
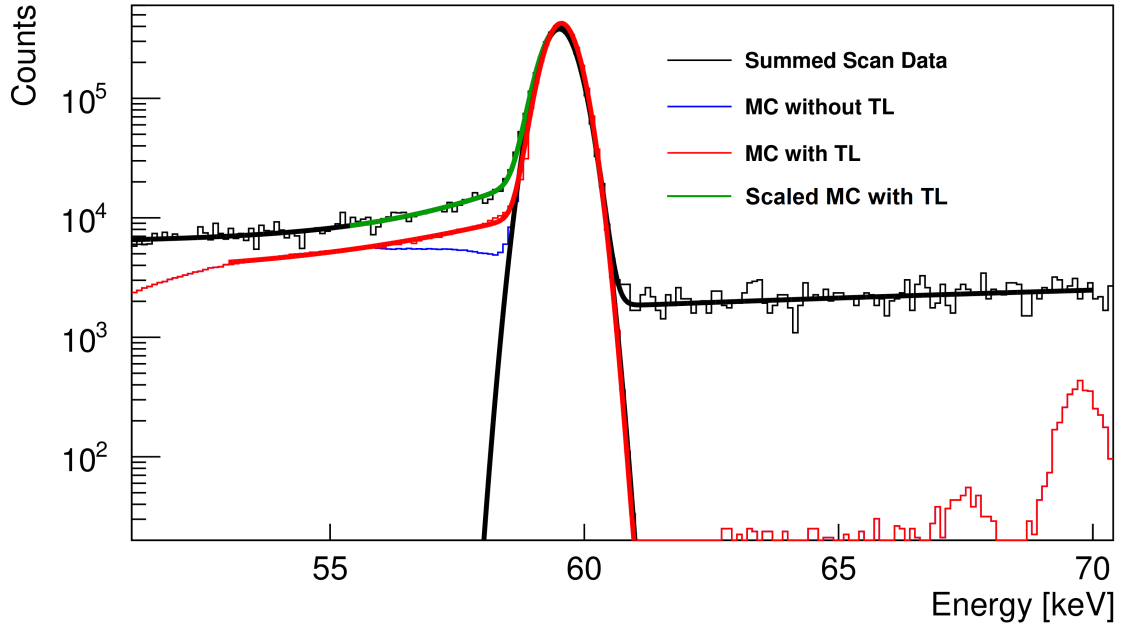
$$TLT = 0.6 \, \text{mm} \,. \tag{4.10}$$

FIGURE 4.18: Simulation of the Transition Layer effect for the $^{241}Am$ Spectrum: Below the 59.5 keV line, the simulations with a Transition Layer (red) created by introducing a layer of size 0.6 mm, wherein the deposited energy of hits is linearly increasing, lead to a much better agreement with data (black) than the simulations without Transition Layer (blue). Adding an additional background component to simulations with a Transition Layer leads to an overlapping low energy tail (darkgreen) The fits results are shown in bold.

As example cases, the chosen simulation sizes

$$0.2 \text{ mm FCCD} = 0.05 \text{ mm DL} + 0.15 \text{ mm TL}$$

$$0.5 \text{ mm FCCD} = 0.125 \text{ mm DL} + 0.375 \text{ mm TL}$$

$$0.8 \text{ mm FCCD} = 0.2 \text{ mm DL} + 0.6 \text{ mm TL}$$

$$1 \text{ mm FCCD} = 0.4 \text{ mm DL} + 0.6 \text{ mm TL,}$$

(4.11)

where DL is the Dead Layer and TL the Transition Layer, that together comprise the FCCD, would yield the best fit. Introducing a Transition Layer into the simulations results in a visibly better replication of the data, as seen in Figure 4.18, and a lower uncertainty on the fits.

To retrieve the size of the FCCD of the detector, the peak signal ratio of the large 59.5 keV line in relation to the sum of the peak signals of the 99 keV and 103 keV lines was determined according to Equation 4.12 to compare it to the simulated ratio. Only the Gaussian component of the fit was chosen to represent the peak signal of each line to determine the FCCD, as the low energy tail produced by the Transition Layer effect represents events for which less than the full charge

was collected on the readout electrode.

$$R^{241\text{Am}} = \frac{\epsilon_{59.5\,\text{keV}}}{\epsilon_{99\,\text{keV}} + \epsilon_{103\,\text{keV}}} \, . \tag{4.12}$$

The ratios of the MC simulations with different FCCDs and a linear fit through the ratios are shown in Figure 4.19 for IC48B and IC50B. The calculated high statistics data peak ratio was then aligned onto the fitted line to estimate the FCCDs. The results are listed in Table 4.2.

| Detector | FCCD at 60–100 keV |
|----------|--------------------|
| IC48B | 0.80 mm $\pm$ 0.03 mm (stat.) |
| IC50B | 0.79 mm $\pm$ 0.03 mm (stat.) |

TABLE 4.2: FCCD results at 60–100 keV for IC48B and IC50B from the peak ratio comparison to $^{241}$Am high statistics data. The systematic uncertainties are described in Section 4.3.3.

Since the $^{241}$Am high statistics measurements specifically meant for the FCCD estimation were only available for IC48B and IC50B, a solution had to be found for the other IC detectors. Although the $^{241}$Am scan measurements, described in Section 4.1, did not individually possess enough statistics for analysis, they could be combined into one dataset. The scan data with constant height of the $^{241}$Am source was summed over both scanning angles. Selected regions were removed, namely [-30;-10] mm and [+10;+30] mm in both the x- and the y-dimension, to account for edge effects and to exclude the detector well. In total, 84 spectra were combined with each 300 s data acquisition time for a total of 7 h of statistics. The resulting combined scan data spectrum in comparison to the MC simulations with a Transition Layer is depicted in Figure 4.20 for IC50A. The lower statistics collected in each scan run leads to a slightly higher uncertainty on the data peak fit parameters.

The ratio graphs for IC48A and IC74A are depicted in Figure 4.21. Analogously to the $^{228}$Th analysis, the linear regression through the line ratio plotted against the thickness of the Dead Layer was interpolated to the ratio found in data to estimate the FCCD. The results are shown in Table 4.3.
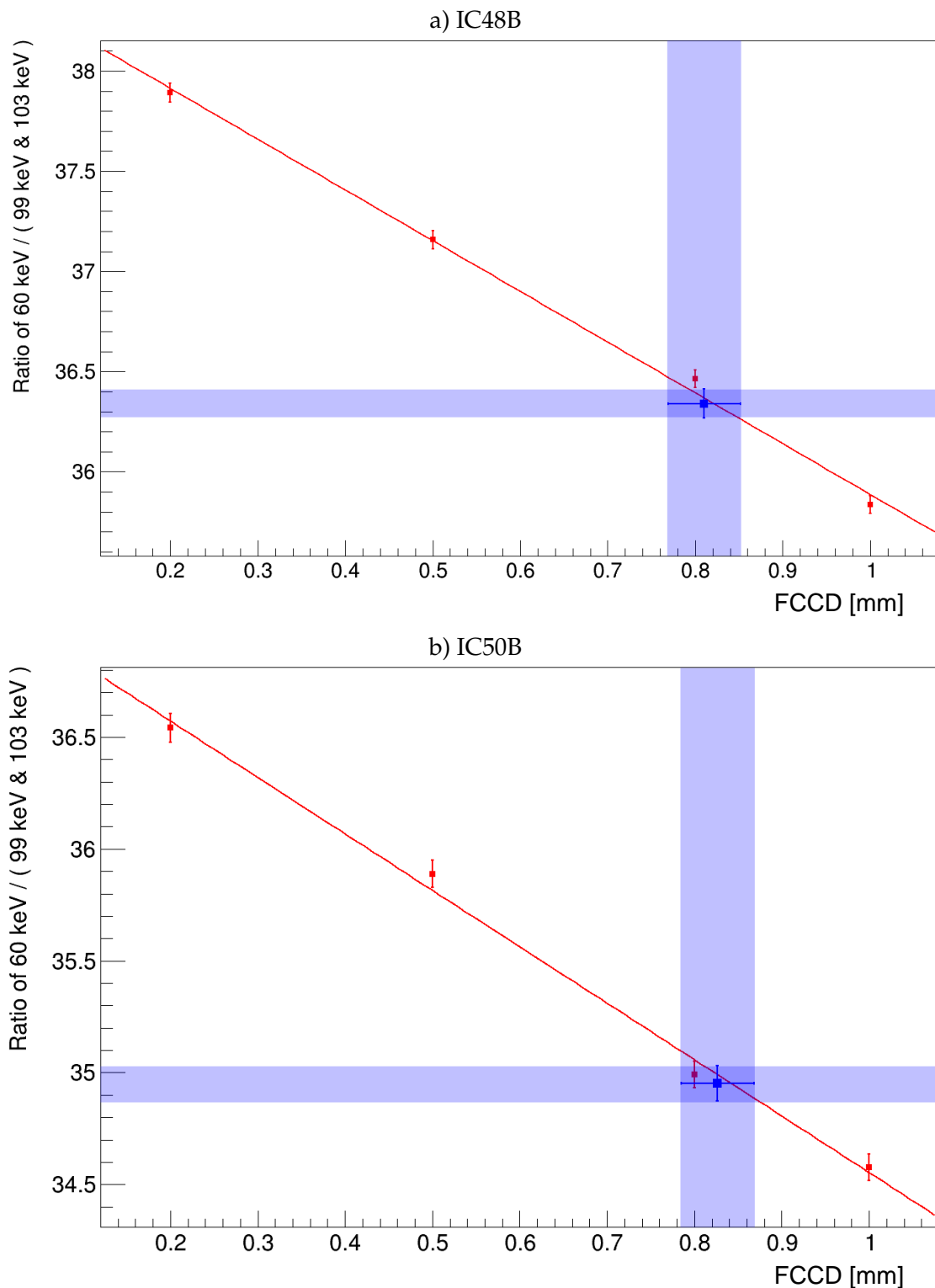
FIGURE 4.19: Peak ratio graphs for $^{241}$Am high statistics: Extracted MC simulated peak ratios (red) for IC48B (top, a) and IC50B (bottom, b) against the simulated FCCDs. The data peak ratio (blue) was then interpolated to the fitted linear curve with the blue data point representing the best fit and the error bars on the y-axis consisting of the uncertainty on the peak fit. The error bars on the x-axis reflect the resulting uncertainty on the determined FCCD.
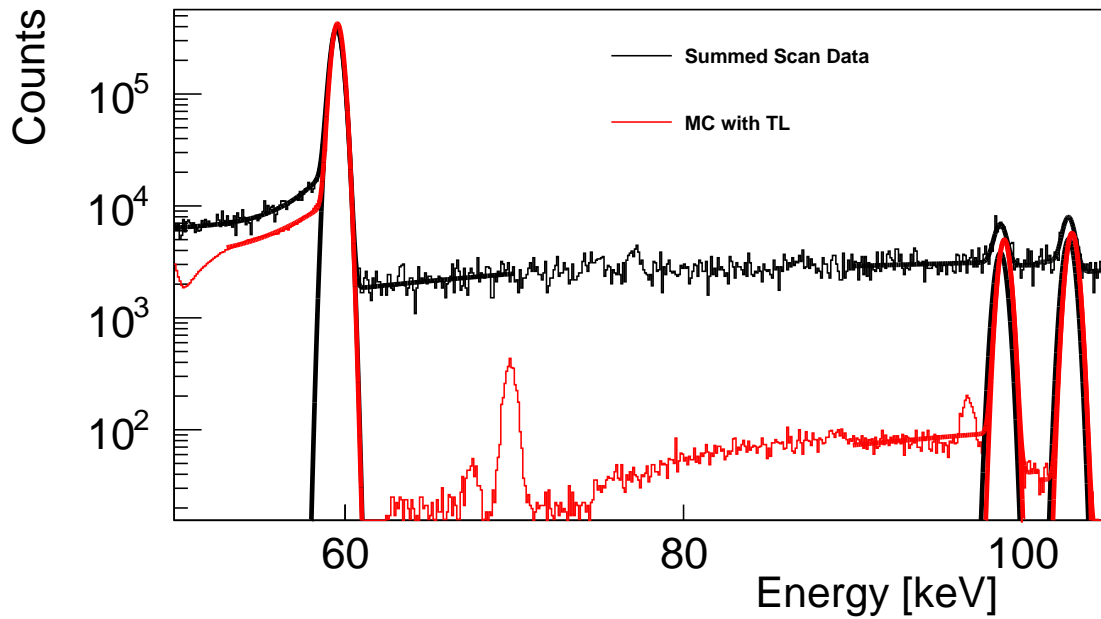
FIGURE 4.20: Combined scan $^{241}$Am spectrum for IC50A: The combined scan data (black) as a summation of 84 spectra is compared to the MC simulations with a Transition Layer (red). The peak fits are shown in bold.

| Detector | FCCD at 60–100 keV |
|----------|--------------------|
| IC48A | 0.82 mm $\pm$ 0.05 mm (stat.) |
| IC50A | 1.03 mm $\pm$ 0.06 mm (stat.) |
| IC74A | 1.14 mm $\pm$ 0.06 mm (stat.) |

TABLE 4.3: FCCD results at 60–100 keV for IC48A, IC50A, and IC74A from the peak ratio comparison to $^{241}$Am combined scan data. The systematic uncertainties are described in Section 4.3.3.
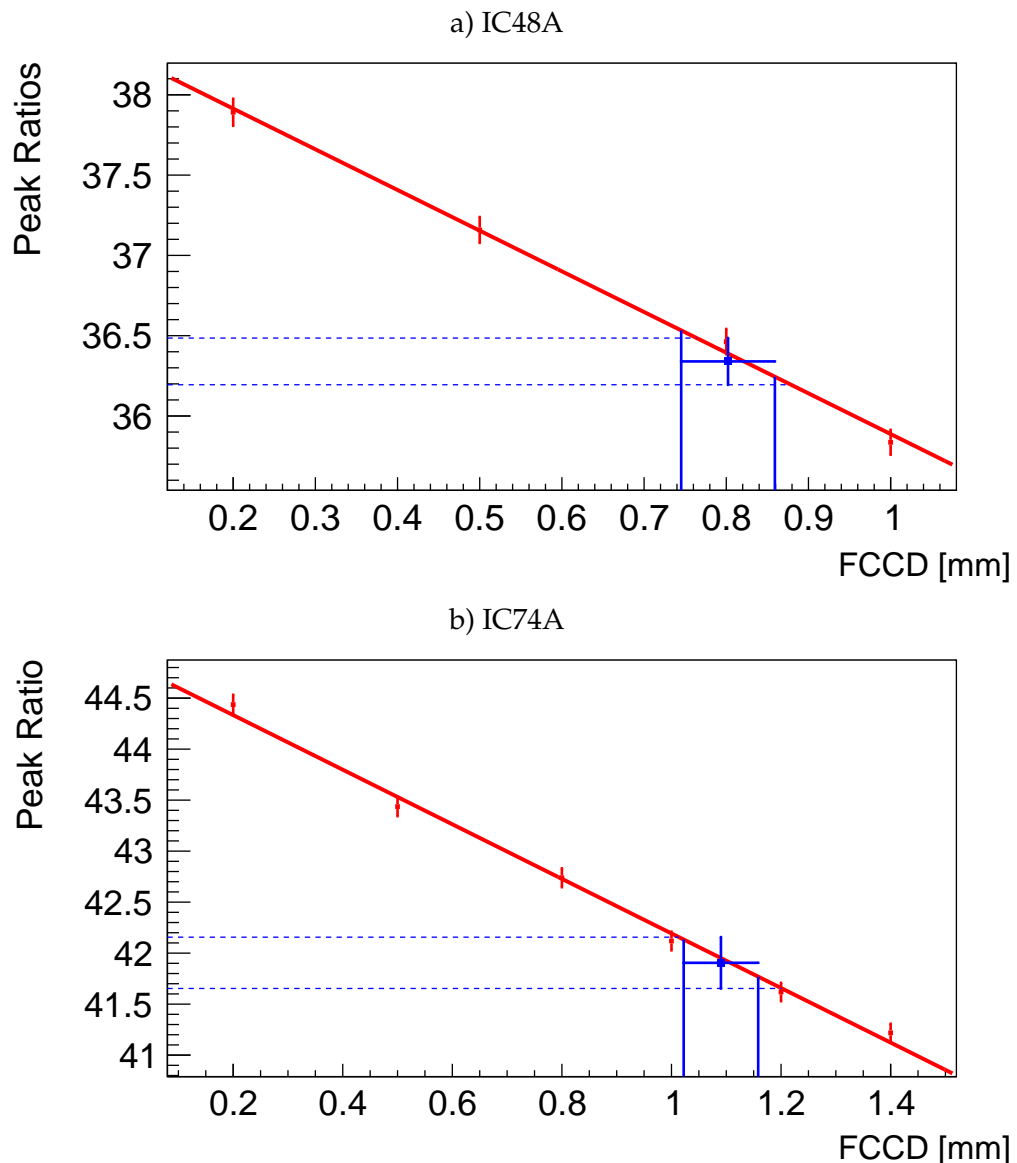
FIGURE 4.21: Peak ratio graphs for $^{241}$Am combined scan: Extracted MC simulated peak ratios (red) for IC48A (top, a) and IC74A (bottom, b) against the simulated FCCDs. The data peak ratio (blue) was then interpolated to the fitted linear curve with the blue data point representing the best fit and the error bars on the y-axis consisting of the uncertainty on the peak fit. The error bars on the x-axis reflect the resulting uncertainty on the determined FCCD.

### 4.3.3   Systematic Uncertainties on Full Charge Collection Depth

The main systematic uncertainties in percentage of the $^{228}$Th and $^{241}$Am peak ratios that affect the FCCD determination and thus the resulting active masses are listed in Table 4.4. The uncertainties have been estimated by varying set-up dimensions according to their systematic uncertainties inside Geant4 and running test simulations and judging the effect on the peak ratios. It is apparent, that the $^{241}$Am measurements are noticeably more sensitive to the detector dimensions and especially to the source distance.

The systematic uncertainties are applied to the FCCD results in Section 4.3.4.

| Category | Systematics | Uncert. $^{228}$Th | Uncert. $^{241}$Am |
|---|---|---|---|
| | Detector dimensions | $\pm3\%$ | $\pm4\%$ |
| | Taper of IC50A | $\pm1\%$ | $\pm0.5\%$ |
| | Holder dimensions | $\pm1.5\%$ | $\pm1\%$ |
| Set-up | Cryostat dimensions | $\pm2\%$ | $\pm1.5\%$ |
| | Distance source/end cap | $\pm1\%$ | $\pm2\%$ |
| | Distance detector/end cap | $\pm0.5\%$ | $\pm2\%$ |
| | Source dimensions | $\pm0.01\%$ | $\pm0.05\%$ |
| MC physics | GEANT4 physics [88] | $\pm2\%$ | $\pm2\%$ |
| | Comb. Uncert. $\gamma$-lines | $\pm0.1\%$ | $\pm1.5\%$ |

TABLE 4.4: List of systematic uncertainties affecting the FCCD determination from the measurement set-up side and the MC simulation side in percent of the calculated peak ratios.

### 4.3.4   Discussion of Full Charge Collection Depth Results

Since the analysis was performed for both $^{228}$Th and $^{241}$Am and estimations were found for all IC detectors, the resulting FCCDs can be directly compared, as shown in Table 4.5. Both techniques are listed side-by-side, as well as the number of annealing cycles from manufacturer Mirion, where the first two cycles are estimated to result in a 0.8 mm FCCD.

There is a good agreement across the $^{228}$Th, $^{241}$Am, and the manufacturer FCCD estimates for detectors IC48A, IC48B, and IC50B that all experienced two cycles

| Detector | $^{228}$Th FCCD results [mm] | $^{241}$Am FCCD results [mm] | A |
|---|---|---|---|
| IC48A | $(0.81 \pm 0.08 \,(\text{stat.}) \pm 0.04 \,(\text{sys.}))$ | **$(0.82 \pm 0.05 \,(\text{stat.}) \pm 0.05 \,(\text{sys.}))$** | 2 |
| IC48B | $(0.78 \pm 0.09 \,(\text{stat.}) \pm 0.04 \,(\text{sys.}))$ | $(0.80 \pm 0.03 \,(\text{stat.}) \pm 0.05 \,(\text{sys.}))$ | 2 |
| IC50A | $(0.86 \pm 0.12 \,(\text{stat.}) \pm 0.05 \,(\text{sys.}))$ | **$(1.03 \pm 0.06 \,(\text{stat.}) \pm 0.06 \,(\text{sys.}))$** | 3 |
| IC50B | $(0.76 \pm 0.09 \,(\text{stat.}) \pm 0.04 \,(\text{sys.}))$ | $(0.79 \pm 0.03 \,(\text{stat.}) \pm 0.05 \,(\text{sys.}))$ | 2 |
| IC74A | $(0.88 \pm 0.13 \,(\text{stat.}) \pm 0.04 \,(\text{sys.}))$ | **$(1.14 \pm 0.06 \,(\text{stat.}) \pm 0.05 \,(\text{sys.}))$** | 4 |

TABLE 4.5: FCCD result comparison for $^{228}$Th at $Q_{\beta\beta}$ and $^{241}$Am at 60–100 keV with A as number of annealing cycles. The $^{241}$Am combined scan results are shown in bold.

and thus increased their FCCD of about 0.4 mm per cycle. Further annealing cycles seem to have added less and less as the method of annealing was changed from electro-magnetic to thermal after the first two cycles. In addition, the heavily lithium doped layer, responsible for the FCCD of the n+ electrode, is not expected to increase linearly as the previously deposited lithium will obstruct the further doping. For IC50A and IC74A, where an increase in the resulting FCCD is expected due to the exposure to more annealing cycles, the $^{241}$Am results reflect this expectation with about 20–23% and 28–31% increase of the best fit FCCD, respectively. For $^{228}$Th, the increase is 6–12% and 8–14%, respectively, although with a higher uncertainty for these detectors. In the previous characterisation campaign for the BEGe detectors, there also appeared a systematic discrepancy between the surface sensitive $^{241}$Am and the bulk sensitive $^{60}$Co (measured using absolute count rates at 1173 keV and 1333 keV) with an average relative difference of 25–27% [87]. An energy dependence of the FCCD was hypothesised due to energy dependent electron-hole cloud sizes, but not further investigated.

Looking at the energy dependence for the IC detectors, a possible explanation for the discrepancy could be the different energies at which the FCCD result was evaluated, coupled with the stronger energy dependence for IC50A and IC74A, as seen in Figure 4.15. If extrapolated down to 100 keV, the FCCD result leads to $(1.03 \pm 0.17 \,(\text{stat.}))$ mm for IC50A and $(1.09 \pm 0.18 \,(\text{stat.}))$ mm for IC74A.

Another factor, anticipated even before the analysis, is the overall sensitivity of the $^{228}$Th sources to the active volume due to its high energy peaks, while $^{241}$Am features much better surface sensitivity. They were expected to match only in a simplified model of homogeneously distributed, constant FCCD. In addition, the $^{228}$Th source measurements, located at an order of magnitude higher distance
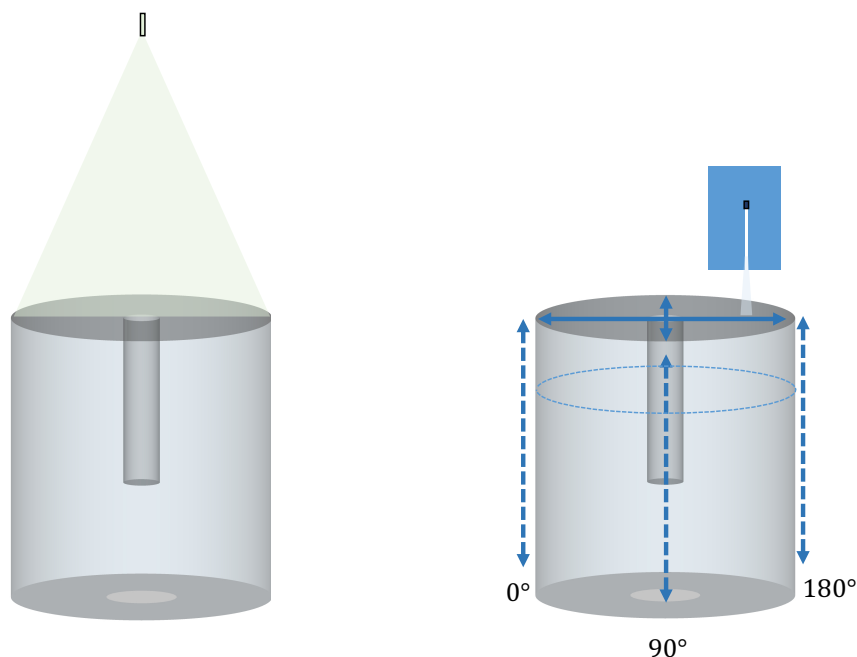
FIGURE 4.22: Measurement schematic for $^{228}$Th (left) covering the full detector and $^{241}$Am (right) pinpointing a highly focused area, possibly affecting their effective FCCD results.

and covering a large area, were probing more of an effective Dead Layer over a bigger area, while the $^{241}$Am combined scan data were highly localised, as illustrated in Figure 4.22.

With the known reliability of the $^{241}$Am approach and its usage in the previous characterisation campaigns, while reflecting the annealing cycles more closely, it was chosen as the main FCCD result. In addition, the its higher FCCDs constrain the active volume more, thus ultimately leading to a more conservative result. The $^{228}$Th analysis was a novel avenue and successful as the first proof of principle of using this source for the determination of the FCCDs. Further investigation into the energy dependence of the FCCD might lead to an even better understanding on the observed discrepancies in this work and the BEGe characterisation campaign. The active volumina and the active masses are calculated in the following Section using the $^{241}$Am result.

## 4.4 Active Mass Determination

In order to determine the active mass from the FCCD results, first the active volume needs to be calculated using the dimensions of the five IC detectors

displayed in Appendix A in Figure A.1 and summarised in Table 4.6. The masses were measured in the GERDA Detector Laboratory (GDL) at LNGS during the detector mounting into the GERDA holders before installation into the GERDA array.

| Detector | IC48A | IC48B | IC50A | IC50B | IC74A |
|---|---|---|---|---|---|
| m – Mass $\pm 0.5$ [g] | 1906.7 | 1808.0 | 1868.2 | 1912.6 | 2072.9 |
| h – Height $\pm 0.3$ [mm] | 80.4 | 80.5 | 80.4 | 85.4 | 82.3 |
| d – Diameter $\pm 0.2$ [mm] | 74.6 | 72.6 | 74.2 / 72.2 | 72.6 | 76.6 |
| $h_w$ – Well bore hole depth [mm] | 47.4 | 56 | 40 | 53.9 | 52.4 |
| $d_w$ – Well bore hole diameter [mm] | 10.5 | 10.5 | 10.5 | 10.5 | 10.5 |
| $h_g$ – Groove depth [mm] | 2 | 2 | 2 | 2 | 2 |
| $d_{ig}$ – Inner groove diameter [mm] | 20 | 15 | 19 | 19 | 19 |
| $d_{og}$ – Outer groove diameter [mm] | 26 | 25 | 27 | 27 | 27 |

TABLE 4.6: Summary of the masses and dimensions of the five IC detectors.

The calculation of the active volume is described in Equation 4.13, consisting of the bulk cylindrical volume decreased in size by the FCCD, while cutting out the inner cylindrical detector well and the holes for the groove. IC50A required the additional addition of the taper length into the calculation. The [241]Am FCCDs of Section 4.3.4 were treated as effective FCCDs and assumed to cover all of the n+ electrode homogeneously. The p+ electrode FCCD was not determined due to its negligible size and thus did not go into the calculation of the active volume.

$$
\begin{aligned}
V_{IC} &= V_{bulk} - V_{well} - V_{groove} \\
&= \pi \cdot \left( \frac{d - 2 \cdot FCCD}{2} \right)^2 \cdot (h - 2 \cdot FCCD) \\
&\quad - \pi \left( \frac{d_w + 2 \cdot FCCD}{2} \right)^2 \cdot h_w \\
&\quad - \left( \pi \cdot \left( \frac{d_{og}}{2} \right)^2 - \pi \cdot \left( \frac{d_{ig}}{2} \right)^2 \right)
\end{aligned}
\tag{4.13}
$$

The resulting active volumina and active volume fractions $f_{AV}$ of the IC detectors are listed in Table 4.7. These quantities are used in the calculation of the $0\nu\beta\beta$ half-life median sensitivity, as explained in Section 2.2.

| Detector | Active Volume | Active Volume Fraction $f_{AV}$ |
|----------|---------------|--------------------------------|
| IC48A | $(323.6 \, ^{+1.4 \, \text{(stat.)}}_{-1.4 \, \text{(stat.)}} \, ^{+4.6 \, \text{(sys.)}}_{-4.5 \, \text{(sys.)}}) \, \text{cm}^3$ | $(92.1 \, ^{+0.4 \, \text{(stat.)}}_{-0.4 \, \text{(stat.)}} \, ^{+1.4 \, \text{(sys.)}}_{-1.3 \, \text{(sys.)}}) \, \%$ |
| IC48B | $(305.6 \, ^{+0.8 \, \text{(stat.)}}_{-0.8 \, \text{(stat.)}} \, ^{+4.3 \, \text{(sys.)}}_{-4.3 \, \text{(sys.)}}) \, \text{cm}^3$ | $(91.7 \, ^{+0.2 \, \text{(stat.)}}_{-0.2 \, \text{(stat.)}} \, ^{+1.3 \, \text{(sys.)}}_{-1.3 \, \text{(sys.)}}) \, \%$ |
| IC50A | $(297.4 \, ^{+1.6 \, \text{(stat.)}}_{-1.6 \, \text{(stat.)}} \, ^{+4.6 \, \text{(sys.)}}_{-4.5 \, \text{(sys.)}}) \, \text{cm}^3$ | $(90.4 \, ^{+0.5 \, \text{(stat.)}}_{-0.5 \, \text{(stat.)}} \, ^{+1.4 \, \text{(sys.)}}_{-1.4 \, \text{(sys.)}}) \, \%$ |
| IC50B | $(325.6 \, ^{+0.9 \, \text{(stat.)}}_{-0.9 \, \text{(stat.)}} \, ^{+4.5 \, \text{(sys.)}}_{-4.5 \, \text{(sys.)}}) \, \text{cm}^3$ | $(92.1 \, ^{+0.2 \, \text{(stat.)}}_{-0.2 \, \text{(stat.)}} \, ^{+1.4 \, \text{(sys.)}}_{-1.3 \, \text{(sys.)}}) \, \%$ |
| IC74A | $(340.1 \, ^{+1.8 \, \text{(stat.)}}_{-1.8 \, \text{(stat.)}} \, ^{+4.7 \, \text{(sys.)}}_{-4.6 \, \text{(sys.)}}) \, \text{cm}^3$ | $(89.7 \, ^{+0.5 \, \text{(stat.)}}_{-0.5 \, \text{(stat.)}} \, ^{+1.2 \, \text{(sys.)}}_{-1.2 \, \text{(sys.)}}) \, \%$ |

TABLE 4.7: Active volume results for all five IC detectors.

The density of enriched germanium after crystal growth was measured by the GERDA Collaboration in the past [86] and resulted in an average value of

$$\rho_{^{76}\text{Ge}} = (5.552 \pm 0.003 \, (\text{stat.}) \pm 0.007 (\text{syst.})) \, \text{g} \cdot \text{cm}^{-3} . \qquad (4.14)$$

Multiplying the density with the calculated active volumina leads to the respective active masses of the IC detectors, shown in Table 4.8.

| Detector | Active Mass |
|----------|-------------|
| IC48A | $(1796.5 \, ^{+7.8 \, \text{(stat.)}}_{-7.8 \, \text{(stat.)}} \, ^{+25.0 \, \text{(sys.)}}_{-24.7 \, \text{(sys.)}}) \, \text{g}$ |
| IC48B | $(1696.8 \, ^{+4.6 \, \text{(stat.)}}_{-4.6 \, \text{(stat.)}} \, ^{+24.2 \, \text{(sys.)}}_{-24.0 \, \text{(sys.)}}) \, \text{g}$ |
| IC50A | $(1651.4 \, ^{+8.9 \, \text{(stat.)}}_{-8.8 \, \text{(stat.)}} \, ^{+25.0 \, \text{(sys.)}}_{-24.8 \, \text{(sys.)}}) \, \text{g}$ |
| IC50B | $(1807.6 \, ^{+4.8 \, \text{(stat.)}}_{-4.8 \, \text{(stat.)}} \, ^{+25.1 \, \text{(sys.)}}_{-24.9 \, \text{(sys.)}}) \, \text{g}$ |
| IC74A | $(1888.4 \, ^{+9.8 \, \text{(stat.)}}_{-9.8 \, \text{(stat.)}} \, ^{+25.9 \, \text{(sys.)}}_{-25.7 \, \text{(sys.)}}) \, \text{g}$ |

TABLE 4.8: Active mass results for all five IC detectors.

## 4.5   Conclusion and Outlook

Five IC detectors were tested using $^{228}$Th and $^{241}$Am sources at the HADES underground facility. The Full Charge Collection Depths (FCCDs) of the detectors, describing the part of the n+ electrode wherein interactions induce no charge or only partial charge, were obtained for both source types by comparing peak

ratios in the data to variable MC ratios. The resulting FCCDs agreed for three out of the five detectors. Two detectors with higher expected FCCDs exhibited a discrepancy in their FCCD increase between the two source types with $^{241}$Am more closely following the trend. The difference could stem from an energy dependence and geometrical considerations creating a difference between the more bulk sensitive $^{228}$Th and the more surface sensitive $^{241}$Am. The $^{241}$Am results were chosen to calculate the active volumina, active volume fractions, and active masses of the IC detectors. Since the installation of the IC detectors into the GERDA array, the results will be used for the active exposure calculation for the $0\nu\beta\beta$-analysis in the next unblinding and for LEGEND in the future.

# Chapter 5

# Pulse Shape Simulations

So far, most types of detector MC simulations for GERDA utilised MaGe, based on Geant4. Instead of simulating the induced charge of particle interactions inside the germanium detectors and inferring the energy, Geant4 saves the energy depositions directly. Energy spectra simulations for comparison with data are thus possible through Geant4, as presented in the previous chapters. Partial charge collection effects had to be implemented through the analysis software after the fact, as described in Section 4.2 for Dead Layers and Section 4.3.2 for Transition Layers. Obtaining parameters that explicitly depend on the germanium detector signal shape, however, requires the simulation of the processes happening inside the semiconductor. An example of such a parameter would be A/E used in Pulse Shape Discrimination (PSD). This chapter describes the development of a framework for Pulse Shape Simulations (PSS) that calculates the movement of electron-hole pairs in the electric field and computes the resulting charge and current induction on the readout electrode of the germanium detectors to create signal waveforms. On the technical side, the Geoextractor interface, explained in detail in Section 5.1, was developed in the frame of this work to bridge the gap between MaGe and the modified field and induction simulation softwares ADL and Siggen, introduced in Section 5.2.1 [89, 90]. The Geoextractor workflow is described in Appendix B. The electric fields of all BEGe (Section 5.2.1) and IC detectors (Section 5.3.1) in GERDA were simulated. Next, the averaged $^{208}$Tl DEP pulses in $^{228}$Th calibration data and simulations were compared to retrieve the electronic response parameters and verify the PSS method for BEGe and IC detectors in Section 5.2.3 and Section 5.3.2, respectively. The Transition Layer effect, observed in Section 4.3.2, was further investigated with PSS of the IC

detectors through the simulation of the A/E distribution in the vicinity of the 59.5 keV line, reinforcing the results of Chapter 4. Section 5.4 summarises the results and presents an outlook for the future of PSS.

## 5.1   Geoextractor Framework

Initially, the development of PSS was faced with a considerable challenge: The existing softwares ADL and Siggen, that were chosen for the simulation of the fields, charge carrier movement, and induction processes, had a vastly different underlying design than MaGe. Whereas MaGe simulates the locations and energy depositions of particle interactions in the whole GERDA array simultaneously and stores the output as a convenient .root files, ADL and Siggen originally possesses only functions (SimulatePulse and get_signal, respectively) that simulate one pulse – the part of the waveform that signifies the induction process for each event by rising up and then back down – for one hit location at a time. Every pulse thus needs to be simulated for one detector at a time, based on the individual detector coordinate system. MaGe MC hit positions, however, are saved in the Geant4 absolute experimental system frame of the array. Furthermore, the building of the structural geometry is based on three different systems: MaGe requires geometry-files for the dimensions and types of the detectors and matrix-files for their location in the string set-up of the GERDA array. They are explicitly called with .mac macrofiles. The input for ADL and Siggen are .txt ConfigFiles and .config files, respectively, for each individual detector. All these parameter files have their own formatting and some of them are binary and not human-readable. All of these issues make the transfer of hit locations and energy depositions a tedious and error-prone manual work. The first efforts were based on a one-off cumbersome visual readout of the hit positions in MaGe to determine efficiencies of the PSD methods for the coaxial detectors [91]. A specific set of geometry and matrix-files was used and even a slight update to them would lead to incompatibility and the readout would have to be remade.

The solution to these issues was the development of Geoextractor, an interface between MaGe, ADL, and Siggen to automatise the input of geometry information, the simulation of the electric fields for each detector, the transfer

of hit locations and energy deposition information, the transformation between coordinate systems, and the multi-threaded execution of the PSS.

The modular approach of Geoextractor is shown in a data flow diagram in Figure 5.1 that visualises the connecting role between available simulation software.
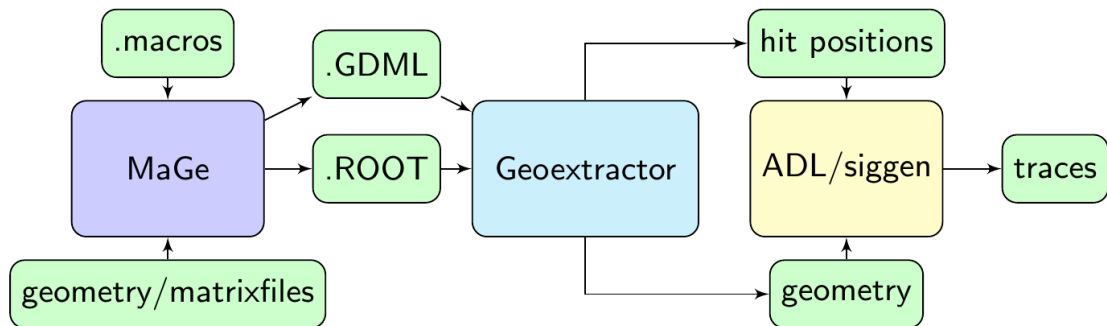


FIGURE 5.1: Geoextractor forms a bridge between MaGe simulations created by macrofiles calling a defined geometry through geometry- and matrix-files. Through the creation of a .GDML file, Geoextractor reads out the geometry, creates geometry files for ADL and Siggen, and transforms the MaGe .root output files into the detector frame. This allows the simulation of signal traces as the final product of this chain.

The input files for MaGe are not blueprints, but rather parameters available to geometry definitions scattered throughout different hardcoded files that are only interacting at run time. To access the geometry built inside MaGe for a given matrix- and geometry-file, it would normally be necessary to modify or inject into MaGe and recompile it for every change or completely recreate the responsible Geant4 code. A creative alternative was found to keep Geoextractor and MaGe free from any reciprocal dependencies by exporting a .GDML file. The Geometry Description Markup Language (GDML) is a Geant4 spin-off project to exchange geometry information independently of application through a specialised XML-based format. It makes use of the same geometry tree logic as Geant4. The full geometry build is thus extracted through a one-time MaGe macro, *gdmlextractor.mac*, stored into a compact .GDML file to remove any direct dependence on MaGe. After running the macro in MaGe once, the produced .GDML file can be used without the need to recompile or even use MaGe. A visualisation of the contents of a .GDML file for the extracted geometry of the GERDA Phase II experiment is shown in Figure 5.2.

How Geoextractor works from a technical side is explained in Appendix B. Geoextractor is capable of autonomously searching through any Geant4 geometry.
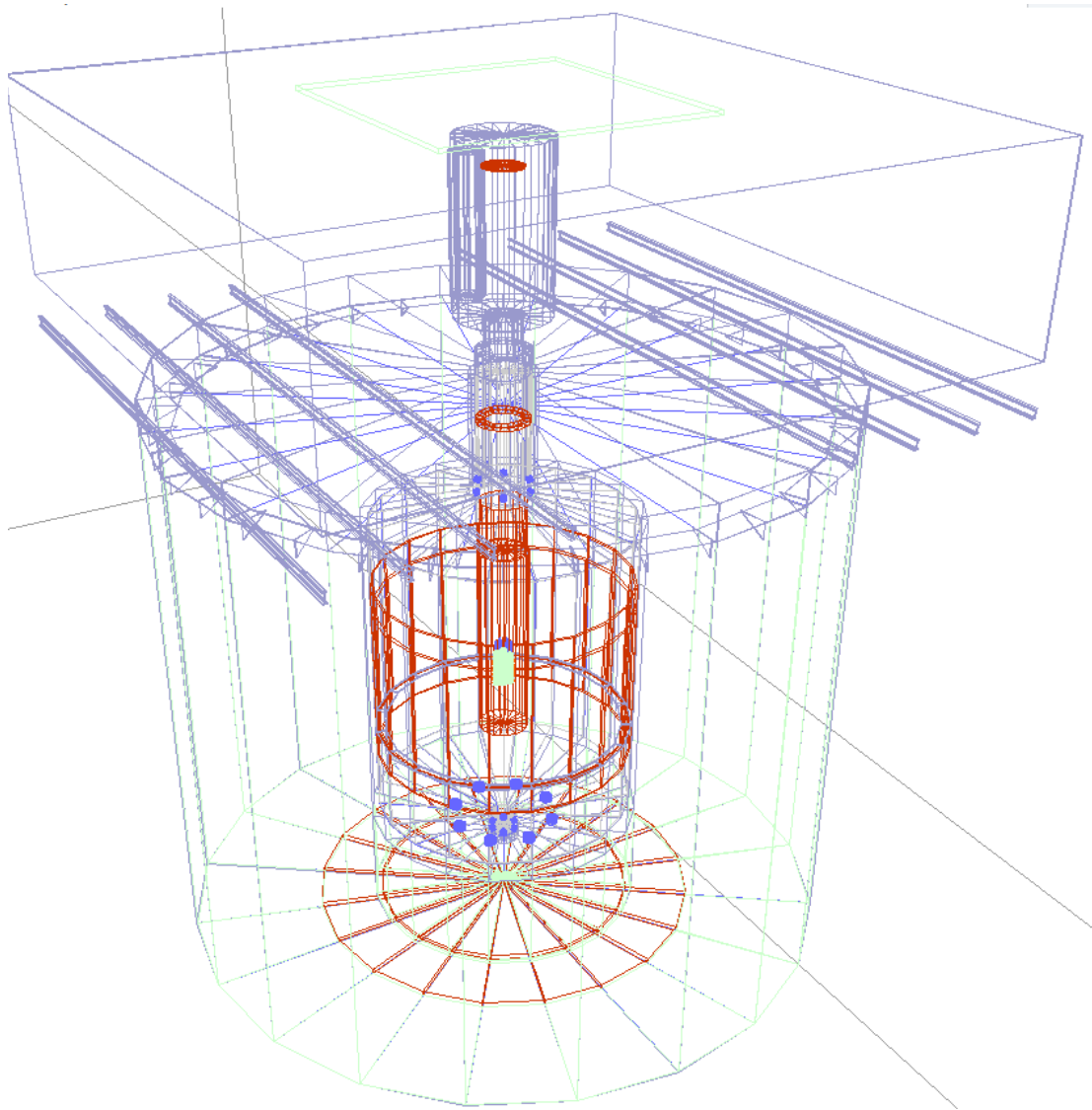
FIGURE 5.2: Extracted geometry of the GERDA Phase II experiment in .GDML
format viewed with OGL. Visible are the clean room above the experiment, the
water tank surrounding it, the cryostat, and in the very center the germanium
detector array itself.

The shape of the identified detector volumes and their position in absolute
MaGe space is retrieved from an auxiliary file, accounting for programmed
dead layer volumes, groove and point contact position, taper, and detector type.
Consequently, Geoextractor will also prove useful for the future of the experi-
ment and for LEGEND as any upgrade with more detectors or new geometries
will automatically be accommodated by the interface. Geoextractor was made
available collaboration-wide and is in use by several members of the background
modelling team for a wide range of applications.

## 5.2 Pulse Shape Simulations for BEGe Detectors

In the following, the softwares for the field, charge carrier movement, and charge induction simulations are described to achieve BEGe detector PSS. Then, a section is dedicated to the comparison of the BEGe detector PSS to data to verify the PSS framework.

### 5.2.1 Field Simulations inside BEGe Detectors

The AGATA Detector simulation Library (ADL) is an existing software to simulate potentials and electric fields inside germanium detectors. The Advanced GAmma Tracking Array (AGATA) experiment aims to build a spherical array of germanium detectors for nuclear spectroscopy and for that purpose developed ADL to reconstruct interaction locations in their segmented germanium detectors through PSS [92]. ADL was adapted for GERDA as ADL 3 [93]. Appendix B explains the technical aspects of ADL and the updates in the framework of this thesis in more detail. The program itself is comprised of a library part capable to compute electric and weighting potentials. Another part of the library is then responsible to calculate the charge drift through these precomputed fields and the induced charge on the read out electrode calculated through the weighting potential. The different potentials and fields are derived from electrodynamics: The electric field results from Gauss' law with charge, written in Equation 5.1, describing the shape and density of the electric field lines originating from the applied high voltage between the two electrodes [94].

$$\nabla \cdot \vec{E}(r,z) = \frac{\rho(r,z)}{\epsilon} \, , \tag{5.1}$$

where $\vec{E}(r,z)$ is the electric field, $\epsilon$ the permittivity, and $\rho(r,z)$ the free charge. The permittivity is given as $\epsilon = \epsilon_0 \cdot \epsilon_r$ with $\epsilon_0$ the vacuum permittivity and $\epsilon_r = 16$ in germanium. The field calculations of ADL are based on the transformation of the three-dimensional cylindrical coordinates of a germanium detector onto a two-dimensional plane, a single slice, due to the assumed azimuthal symmetry. In this way, the fields, field lines, and charge distribution depend only on the r and z coordinates. The electron-hole pairs drift along these field lines to the n+ and p+ electrodes, respectively. This generates space charges, which are

accounted for inside $\rho(r,z)$. The electric field can then be related to the electric potential with

$$\nabla\Phi(r,z) = -\vec{E}(r,z) \, , \tag{5.2}$$

retrieving through Gauss' Law, defined in Equation 5.1, the Poisson equation as

$$\nabla^2\Phi(r,z) = -\frac{\rho(r,z)}{\epsilon} \, . \tag{5.3}$$

The fields are numerically stored with a gridsize of 0.01 mm throughout this work. By means of the granualisation of the detector fields through a finite gridsize, the Successive Over-Relaxation (SOR) algorithm can be employed to solve the Poisson equation iteratively [95]. The electric potential and space charge values for every grid unit, stored in C arrays, are replaced in each step by the average of the surrounding entries, weighted by the difference to the previous field values and the relaxation factor $\omega$, according to

$$\Phi_{i,j}^{new} = \Phi_{i,j}^{old} + \omega \left( \Phi_{i,j}^{new} - \Phi_{i,j}^{old} \right) \, . \tag{5.4}$$

Since this approach replaces the values inside the same array, it is highly memory efficient. The relaxation factor $\omega$ varies as a function of the iteration number: It begins at first as $\omega = 0.4$, when the initial guessed field may be very far from the solution, then is changed to 0.67, and finally goes to 0.9 after 10 iterations to converge the electric potential solution. From the electric potential, the electric field follows through Equation 5.2. In this way, the electric fields and potentials of all the BEGe type detectors were simulated, as shown for an example in Figure 5.3, after implementing their geometry type and dimensions into ADL. These were based on the extracted geometries through Geoextractor.

The impurity concentrations as the space charge distribution inside the detectors were calculated based on the depletion voltages of the detectors determined in the BEGe characterisation campaign and implemented into ADL 3, affecting the electric potentials [86, 87]. The impurities were partly introduced at production time to homogenise the fields for more uniform drift velocities. The drift velocity
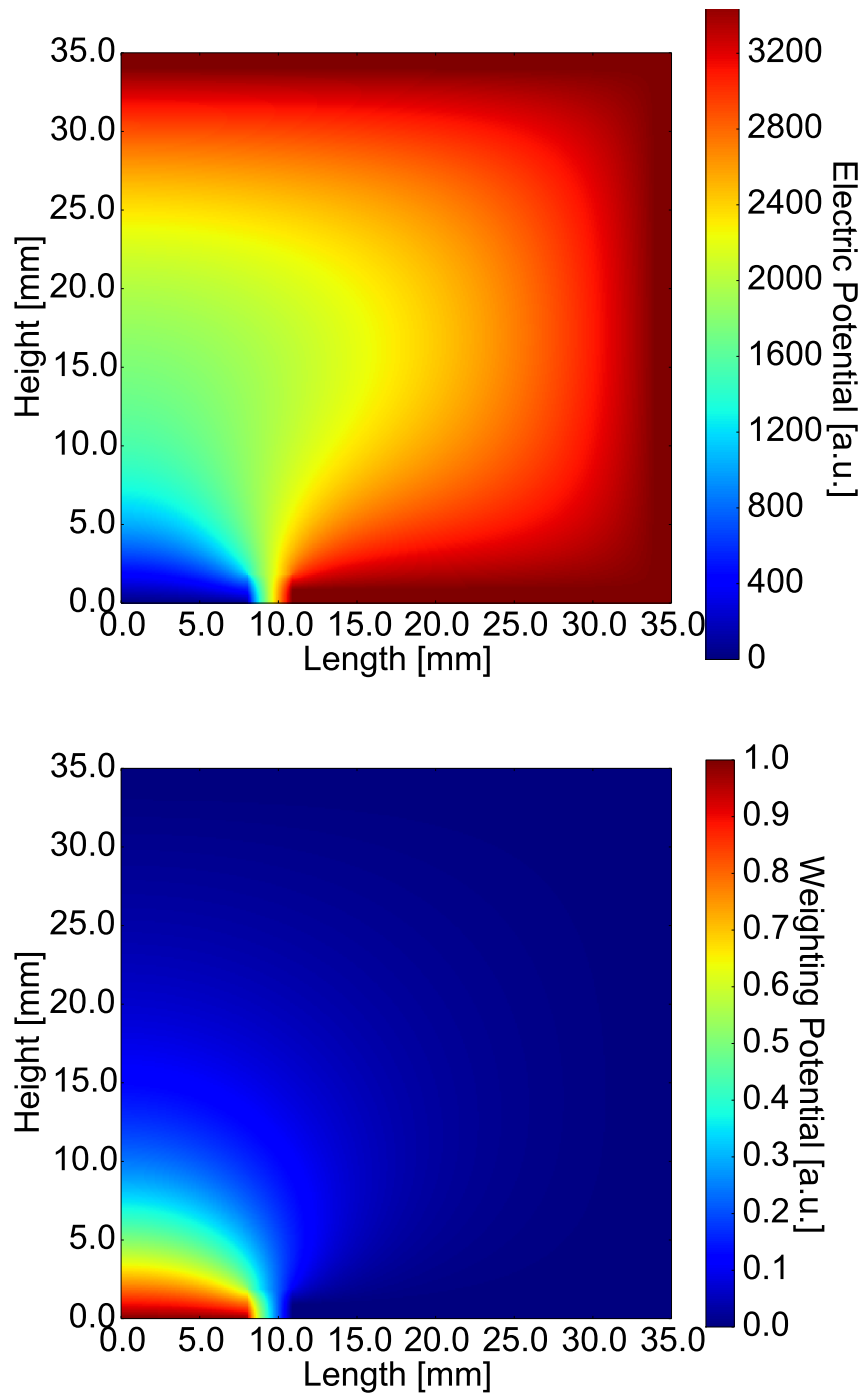
FIGURE 5.3: BEGe detector field simulations: The electric potential (top) of BEGe GD35A, created by applying a 3200 V high voltage, establishes the electric field that determines the calculated path of charge carriers. The weighting potential (bottom) determines the induced charge on the electrode with the Shockley-Ramo Theorem.

of the electrons and holes is calculated from the empirical formula [96] at 77 K

$$v_{\text{drift}} = \frac{\mu_0 \cdot E}{\left(1 + \left(\frac{E}{E_0}\right)^\beta\right)^{\frac{1}{\beta}}} \, .$$ (5.5)

In addition, drift velocity corrections depending on the germanium crystal lattice structure are also part of ADL 3.

## 5.2.2 Induction Simulations inside BEGe Detectors

To calculate the induced charge and current, stemming from the electron-hole drift along the field lines, the Shockley-Ramo theorem is applied, as shown in Equation 5.6, which introduces another type of scalar field – the weighting potential.

$$\dot{Q}_{induced}(\text{t}) = I_{induced}(\text{t}) = -q\nabla\psi(r,z) \cdot v_{\text{drift}}(\text{t}) \, ,$$ (5.6)

where q is the charge of the particle, $\psi(r,z)$ the weighting potential, $v_{\text{drift}}$ the drift velocity of the particle, $\dot{Q}_{induced}$ the induced charge, and $I_{induced}$ the induced current. The Shockley-Ramo theorem conceptualises the induction process as the change of electrostatic flux lines feeding into the electrode. In this way, different simultaneous moving charges can be seen and simulated as decoupled from each other. The weighting potential itself is attained in the calculation by setting the p+ readout electrode to unit potential, the n+ electrode to zero potential, while the charges are ignored. The program thus solves the Laplace equation, defined in Equation 5.7, with the SOR algorithm.

$$\nabla^2\Phi(r,z) = 0 \, .$$ (5.7)

The resulting weighting potential, depicted in Figure 5.3 on the bottom, thus allows, in conjunction with the electric potential, the simulation of the full signal pulse just from the initial single or distributed interaction positions and energy depositions of the particle. The Laplace equation needs to be solved only once for each detector as the induction can then be calculated from the saved weighting potential matrix, optimising simulation performance. An example BEGe signal pulse is shown in Figure 5.4.
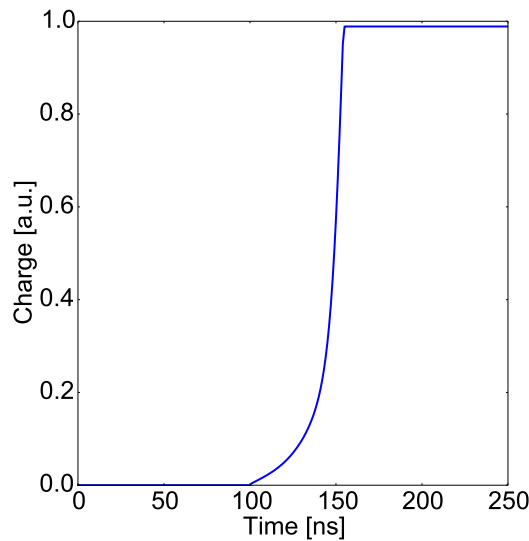
FIGURE 5.4: Pulse Shape Simulation (PSS) of BEGe GD35A from the calculation of the movement of the charge carriers originating in a single interaction at $(r, z) = (15, 15)$ mm. The charge carriers are moved through the electric potential (Figure 5.3, top) with a drift speed, inducing a charge on the readout electrode, calculated by moving the charge carriers through the weighting potential (Figure 5.3, bottom).

Just like ADL 3, Siggen is a program that allows the simulation of signal pulses from these simulated weighting potentials of the germanium detectors in conjunction with the previously simulated fields. Its advanced diffusion and charge cloud size simulation capabilities proved especially advantageous for the simulation of the Transition Layer (TL) in Section 5.2.1 [90]. It also features temperature dependent electron-hole pair mobilities affecting their drift velocity and diffusion coefficient depending on the electric field strength [97]. Originally developed by David Radford, Siggen was made part of the PSS framework chain through its implementation with *julia*, a high-level programming language from MIT, capable of working with foreign functions from both C and Python [98]. This allowed the introduction of a sophisticated electronic response module to convolve the PSS output in the production chain, based on the Python version, utilising the scipy library, of a previous work [91]. The electronic response models the slowed pulse rise observed in data due to the finite bandwidth of the pre-amplifier, as well as the exponentially falling slope after the peak, caused by the discharge of the feedback capacitor. The module simulates a circuit, as illustrated in Figure 5.5, containing a 1-pole filter amplifier, feedback capacitor, and feedback resistor.

The impulse response of the circuit to the signal can be attained through Laplace
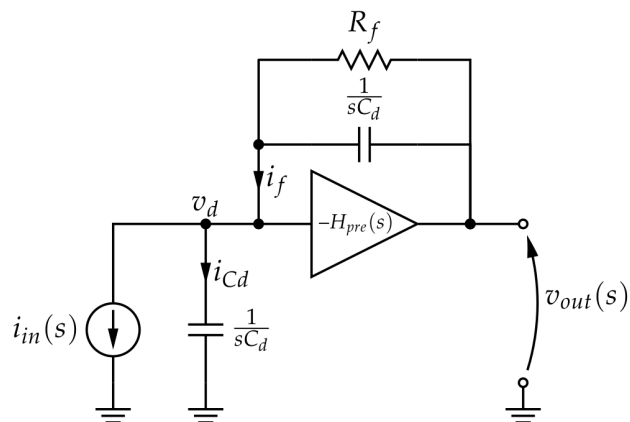
FIGURE 5.5: Schematic of the circuit simulated in the electronic response module implemented into julia, based on a Python version of a previous work [91].

analysis. The transfer function $H(s)$ depends on the Gain-Bandwidth Product (GBP) of the amplifier, the capacitances, and the resistance. The inverse Laplace transform of the transfer function results in the impulse response $h(s)$ depending on the signal $s$, according to

$$h(s) = \mathcal{L}^{-1}\{H(s)\} . \tag{5.8}$$

Furthermore, a module was programmed to extract the noise profile from the 80 $\mu s$ long baseline in GERDA data waveforms for each detector, depicted in Figure 5.6.
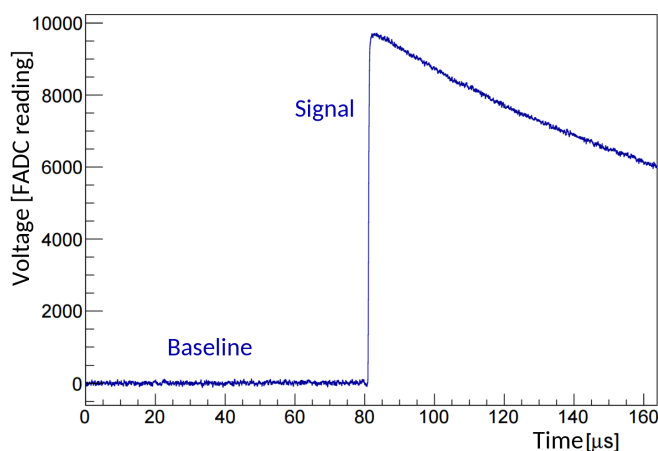


FIGURE 5.6: The 80 $\mu s$ long baseline in the GERDA data, preceding the signal pulse, served as the noise profile for the PSS.

The signal is thus first convolved with the impulse response $h(s)$, then random noise sampled from the noise profile library is introduced to create realistic pulse

shapes. Figure 5.7 shows a comparison between simulated pulses before and after the application of the electronic response and noise profile modules. The induced charge is differentiated to retrieve the induced current. An exponential decay of the charge pulse and a slowed rise of both the charge and current pulse were thus achieved.
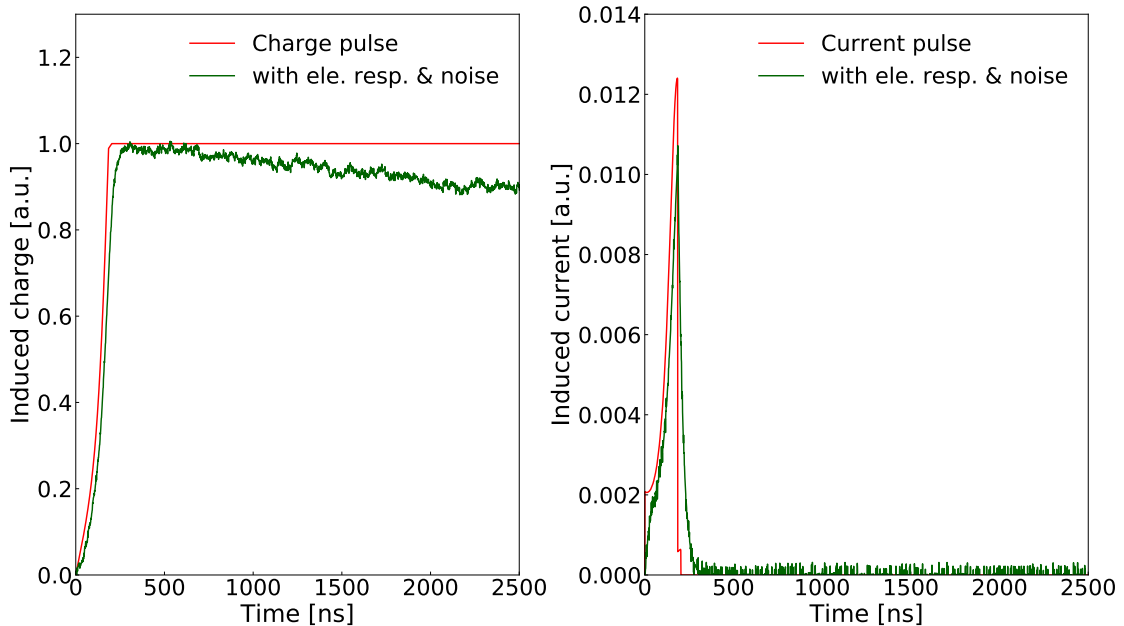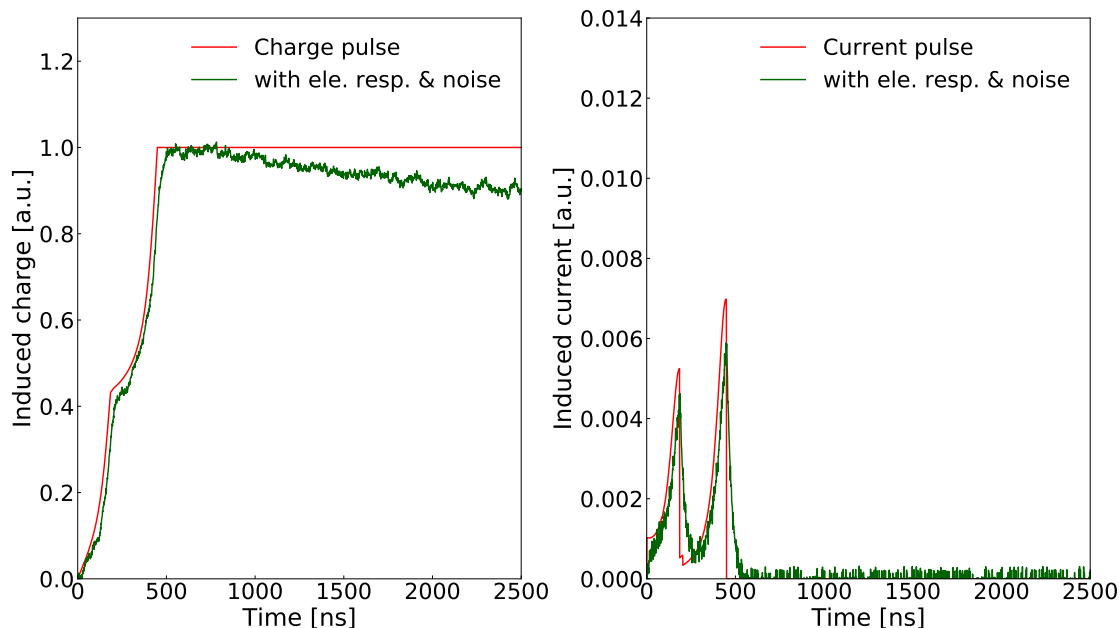


FIGURE 5.7: Pulse shape simulation of a SSE showing the impact of the electronics response and noise module (green) in comparison to an unconvolved simulated pulse (red). In addition, noise extracted from baselines of data waveforms, as shown in Figure 5.6, is added to make the signal even more realistic. Left: Charge pulse, right: Current pulse from differentiation.

The point contact shapes the electric field in BEGes and IC detectors to be the strongest in the vicinity of the p+ electrode. Consequently, holes move along similar trajectories towards it, inducing a characteristic pulse shape, regardless of initial interaction location. For a single current pulse originating from a SSE, the maximum height of the induced charge is proportional to the total energy. If that energy is, however, distributed into several interaction locations, such as from Compton scattered $\gamma$-particles, the resulting MSE is made identifiable by the multiple similar current pulse peaks partially separated in time. Different drift times are responsible for the time delay between peaks. In this case, the maximum current amplitude A is different from the total energy E, divided up into the different peaks, thus enabling PSD to discern SSEs from MSEs through the A/E ratio.

FIGURE 5.8: Pulse shape simulation of a MSE showing the impact of the electronics response module (green) in comparison to an unconvolved simulated pulse (red). In addition, noise extracted from baselines of data waveforms is added to make the signal even more realistic. Left: Charge pulse, right: Current pulse from differentiation.

Modelling the electronic response was an important step towards simulating and comparing the virtual pulses to the ones from real data. The next section reports on the direct comparison of simulated pulses with real pulses from GERDA Phase II data.

### 5.2.3 Verification of BEGe Detector Pulse Shape Simulations with Data

To replicate the shape of the real pulses to the virtual ones, the Gain-Bandwidth Product (GBP) parameter of the electronic response convolution, responsible for the rise time of the pulse, and the exponential decay time $\tau$ needed to be determined from a direct comparison to data for every detector. Ideally suited for that task is the Double Escape Peak (DEP) of the $^{208}$Tl component in the $^{228}$Th decay chain, available in abundance in the calibration data. This phenomenon is described in more detail in Section 2.5. Unlike the Full Energy Peak (FEP) at 2615 keV, that stems from a mix of SSE and MSE total absorption events, the dominant event topology for the DEP at 1593 keV are SSEs. This is due to the escape of both 511 keV $\gamma$-particles from the detector, that originated in the

positronium decay generated by the positron of a pair production event, leaving only the initial short ranged positron and electron to deposit their energy in a single location. The waveforms of the events reflect this behaviour: Pulse shapes taken from the $^{228}$Th calibration data FEP exhibit a lot of variation, whereas the predominantely SSEs in the DEP induce a characteristic shape, as illustrated in Figure 5.9.
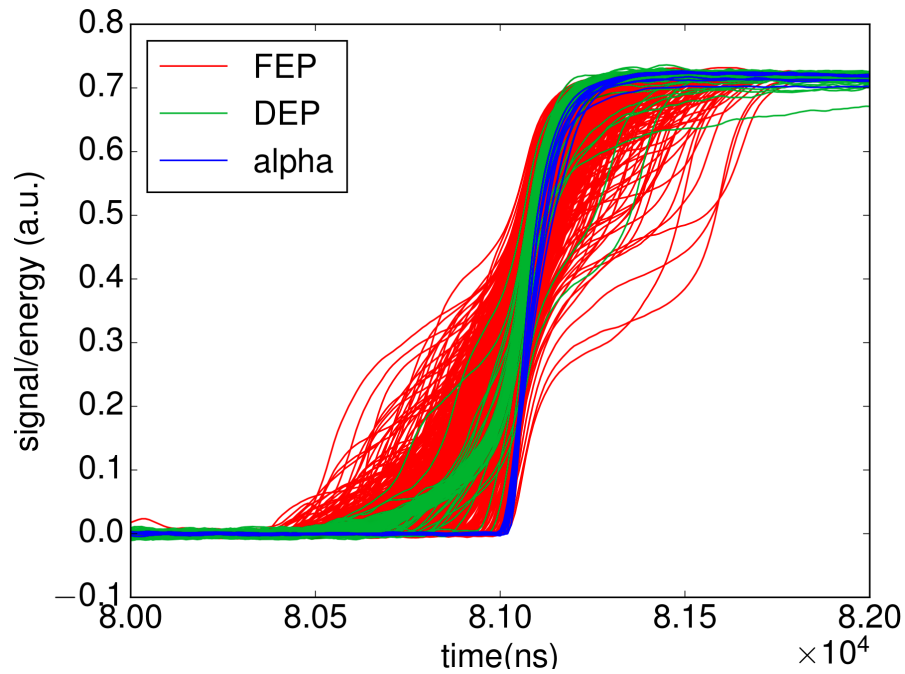


FIGURE 5.9: Waveforms of $10^4$ events taken from the $^{228}$Th calibration data FEP (red) and DEP (green) combined with $\alpha$-particles (blue) at energies beyond the FEP were stacked on top of each other as an illustration: The SSEs found in the DEP induce a characteristic pulse shape in comparison to events from the FEP. The $\alpha$-event waveforms coming from energies beyond the limit of natural $\gamma$-ray emission through radioactivity also induce a unique shape as they enter the detector exclusively as SSEs through the p+ electrode's negligible FCCD.

To compare SSEs from PSS to these SSEs from data, $^{228}$Th calibration simulations of the GERDA array were performed in MaGe. The simulated hits in the DEP were converted into a matrix and transformed from the GERDA array coordinate system into each detector's own frame using Geoextractor. Calibration data events in a range of 1591–1594 keV were chosen to target DEP events and filtered additionally according to their A/E classifier. Next, the averaged simulation and data waveforms were aligned at half their full height and compared through a $\chi^2$-minimisation, separately for each detector. An example is shown in Figure 5.10, where an excellent agreement is seen for GD00A, as evidenced by its minimal residual and small p-value of 0.0016.
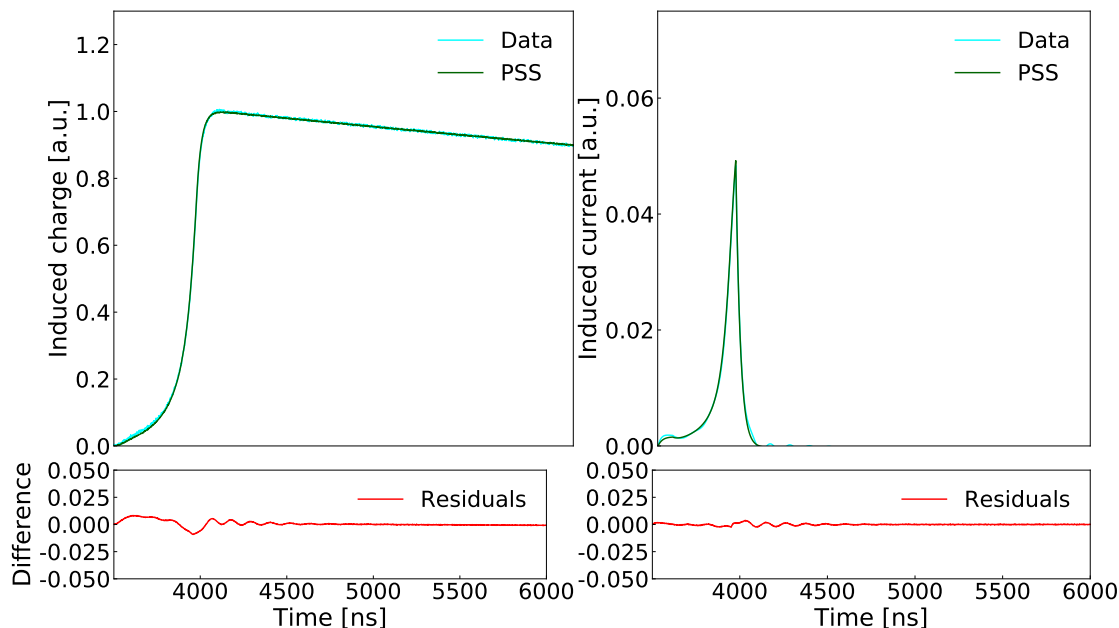
FIGURE 5.10: Verification of BEGe Detector PSS using averaged data from the DEP of $^{208}$Tl. Top: Averaged simulated pulses (green) in comparison to averaged data pulses (cyan). Bottom: Corresponding residual (red)s of simulations to data for charge and current. The $\chi^2$-minimisation resulted in a p-value of 0.0016 for GD00A.

The results for the GBP and $\tau$ parameters of the pre-amplifier, which influence the rise time and the decay time of the waveform, from data matching are gathered in Table 5.1 for all BEGe detectors in GERDA.

## 5.3 Pulse Shape Simulations for IC Detectors

After creating the PSS framework and verifying it for the BEGe detectors, the goal was adapt it for the IC detectors. This section describes the further advances achieved for the PSS softwares and their application for the IC detector field simulations, verification to data, and the implementation of a Transition Layer to compare to the observations of Section 4.3.2.

### 5.3.1 Field and Induction Simulations inside IC Detectors

New multi-threaded parallel computing capabilities assisting in the IC detector field simulations and later in the simulation of entire germanium detector arrays of GERDA and LEGEND were implemented into ADL to form a new package,

| Detector | Channel | GBP $[10^9]$ | $\tau$ [µs] | p-value ($\chi^2$) |
|----------|---------|--------------|-------------|-------------------|
| GD91A | 0 | 4.48 | 140 | 0.0134 |
| GD35B | 1 | 4.52 | 131 | 0.0189 |
| GD02B | 2 | 3.27 | 112 | 0.0006 |
| GD00B | 3 | 2.42 | 122 | 0.0012 |
| GD61A | 4 | 3.11 | 109 | 0.0057 |
| GD89B | 5 | 1.79 | 125 | 0.0029 |
| GD02D | 6 | 1.66 | 103 | 0.0036 |
| GD91C | 7 | 1.98 | 113 | 0.0075 |
| GD02A | 11 | 4.77 | 114 | 0.0046 |
| GD32B | 12 | 3.13 | 104 | 0.0277 |
| GD32A | 13 | 3.21 | 107 | 0.0009 |
| GD32C | 14 | 3.17 | 101 | 0.0018 |
| GD89C | 15 | 3.18 | 126 | 0.0033 |
| GD61C | 16 | 2.22 | 111 | 0.0006 |
| GD76B | 17 | 3.07 | 141 | 0.0296 |
| GD00C | 18 | 4.89 | 116 | 0.0039 |
| GD76C | 20 | 3.37 | 109 | 0.0311 |
| GD89D | 21 | 4.44 | 127 | 0.0025 |
| GD00D | 22 | 3.12 | 100 | 0.0031 |
| GD79C | 23 | 2.96 | 133 | 0.0042 |
| GD91B | 25 | 2.09 | 129 | 0.0692 |
| GD61B | 26 | 2.55 | 126 | 0.0071 |
| GD00A | 30 | 5.03 | 114 | 0.0016 |
| GD02C | 31 | 4.56 | 112 | 0.0018 |
| GD79B | 32 | 4.23 | 98 | 0.0051 |
| GD91D | 33 | 3.08 | 131 | 0.0228 |
| GD32D | 34 | 2.76 | 108 | 0.0004 |
| GD89A | 35 | 2.23 | 116 | 0.0033 |

TABLE 5.1: Electronic response parameter results of Gain-Bandwidth Product (GBP) and $\tau$ of the exponential decay of the pre-amplifier for all BEGe detectors .

ADL 4. This is to be able to compile it together with ROOT, GEANA (Gerda Analysis Package), and Geant4. In an effort to further unify ADL 4 and Siggen, the temperature dependent electron-hole pair mobilities were also integrated [97]. The IC detector geometry with its point contact readout electrode and its bore hole were implemented into ADL 4 for this work and the electric fields, electric potentials, and weighting potentials of the five IC detectors described in Chapter 4 were simulated. An example of the simulated IC detector fields can be seen in Figure 5.11.

The IC detectors were then implemented into the induction and PSS framework and each module was adapted to suit the IC detector geometry. After this is accomplished once for a detector type, Geoextractor is capable of transmitting the event coordinates throughout the PSS chain.

### 5.3.2  Verification of IC Detector Pulse Shape Simulations with Data

In the IC detector characterisation campaign, described in Section 4.1, data was acquired both with an MCA to save histograms directly and an FADC to save the time dependent charge collection information in waveforms. The energy, current, amplitude, and rise time were then retrieved from these waveforms through waveform processing, mimicking the waveform processing in GERDA. Using the FADC data, the recorded waveforms can be compared to simulated ones.

In the same vein as the verification of the BEGe Detector PSS, described in Section 5.2.3, the IC Detector PSS had to be verified and the electronic response parameters GBP and $\tau$ needed to be extracted to match the data pulse shape. For this purpose, the $^{228}$Th calibration simulations, performed in the framework of the IC Detector characterisation campaign in Chapter 4, were employed. The simulated hits in the DEP were converted into a matrix and transformed from HADES facility coordinate system in MaGe into each detector's own frame using Geoextractor. A/E filtered calibration data events in a range of 1591–1594 keV were chosen to target DEP events. Next, the averaged simulation and data waveforms were compared through a $\chi^2$-minimisation. Figure 5.12 illustrates
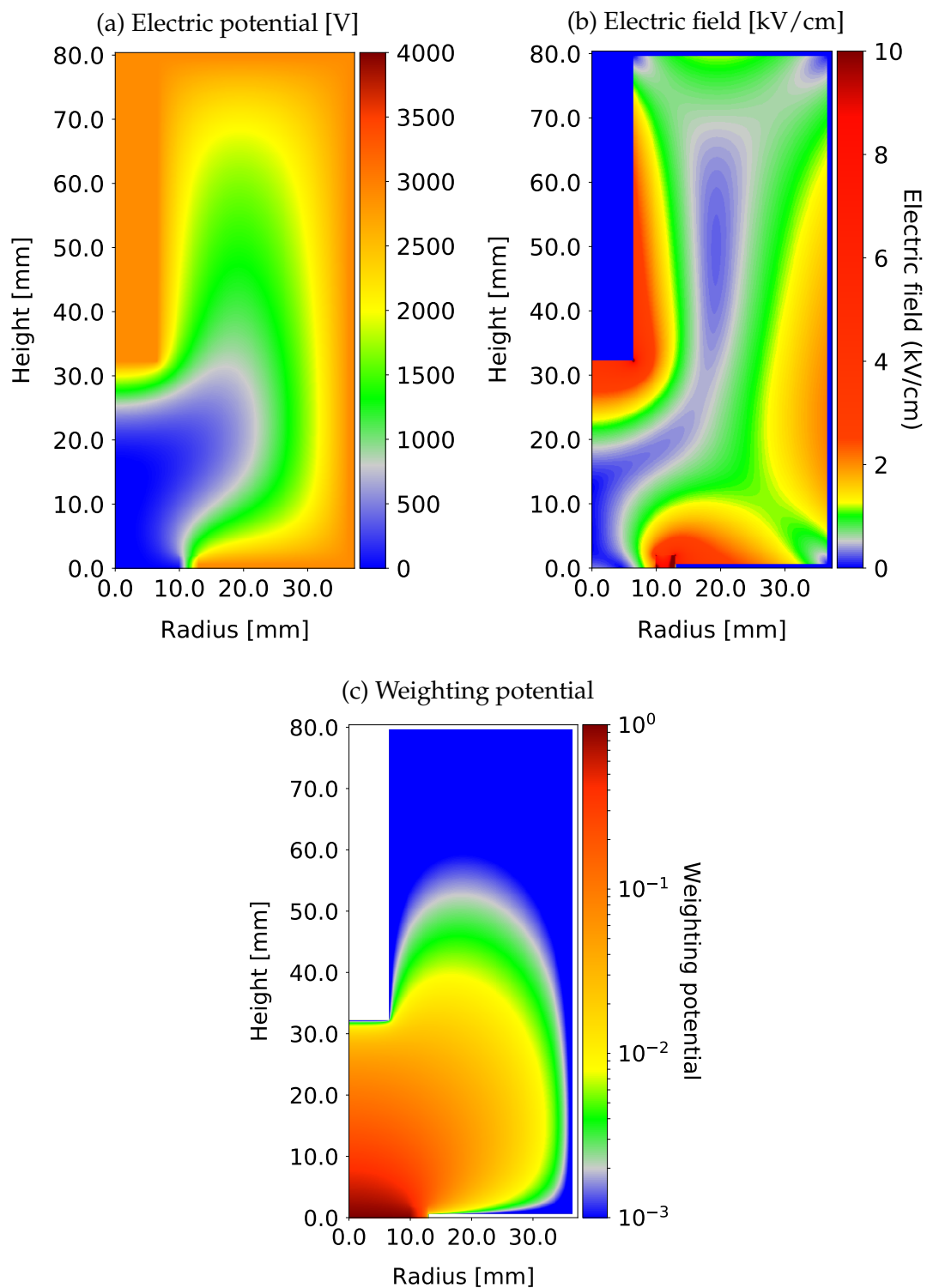
FIGURE 5.11: IC detector field simulations: The electric potential (a) of IC48A, created by applying high voltage to the depletion voltage of 2900 V, establishes the electric field (b) that determines the calculated path of charge carriers. The weighting potential (c) allows the calculation of the induced charge on the readout electrode with the Shockley-Ramo Theorem.

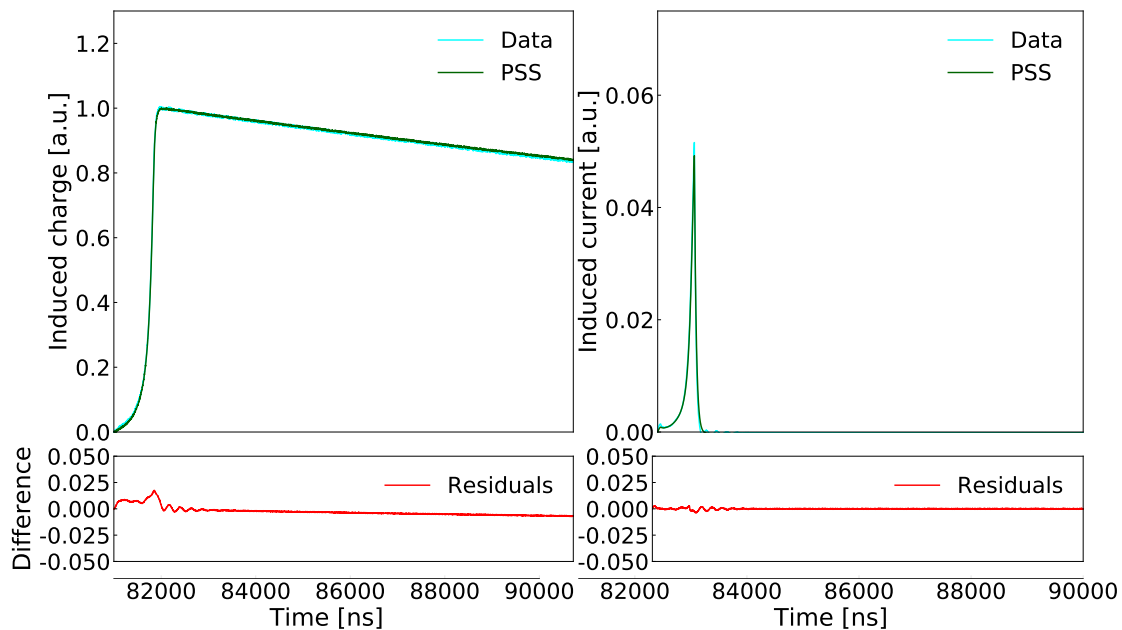the results for IC48A, where an excellent agreement was found with a p-value of 0.0034.



FIGURE 5.12: Verification of IC Detector PSS using averaged data in the DEP of $^{208}$Tl. Top: Averaged simulated pulses (green) in comparison to averaged data pulses (cyan). Bottom: Corresponding residuals (red) of simulations to data for charge and current. The $\chi^2$-minimisation resulted in a p-value of 0.0034 for IC48A.

The results of the electronic response parameters from the matching are gathered in Table 5.2 for all five IC detectors.

| Detector | GBP [$10^9$] | $\tau$ [µs] | p-value ($\chi^2$) |
|---|---|---|---|
| IC48A | 4.48 | 174 | 0.0034 |
| IC48B | 4.52 | 181 | 0.0057 |
| IC50A | 3.27 | 132 | 0.0041 |
| IC50B | 2.42 | 198 | 0.0094 |
| IC74A | 3.11 | 159 | 0.0132 |

TABLE 5.2: Electronic response parameter results of Gain-Bandwidth Product (GBP) and $\tau$ of the exponential decay of the pre-amplifier for all all five IC detectors.

### 5.3.3  Transition Layer Simulations with IC Detector PSS

The characteristic shape of an IC detector pulse is caused by the strongly peaked weighting potential near the readout electrode due to the small size of the p+ contact in comparison to the outer dimensions. SSEs and MSEs thus feature single or stacks of similar pulses with an initial delay, corresponding to the distance from the interaction point to the readout electrode. Events that exceed this range in rise time stem from the creation of charge carriers in the Transition Layer of the n+ electrode. Even though the charge carriers are shielded through the lithium doping from accelerating in the electric field, they still manage to reach the active volume through the process of diffusion. Because of the slow nature of diffusion in comparison to the much faster field drift, the event topology is recognised as so-called *slow pulses*. The pulse integration time for the maximum current amplitude A of a slow pulse is thus much shorter than the one for the total energy E, leading to a strongly reduced A/E ratio in comparison to SSEs. The increased rise time induces a ballistic deficit in the energy reconstruction, visible as a low energy tails of peaks in the energy spectrum.

In Section 4.3.2, the low energy tail of the 59.5 keV peak in the $^{241}$Am spectrum was assumed to originate from a Transition Layer effect, as it could not be replicated otherwise in the simulations. Additional evidence for the effect came in the form of the A/E distribution of the low energy tail, shown in Figure 4.17, where a majority of the low energy tail events featured a $A/E < 1$ classifier, typical for Transition Layer slow pulses. Using PSS, the phenomenon could be investigated further by simulating the diffusion process and studying its effect on the A/E distribution of a $^{241}$Am source measurement.

For that purpose, a diffusion module was employed in the simulation chain, that allowed the simulation of a diffusion zone inside the Transition Layer to convolve the Siggen output to emulate the degraded signal shape [90]. This enabled the simulation of slow pulses using the PSS framework. Figure 5.13 illustrates the difference in rise time for a SSE in the bulk volume and charge carrier in the Transition Layer of the n+ electrode that slowly diffuses into the active volume, where it induces a slow pulse on the readout electrode.

Events from the $^{241}$Am simulations below 62 keV were selected, transformed using Geoextractor into an event matrix in the detector frame, and placed into the fields of the IC detectors to calculate their drift velocity and the resulting
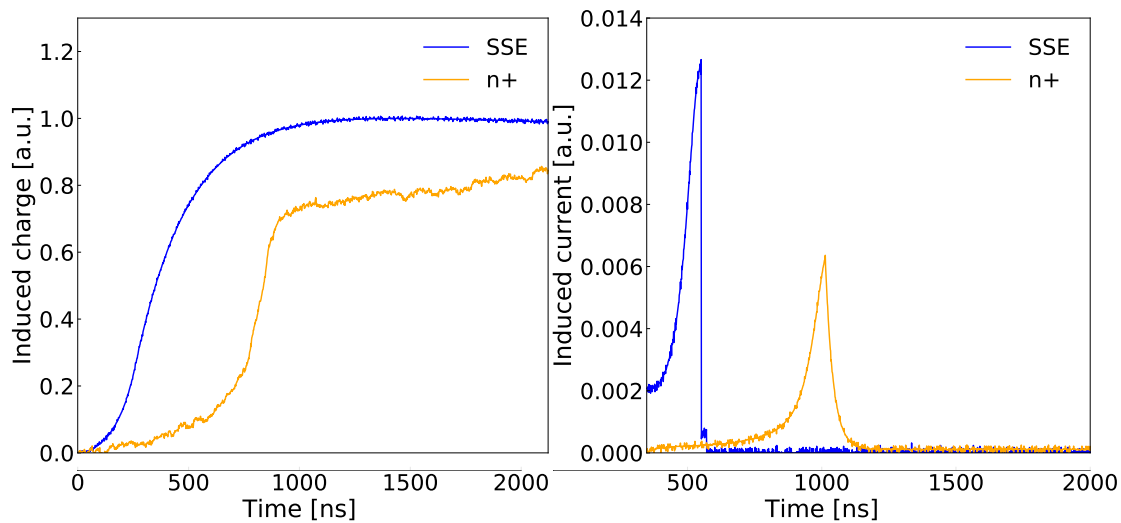
FIGURE 5.13: Comparison of simulated SSE (blue) in the bulk of an IC detector and a simulated slow pulse (orange) originating on the n+ electrode. Due to the convolution with the simulation of diffusion effects, the slow pulse exhibits a much higher rise time than the SSE.

induction on the readout electrode with Siggen. Diffusion was simulated for hits that interacted in the virtual Transition Layer of size 0.6 mm, through the convolution of the induction signal. Then the signal was further convolved with the electronic response module using the parameters obtained in Section 5.2. By utilising the same waveform processing on the simulated pulses as for the FADC data, discussed in Section 5.2.2, the energy, current, amplitude, rise time, and thus A/E were calculated in the same way. The A/E classifiers of all the simulated pulses were then plotted in Figure 5.14, as a function of energy on a two-dimensional histogram, and normalised with the SSE band equalling unity.

The events in the 59.5 keV peak are a mixture of SSEs and MSEs with $A/E = 1$ and $A/E < 1$, respectively. Below the peak, especially low A/E values begin to appear, which were identified as slow pulses in individual waveform view. The shape of the slow pulse A/E distribution induced by the Transition Layer is similar the one observed in Figure 4.17 for data. This result served as a further proof of the Transition Layer effect, which was simulated in the last chapter to achieve the best match to data for the most accurate FCCD determination of the IC detectors.

(a) Simulation

(b) Data
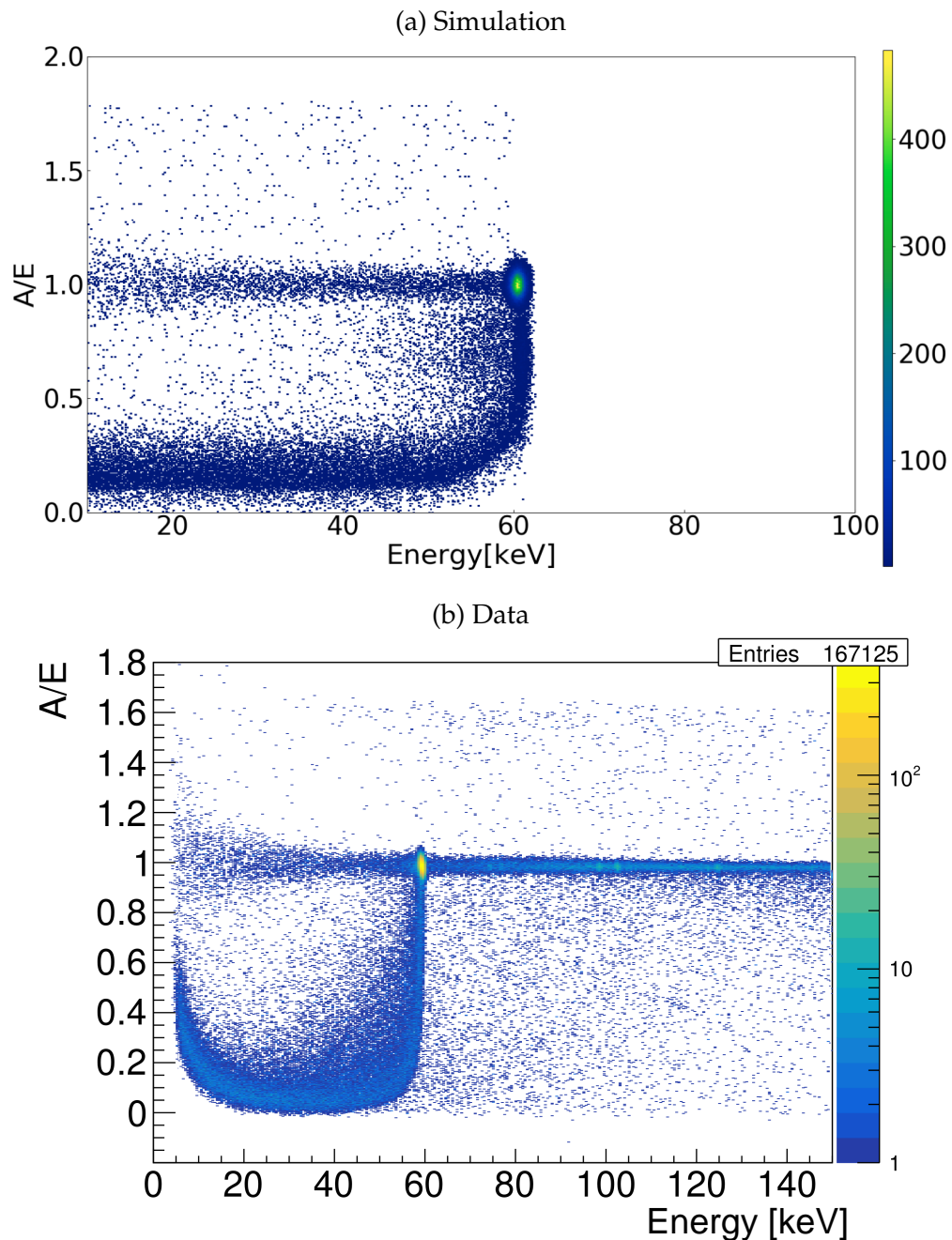
FIGURE 5.14: A/E distribution of PSS using $^{241}$Am 59.5 keV peak simulations (top). With the introduction of a 0.6 mm TL, the low A/E tail below the 59.5 peak can be replicated similar to the shape observed in data (bottom).

## 5.4   Conclusion and Outlook

A framework for PSS was developed that allows the transformation of MaGe based hit location and energy deposition simulations into simulated fields of germanium detectors to calculate the induced charge and current that is further convolved to include diffusion effects, electronic response, and baseline

noise. The geometries of BEGe and IC detectors were implemented and the PSS framework was verified for both detector types with averaged $^{208}$Tl DEP pulses from $^{228}$Th calibration data. In the process, the electronic response parameters for all detectors were retrieved. The low energy tails observed in IC detector $^{241}$Am source measurements in the last chapter were studied through PSS with the addition of diffusion process simulation of charge carriers in the Transition Layer. An A/E distribution was obtained that shows the Transition Layer effect to be the origin of the low energy tail, validating the methods used for the FCCD determination. In the future, PSS will provide an estimate of the PSD efficiencies, $0\nu\beta\beta$ signal efficiency in comparison to the $^{208}$Tl DEP, help judge the data processing impact, and assist future detectors development.

# Chapter 6

# Production and Characterisation of Low Neutron Emission $^{228}$Th Calibration Sources

In GERDA, energy calibrations are performed with the insertion of three $^{228}$Th-sources alongside the germanium detector strings to monitor the energy resolution and ensure the stability of the energy scale for the measurements. This chapter describes the production and the characterisation of new low neutron emission $^{228}$Th sources to be employed as the new primary calibration sources inside the GERDA experiment. All the necessary production steps for their creation and their low neutron emission quality are described in detail in Section 6.1. The subsequent characterisation is explained in Section 6.2. The $\gamma$-activity measurements of the sources with the low background germanium detector counting facility Gator are described in Section 6.2.1.1, while the Gator MC simulations and the activity results are reported in Section 6.2.1.1. The precise knowledge of the activities is essential for the scaling of calibration MC simulations of the GERDA array to calibration measurements to judge the quality of the GERDA background model and the PSD efficiencies of the Full Energy Peak (FEP) and the Double Escape Peak (DEP). The neutron emission measurements and results are presented in Section 6.2, as well.

# 6.1   Production of $^{228}$Th Calibration Sources

Due to the 1.9 yr half-life of $^{228}$Th, the original GERDA Phase II calibration sources produced in 2014 had to be replaced [99]. For this purpose, the production of four new $^{228}$Th sources exhibiting low neutron emission was organised. In the $^{228}$Th decay chain, several $\alpha$-particles of energies of 8.8 MeV and below are emitted, inducing ($\alpha$, n)-reactions in commercially available $^{228}$Th sources. If the germanium detectors of GERDA were to be exposed to the resulting neutrons during calibration, $^{77}$Ge and its metastable state $^{77m}$Ge would be created through neutron activation. With the $^{77}$Ge $\gamma$-lines at 2000 keV, 2038 keV, and 2077 keV so close to $Q_{\beta\beta}$ and a half-life of only 11 hours, it was calculated in a past work [61] that this would pose a problematic irreducible background to the experiment [63]. For this purpose, a technique, developed by the University of Zurich (UZH) and Paul Scherrer Institute (PSI), was employed that makes use of the deposition of the $^{228}$Th inside gold foils [100]. Gold features a ($\alpha$,n)-production energy threshold of 9.94 MeV, above the decay chain's $\alpha$-decay maximum energy of 8.8 MeV [61, 100]. The induced $^{77}$Ge background of the new sources is estimated in Section 6.2.2.

A schematic diagram of all the steps in the procedure to produce the custom low neutron emission $^{228}$Th calibration sources is given in Figure 6.1. First, ThCl$_4$
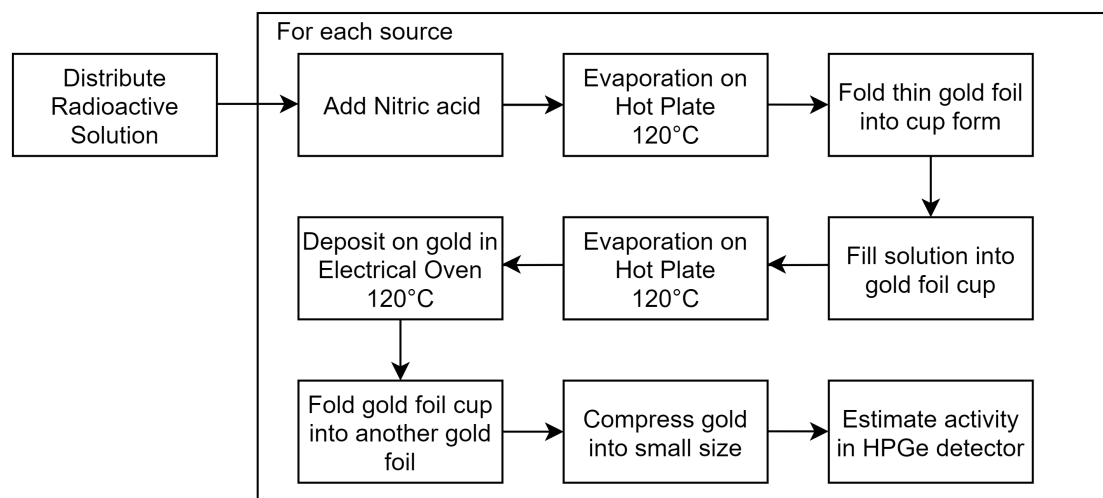


FIGURE 6.1: Schematic diagram on the low neutron emission custom low neutron emission $^{228}$Th calibration source production technique.

dissolved in HCl with a total activity of 153.1 kBq of $^{228}$Th had been delivered from the company Eckert & Ziegler to the University of Mainz, Germany. In

order to handle such high activities, the laboratories of the Nuclear Chemistry Insitute in Mainz were chosen as a production site. The sources were then produced from 18.–19. June 2018 as a collaboration between the University of Zürich, Paul Scherrer Institute (PSI), and the University of Mainz on location.

The required equipment for the production procedure included:

- Plexiglass glovebox with air filter system
- Pump with actived charcoal filter
- Hot plate with aluminum cover
- Electric oven capable of up to 800 °C
- Thermocouplings
- Clean utensils: tweezers, pincers
- Glass cutter
- PE pipettes
- Eppendorf pippette to divide the initial solution
- PTFE crucible with quartz filter paper as cover
- Nitric acid (HNO$_3$) concentrate
- H$_2$O destilled
- Geiger counter to monitor glovebox
- ThCl$_4$ dissolved in HCl with a total activity of around 153.1 kBq of $^{228}$Th
- 8× 20 μm thick, 4 cm$^2$ high purity gold foil squares

The source production itself took place in a glovebox, connected to an air filter to prevent $^{220}$Rn emanation during the heating processes. In order to deposit the $^{228}$Th onto the gold foils, several chemical reactions had to be initiated. Figure 6.2 shows four photos of the entire process.

In a first step, the solution of ThCl$_4$ dissolved in HCl with a total activity of 153.1 kBq of $^{228}$Th was weighed to be 5.1 g and distributed into three PTFE crucibles containg 1.25 g and a fourth one containing the rest. Nitric acid (HNO$_3$) was then added in and the solution was heated to 120 °C on a hot plate, evaporating the chlorine according to the reaction in Equation 6.1. The chlorine
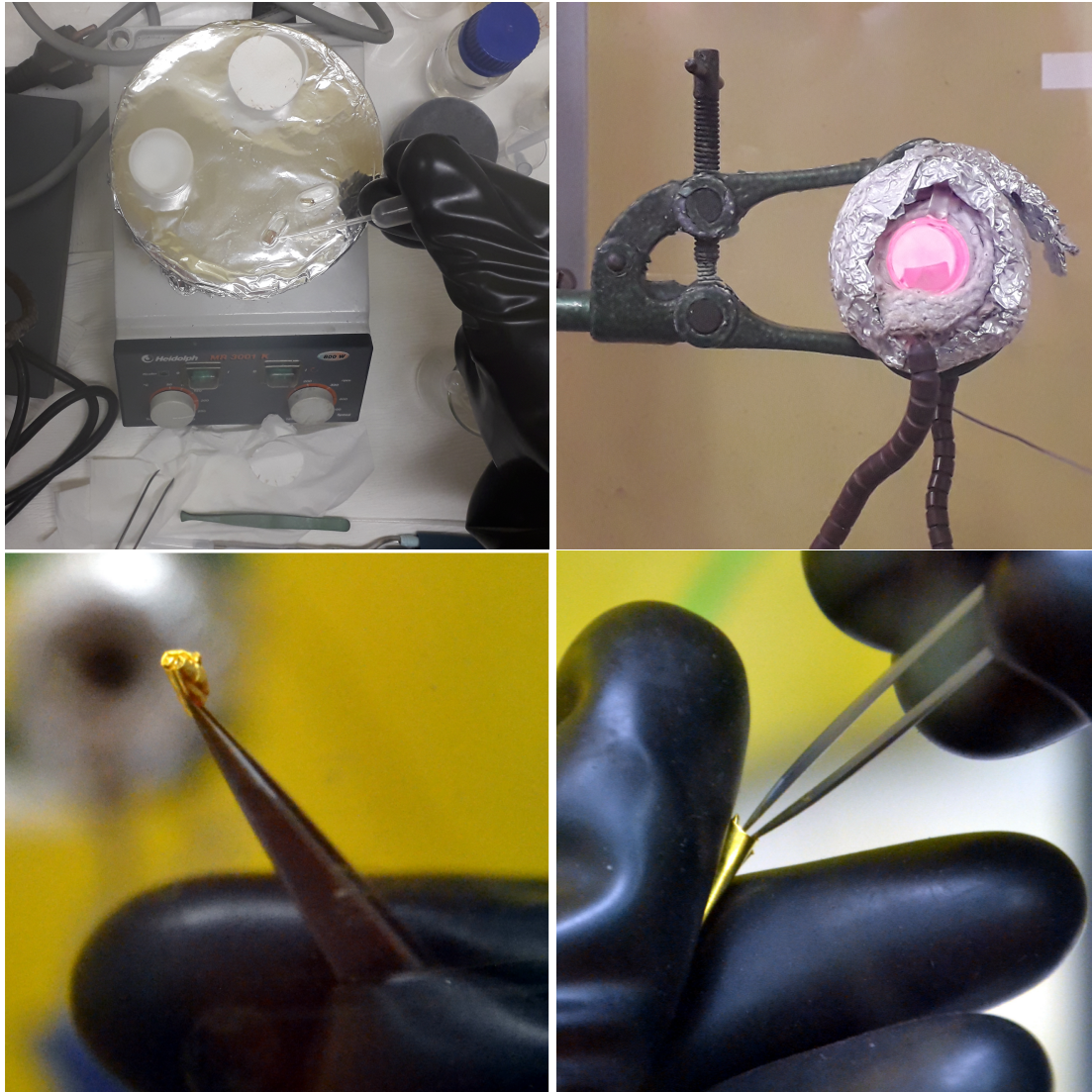
FIGURE 6.2: Source production: (Top left): Heating of the ThCl$_4$ in 1 M HCl solution in PTFE crucibles and subsequent pipetting of Th(NO3)$_4$ with nitric acid into gold cups created from gold foil squares. (Top right): Heating the filled gold cups to 800°C inside an electrical oven to evaporate the liquid and deposit the $^{228}$Th onto the gold surface. (Bottom left): Folding of the inner gold foil cup to contain $^{228}$Th inside. (Bottom right): Folding of gold foil around inner gold foil to reduce the neutron emission of the future calibration sources after encapsulation for the GERDA experiment. Bottom photos from [99].
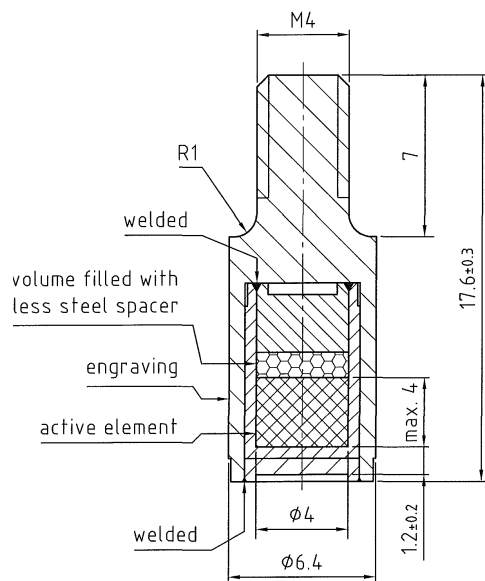
FIGURE 6.3: Schematic of the encapsulated $^{228}$Th calibration source for the GERDA experiment. The dimensions are in mm. Four sources were produced at the University of Mainz to serve as the active elements. Eckert & Ziegler then encapsulated the active elements according to the schematic. The M4 thread serves to screw the source into the source holder of the Source Insertion System (SIS).

was separated from the ThCl$_4$ molecules, because both $^{35}$Cl and $^{37}$Cl possess $(\alpha, n)$-production thresholds below 8.8 MeV.

$$3\text{ThCl}_4 + 16\text{HNO}_3 \longrightarrow [3\text{Th}(\text{NO}_3)_4]_{\text{solid}} + [4\text{NOCl} + 8\text{H}_2\text{O} + 4\text{Cl}_2]_{\text{gas}} \quad (6.1)$$

Four 20 µm thick, 4 cm$^2$ gold foil squares were cleaned with isopropyl and folded into small cups to accommodate in equal parts the Th(NO3)$_4$ mixed together with more nitric acid for better distribution. The gold cups were then each heated to 120 °C on a hot plate to evaporate the nitric acid and, in a second step, inserted into an electrical oven. Reaching 800 °C inside the oven, the Th(NO3)$_4$ reacted and deposited ThO$_2$ onto the gold foil, as shown in Equation 6.2.

$$3\text{Th}(\text{NO}_3)_4 \longrightarrow [3\text{ThO}_2]_{\text{solid}} + [12\text{NO}_2 + 3\text{O}_2]_{\text{gas}} \quad (6.2)$$
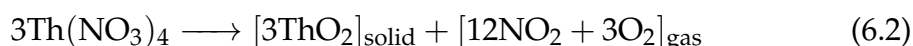
The individual gold cup was then taken out of the oven and folded inside of another gold foil down to a size of 4 mm × 4 mm × 4 mm in order to serve later as the active element of the source. The precise size of the active element was specified by Eckert & Ziegler as illustrated in the schematic of the encapsulated source in Figure 6.3. Achieving these dimensions through folding and strong

pressing proved arduous and demanded additional time and put strain on the material. In future productions of calibration sources, the space issue should be accounted for. During the production, a Geiger counter was employed to monitor the glovebox, glovebox walls, containers, and equipment as potential locations of activity losses. The workspace's detected total count rate counter rose throughout the production from $(0.1–0.2) \cdot 10^2 \, \text{s}^{-1}$ to $(0.6–0.8) \cdot 10^2 \, \text{s}^{-1}$, indicative of lost $^{228}$Th activity in the process.

Four sources were produced in total during the two days, distributing the initial 153.1 kBq of $^{228}$Th into sources with activities ranging anywhere between 10 to 40 kBq per source. The large uncertainty stems from an inevitable loss of activity in the production process and inherent uncertainty in distributing the initial solution into equal parts. A first estimation of the activity distribution was performed right after production with a HPGe detector in the laboratory in Mainz. The count rate of the 583 keV peak energy peak of each $^{228}$Th source was measured using an MCA over 5 min each, leading to the count rates listed in Table 6.1. The sources were thus not anticipated to have equally distributed activities in the later activity determination described in Section 6.2.

| Source | 583 keV count rate [s$^{-1}$] | Relative ratio |
|---|---|---|
| AM-2628 | $10.2 \pm 0.2$ | 1 |
| AM-2629 | $8.6 \pm 0.2$ | 0.84 |
| AM-2630 | $5.8 \pm 0.2$ | 0.57 |
| AM-2631 | $3.9 \pm 0.2$ | 0.38 |

TABLE 6.1: Count rates of the produced calibration sources measured with a HPGe detector in Mainz. This is a first estimation of the activity distribution. The source names were chosen at encapsulation time, but named here accordingly.

The sources were then packaged and sent to Eckert & Ziegler in Braunschweig, Germany, to be encapsulated inside double-sealed stainless steel capsules (VZ-3474-002). At location, the four encapsulated sources were certified for leak tightness at room temperatures with certified primary leak tests I and II according to ISO-2919.

Afterwards, the encapsulated sources were shipped to the Max Planck Institute for Nuclear Physics in Heidelberg, Germany. There, they were tested for leak tightness at cryogenic temperatures by the Radiation Protection Group through
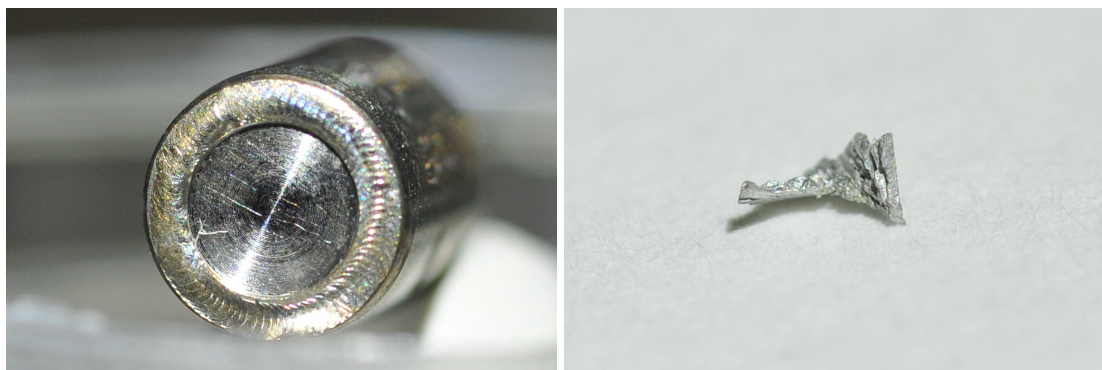
FIGURE 6.4: Cryogenic leakage tests at the Max Planck Institute for Nuclear Physics in Heidelberg, Germany, revealed the outer seal of one of the four sources (left) emitting part of the soldering (right) into the liquid nitrogen. The source was subsequently sent back to Eckert & Ziegler to be re-encapsulated. The other three sources passed all tests.

20 cycles of cooling in liquid nitrogen at 77 K and then warming up to room temperature. In the process, the outer seal of one of the four encapsulated sources, AM-2630, was found to emit part of the soldering into the liquid nitrogen, as shown in Figure 6.4. High performance wipe tests were performed with a detection limit of 0.02 Bq for $\alpha$-particles and 0.05 Bq for $\beta$-particles, leading with an assumed 10% wipe efficiency to a detection sensitivity of 0.2 Bq and 0.5 Bq for $\alpha$-particles and $\beta$-particles, respectively. Additionally, the $^{220}$Rn sensitive radon detector SARAD Thoron Scout [101] was used in a closed 20 l box, containing first the defect AM-2630 source, then all other sources to measure gaseous leaks. No contaminations or additional $^{220}$Rn was detected.

It was decided that even though the source itself was not compromised, the double-sealed safety was not upheld by this fourth source and needed to be checked by the manufacturer and eventually re-encapsulated. The fourth source was thus not measured in this work, but could find use in the LEGEND experiment in the future. The other three sources, AM-2629, AM-2629, and AM-2631, passed all the tests and received their certificates and were subsequently shipped to LNGS.

## 6.2 Characterisation of $^{228}$Th Calibration Sources

When the $^{228}$Th sources arrived at LNGS, they were characterised underground: $\gamma$-activity measurements were performed using the low background High Purity

Germanium (HPGe) detector facility Gator, described in Section 6.2.1, while for the neutron emission measurements a LiI(Eu) detector was employed, as reported in Section 6.2.2.

## 6.2.1  $\gamma$-Activity Measurements in Gator

Gator is a 2.2 kg High Purity Germanium (HPGe) crystal surrounded by low-activity copper, lead, and polyethylene, featuring an integral counting rate of only 9.6 events per hour in the 100-2700 keV energy region [102]. Coupled with its excellent energy resolution, it has proved to be ideally suited to determine the activities for component materials in the selection campaigns for XENON1T, XENONnT, GERDA, and LEGEND [41, 103, 104]. In the course of the characterisation of the new $^{228}$Th calibration sources for GERDA, Gator was employed to determine their $\gamma$-activity. Each source was separately measured for 1 hour, while located directly on the copper endcap of the cryostat above the HPGe, as depicted in Figure 6.5. The energy spectra were acquired with a dead time ranging between 12–24% depending on the source activity.

### 6.2.1.1  $\gamma$-Activity Simulation and Analysis

The Gator facility was previously modelled in Geant4, but altered in the frame of this work to include the accurate sources on top of the copper end cap, close to the detector with the cryostat and the lead castle surrounding them. For the source geometry, the dimensions of Figure 6.3 were implemented. Figure 6.6 illustrates the resulting complete Geant4 model as a wireframe visualisation render using VRML driver 2.0.

The plan was to set up the source volume to contain $^{228}$Th and let it run automatically through its decay chain. The initial Geant4 framework, used in the past for Gator, appeared to have problems in the *nucleusLimit* function, however. Investigating the cause lead to the finding that the function was unable to accurately account for different decay times and thus created artificial summation peaks not visible in data. The MC simulations were resimulated with decoupled simulations of the three primary components $^{208}$Tl, $^{212}$Bi, and $^{212}$Pb. Afterwards their spectra were weighted and combined relative to their branching ratios their
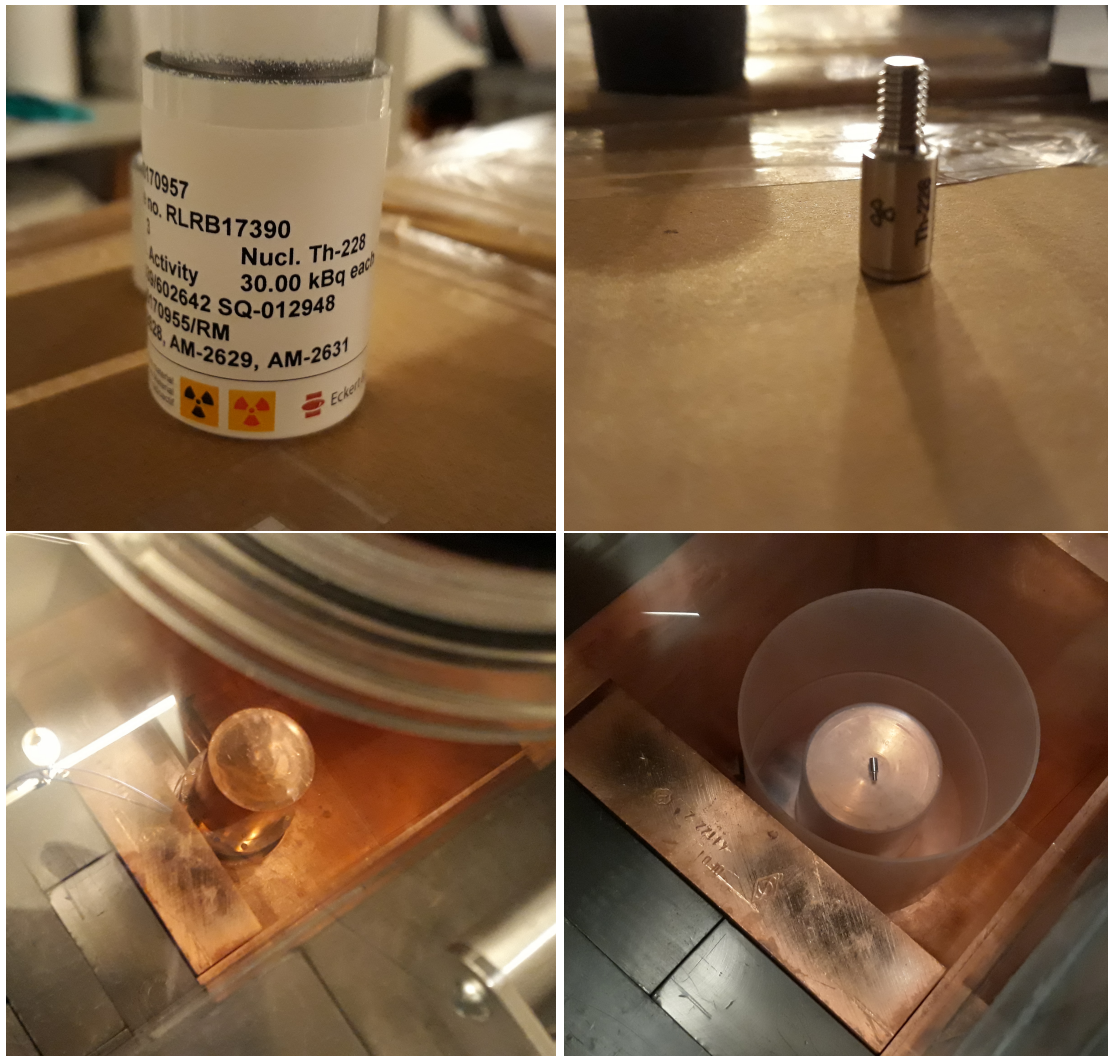
FIGURE 6.5: Source characterisation: (Top left): Lead container in which the sources AM-2628, AM-2629, AM-2631 were delivered underground in LNGS into the measurement facility. (Top right): Steel encapsulated $^{228}$Th sources with a M4 standardised screw to attach it later into the tantalum absorber of the source holder in the GERDA experiment. (Bottom left): Interior view onto the end cap of the of low background HPGe detector facility Gator at LNGS, surrounded by lead bricks to shield from background. (Bottom right): Measurement of each source on top of the copper endcap inside of Gator.
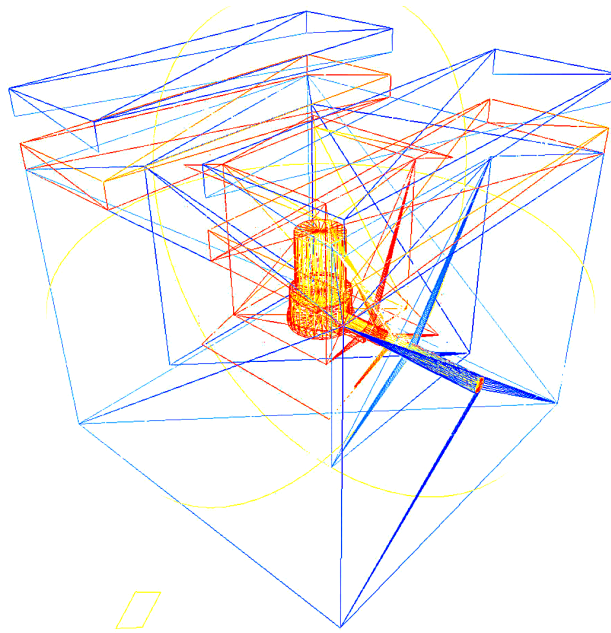
FIGURE 6.6: Geant4 simulation visualisation of the copper end cap above the Gator HPGe detector, and surrounded by the lead castle.

branching ratios and transient equilibrium corrections [63]. The problem with the artificial summation peaks was thereby solved.

Additionally, the spectra were smeared with Gator's energy resolution curve in Figure 4.8, obtained from calibration, given as

$$\Delta E\,(E) = \sqrt{p_0 + p_1 \cdot E + p_2 \cdot E^2}\,, \tag{6.3}$$

where the energy resolution $\Delta E$ at a certain energy $E$ is given as a function of $E$. The parameters are given in Table 6.2.
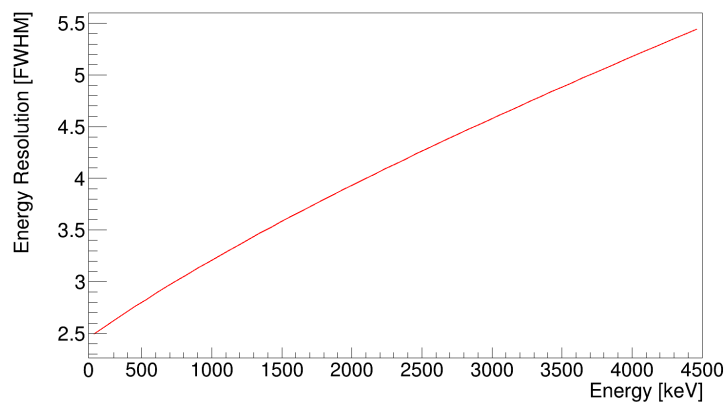


FIGURE 6.7: Gator resolution curve given by Equation 6.3 and Table 6.2 extracted from calibration.

| Parameters | Value |
|---|---|
| $p_0$ | $(6.04 \pm 0.33)$ keV$^2$ |
| $p_1$ | $(1.74 \pm 0.12) \cdot 10^{-3}$ keV |
| $p_2$ | $(2.32 \pm 0.74) \cdot 10^{-8}$ |

TABLE 6.2: Parameters of the Gator resolution curve used in Equation 6.3.

On an event by event basis, the event energies were adjusted according to

$$E_{final} = E_{initial} + \Delta E \, , \tag{6.4}$$

where E is the initial event energy, $\Delta E$ a number created by a random number generator constrained by the composition of a Gaussian function, centered around the origin with the FWHM from the resolution curve, and a low energy tail component with its parameters defined by the 2.6 MeV-line low energy tail parameters extracted from data.

An example of the simulated energy spectrum in comparison to the measured energy spectrum for source AM-2629 is shown in Figure 6.8.

By simulating $10^9$ events as a known quantity of $^{228}$Th decay, the activity of the sources can be determined by matching the spectra to data and calculating from the scaling factor how many decays accumulated in total during the measurement. By dividing then with the measurement duration, the nucleus decay rate and thus the activity is retrieved, according to Equation 6.5.

$$A^{^{228}Th} = \frac{N_{sim} \cdot f_{scale}}{t_{measurement}} \, , \tag{6.5}$$

where $A^{^{228}Th}$ is the activity of each $^{228}$Th source, $N_{sim}$ the total number of simulated events, $f_{scale}$ the scaling factor to match the spectra, and $t_{measurement}$ the total measurement time of that particular source.

Two methods were employed to scale the MC simulation spectra to the measured ones to retrieve the scaling factor $f_{scale}$ and cross-check their results:

- The first method used a $\chi^2$ minimisation of the bin content differences around the Compton edge at around 2380 keV.

(a) AM-2628
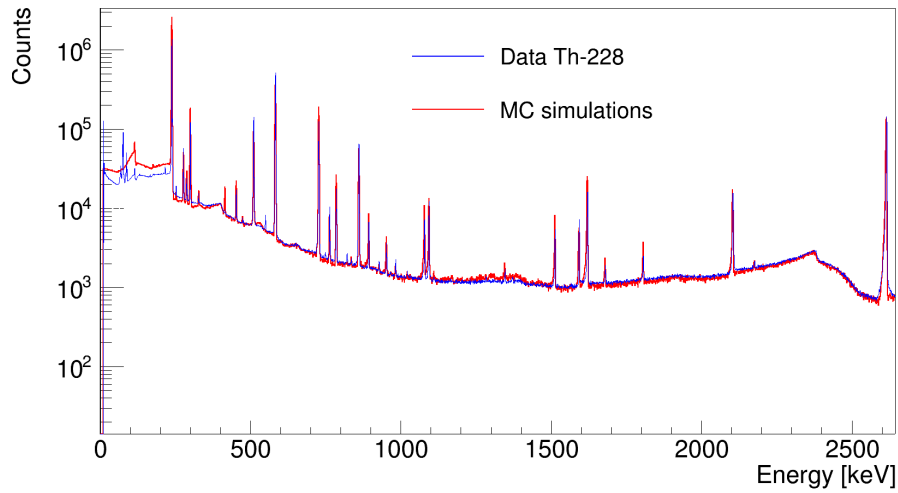


(b) AM-2629
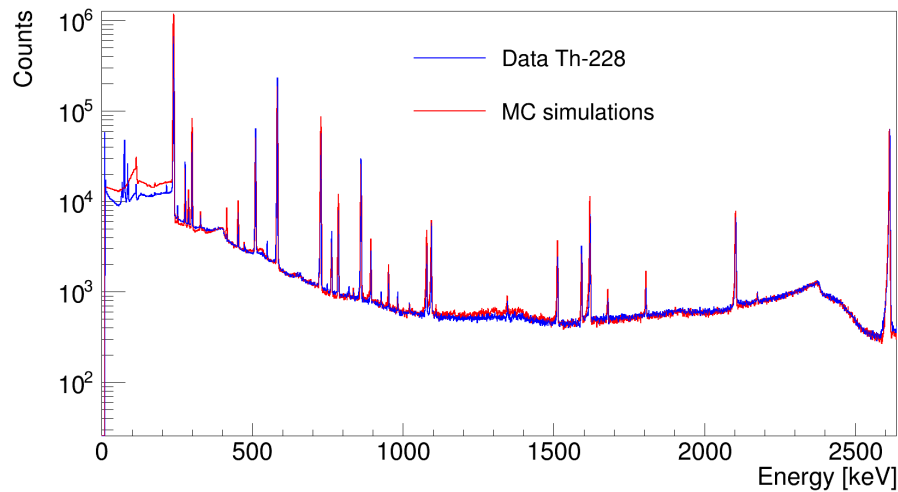


(c) AM-2631
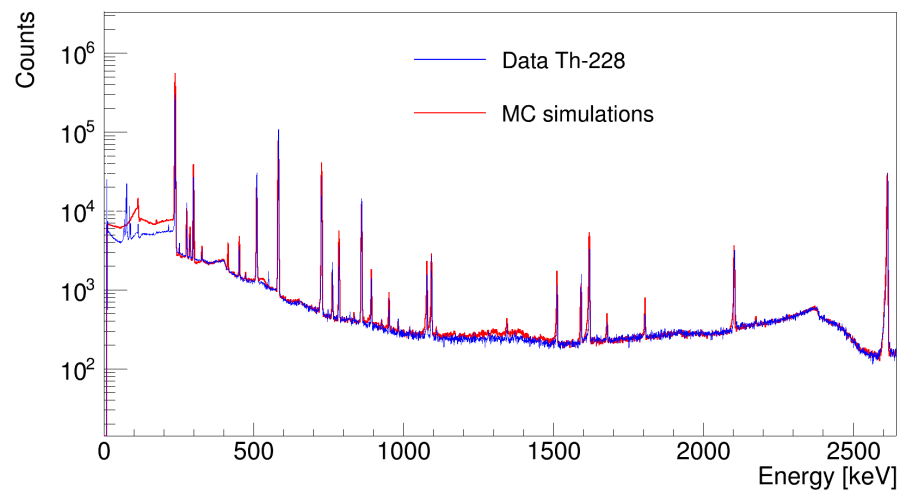


FIGURE 6.8: Energy spectra of the new $^{228}$Th calibration sources (blue) matched to simulations (red) to extract their $\gamma$-activity.

- The second method involved the fitting of the 2.6 MeV line in both spectra with a combination of a Gaussian function, a constant and linear background, a step function, and a low energy tail, as defined in Equation 6.6. The count rate of the 2.6 MeV line in the simulation spectrum was then scaled to the count rate of the measured 2.6 MeV line.

$$
\begin{aligned}
f(x)_{\text{Fit}} &= \frac{A_{\text{Gauss}}}{\sqrt{2\pi}\sigma}\exp\left(\frac{-(x-\mu_0)^2}{2\sigma^2}\right) \\
&+ \frac{B_{\text{Tail}}}{2C}\exp\left(\frac{x-\mu_0}{C}+\frac{D^2}{2C^2}\right)\cdot\text{erfc}\left(\frac{x-\mu_0}{\sqrt{2}D}+\frac{D}{\sqrt{2}C}\right) \\
&+ \frac{E_{\text{Step}}}{2}\text{erfc}\left(\frac{x-\mu_0}{\sqrt{2}\sigma}\right) \\
&+ F_{\text{Linear}}\cdot(x-\mu_0)+G_{\text{Constant}} ,
\end{aligned}
\tag{6.6}
$$

with $\mu_0$ as the mean and $\sigma$ as the standard deviation of the Gaussian function, and $A_{\text{Gauss}}, B_{\text{Tail}}, C, D, E_{\text{Step}}, F_{\text{Linear}}$, and $G_{\text{Constant}}$ as free fit parameters.

The statistical uncertainty was extracted from the best-fit uncertainty for the Compton edge $\chi^2$ method, while for the 2.6 MeV-line method a variation of the 2.6 MeV fit parameters with a Gaussian function was used. The Gaussian function has its mean located at the best fit parameter value and the fit parameter uncertainty was its FWHM. The solution space was mapped as a histogram with the resulting standard deviation of the distribution as the overall statistical uncertainty.

The systematic uncertainties were determined through MC resimulations with a 2 mm height variation, resulting in a +3.5%/-2.7% difference. A variation in the cross sections of the MC simulations gave rise to a -2%/+2.5% difference. An energy range variation of $\pm$ 20 keV resulted in +2.5% uncertainy across the board. Through error propagation, a total systematic uncertainty of +4.8%/-4.5% was estimated.

The two activity measurement methods had matching resulting activities and are listed in Table 6.3. The 2.6 MeV-line method activities were chosen as the main result due to the lower calculated uncertainty of the method.

To predict the activity of the uncharacterised source AM-2630, the relative ratios of the source activities were calculated to be $1 : 0.88 : X : 0.41$, standing for AM-2628 : AM-2629 : AM-2630 : AM-2631, with X the unknown source activity. The relative ratios were compared to the measurements in the laboratory in Mainz during production (in Table 6.1), where the ratios $1 : 0.84 : 0.57 : 0.38$ were found. This gave rise to the $(13 \pm 2)$ kBq activity prediction with a conservative estimated uncertainty for the uncharacterised source AM-2630.

| Source | Activity (Compton edge) [kBq] | Activity (2.6 MeV fit) [kBq] |
| --- | --- | --- |
| AM-2628 | $23.6 \pm 1.1$ (stat.) +1.1/-1.0 (sys.) | $23.4 \pm 0.9$ (stat.) +1.1/-1.0 (sys.) |
| AM-2629 | $20.8 \pm 1.1$ (stat.) +1.0/-0.9 (sys.) | $20.7 \pm 0.8$ (stat.) +1.0/-0.9 (sys.) |
| AM-2630 | | $\sim 13 \quad \pm 2$ (predicted) |
| AM-2631 | $10.1 \pm 0.9$ (stat.) +0.5/-0.4 (sys.) | $9.7 \pm 0.4$ (stat.) +0.5/-0.4 (sys.) |

TABLE 6.3: $\gamma$-activities of the produced $^{228}$Th sources determined in Gator with Compton edge $\chi^2$ minimisation (left) and 2.6 MeV-line (right) matched scaling. The activity of AM-2630 was predicted based on the relative ratios of the measurements in Mainz.

## 6.2.2   Neutron Emission Measurements in LiI(Eu) detector

To estimate the neutron flux emitted by the $^{228}$Th sources, a LiI(Eu) detector equipped with a custom low activity PMT was employed connected to an MCA underground at LNGS [61]. Even though the sources were produced to feature low neutron emission, to prevent $^{77}$Ge creation through neutron activation in the detectors, great care had to be taken to determine the actual neutron emission rate. Figure 6.9 illustrates the inner workings of the detector in a schematic.

The LiI(Eu) detector consists of a 96% $^6$Li crystal to help detect neutrons through the reaction:

$$^6\text{Li} + \text{n} \quad \rightarrow \quad ^7\text{Li}^* \quad \rightarrow \quad ^3\text{H} + \alpha + 4.78 \,\text{MeV} , \qquad (6.7)$$
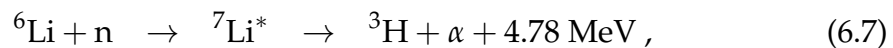
where the excess energy of 4.78 MeV, the Q-value of the reaction, is distributed between the $^3$H and the $\alpha$-particle. The heavy ions then induce scintillation light in the LiI(Eu) crystal. The emission consists of a broad band with a maximum at 470 nm. Due to their high ionizing power, quenching effects result in a reduced
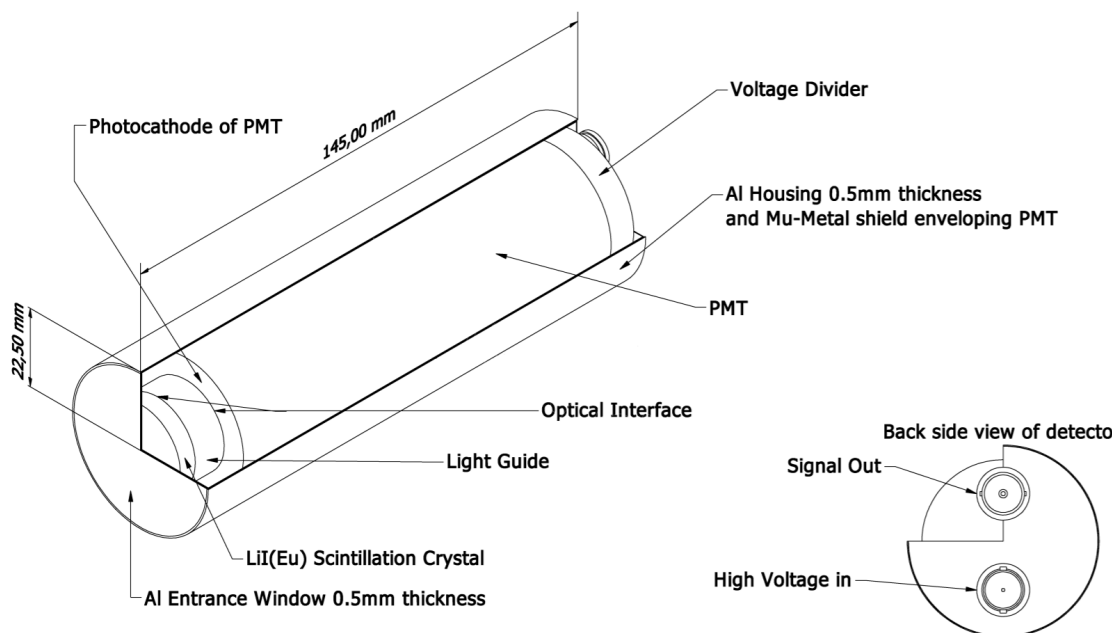
FIGURE 6.9: Schematic of the LiI(Eu) neutron detector. The $^6$Li interacts with neutrons, according to Equation 6.7, to create heavy ions such as $\alpha$-particles that induce scintillation light in the LiI(Eu) crystal that is detected by a 1 inch low activity PMT. Schematic from [105]

light output, shifting the thermal neutron peak to about 3.6–4.1 MeV equivalent $\gamma$-ray energy, still well resolved from the $\gamma$-contribution of background sources and the $^{228}$Th source itself, peaking at 2.6 MeV. The scintillation photons are detected by the low activity 1 inch PMT. Surrounding the detector, a 20 cm thick borated polyethylene shielding helps suppress background neutrons coming from the outside by moderating and absorbing them. Thermal neutrons are moderated with a 5 cm borated polyethylene barrier directly between the source and the detector. An adjacent 2 cm lead brick serves as $\gamma$-background reduction. The crystal itself is cylindrical in shape with a 1.3 cm radius and 0.3 cm length, encased in a copper ring for additional shielding. Figure 6.9 displays these parts in a photo of the LiI(Eu) detector inside the borated polyethylene shielding.

The neutron emission measurements of the $^{228}$Th sources using the LiI(Eu) detector were performed over 54 days underground at LNGS. Figure 6.11 compares the resulting spectrum to 314 days of background data without the sources. In addition, the data measured in 2014 is shown with 11 days of livetime and 142 days of background data. Both datasets exhibit a similar performance in terms of $\gamma$-activity portrayed up until around channel 650. The few events above that are characteristic for thermal neutrons, moderated in this setup with borated polyethylene blocks in front of the detector. Around channel 660, an internal

FIGURE 6.10: Photo of the LiI(Eu) neutron detector surrounded by borated polyethylene shield (white). From left to right: SHV high voltage and BNC signal out cables, aluminum housing containing the LiI(Eu) detector (silver), 5 cm polyethylene shielding (white), 2 cm lead brick, and source holder.

$\alpha$-particle contamination of the crystal is visible. The signal region was chosen to be the channel 700–950 range, above the contamination and including the thermal neutron signal peak around channel 800. The background data was taken over 314 days, shown in Figure 6.12 to be a stable neutron flux throughout, there was no evidence found beyond daily fluctuations.

After subtracting the background rate measured from the 314 days of background, the signal was taken in relation to the summed activity of the sources inside the detector. The neutron flux was then calculated as a counting experiment, according to Equation 6.8.

$$\Phi_n^{228\text{Th}} = \frac{R_n^{228\text{Th}} - R_n^{\text{bkg}}}{\epsilon \cdot \Sigma_i(A^{228\text{Th}})} \, , \tag{6.8}$$

with

$$R_n^{228\text{Th}} = \frac{N_n^{228\text{Th}}}{t^{228\text{Th}}} \, , \quad R_n^{\text{bkg}} = \frac{N_n^{\text{bkg}}}{t^{\text{bkg}}} , \tag{6.9}$$

where $N_n^{228\text{Th}}$, $t^{228\text{Th}}$, and $R_n^{228\text{Th}}$ are the total number of events, the measurement time, and the resulting event rate in the signal range for the $^{228}$Th measurements. $N_n^{\text{bkg}}$, $t^{\text{bkg}}$, and $R_n^{\text{bkg}}$ are the total number of events, the measurement time, and the resulting event rate in the signal range for the background measurements. The list of these parameter values is given in Table 6.4. The internal clock of

(a) New calibration sources



(b) Comparison with old calibration sources from 2014
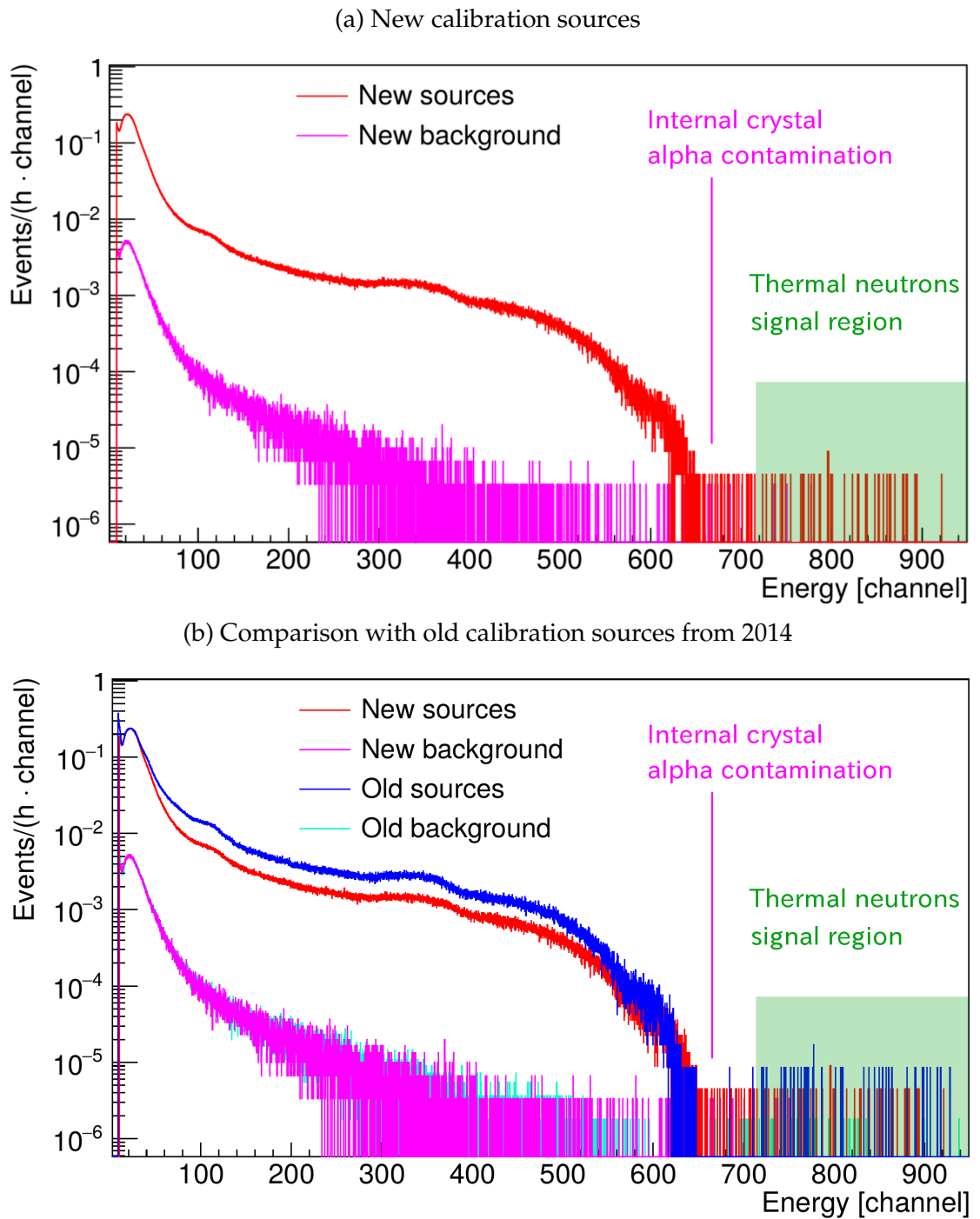


FIGURE 6.11: Normalised energy spectra of the LiI(Eu) detector depicting the newly produced sources (red) in comparison (bottom) to the old sources (blue) produced in 2014 (blue) for a livetime of 54 days and 11 days respectively. The corresponding background runs are almost identical for the new sources (magenta) during 314 days and the old sources (cyan) during 142 days respectively.
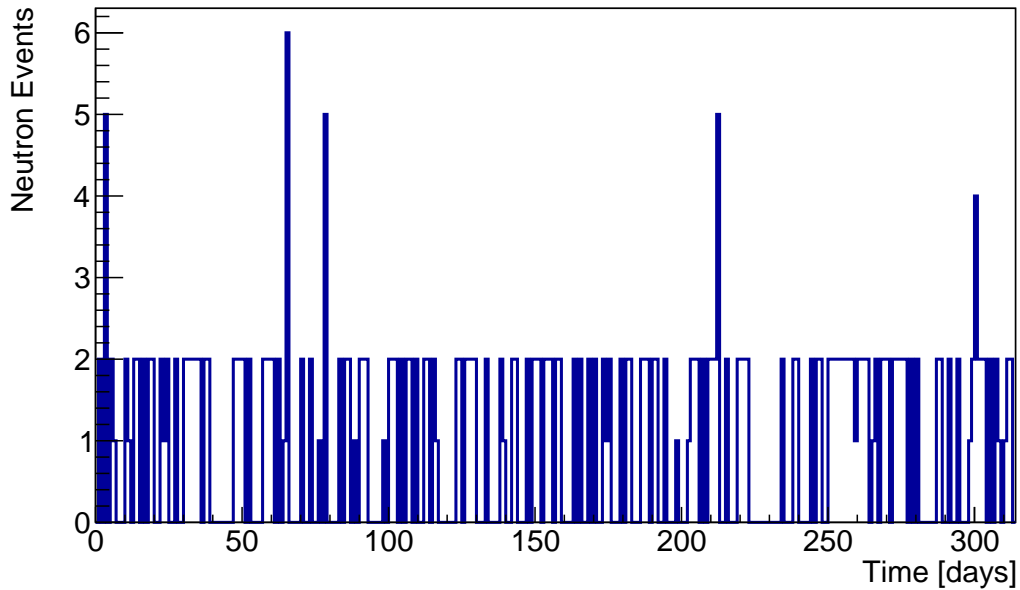
FIGURE 6.12: Background neutron events detected in the LiI(Eu) detector over 314 days of data taking without sources inside. A energy range of channel 700–950 was chosen to include events above the $\gamma$-background. The binning is 1 day per bin.

the MCA was used to measure the measurement time in the settings to directly save the event rates in the output files. $\epsilon$ is the total detection efficiency, and

| Parameters | 2018 Values | 2014 Values |
|---|---:|---:|
| $t^{228\text{Th}}$ | 54 days | 11 days |
| $t^{\text{bkg}}$ | 142 days | 314 days |
| $R_n^{228\text{Th}}$ | $(3.11 \pm 0.09) \cdot 10^{-5} \frac{n}{s}$ | $(6.68 \pm 0.43) \cdot 10^{-5} \frac{n}{s}$ |
| $R_n^{\text{bkg}}$ | $(0.88 \pm 0.11) \cdot 10^{-5} \frac{n}{s}$ | $(0.92 \pm 0.18) \cdot 10^{-5} \frac{n}{s}$ |
| $\Sigma_i(A^{228\text{Th}})$ | $(53.8^{+4.3}_{-4.0})$ kBq | $(130.4 \pm 5.5)$ kBq |

TABLE 6.4: Parameters for the calculation of the neutron flux used in Equation 6.8.

$\Sigma_i(A^{228\text{Th}})$ the sum of the source activities from Table 6.3. The total detection efficiency $\epsilon$ was estimated in the past from an AmBe measurement with the old sources to be [99, 106]

$$\epsilon = \left(5.32^{+0.18}_{-0.15} \pm 0.27\right) \cdot 10^{-4}. \tag{6.10}$$

The resulting combined neutron emission rate of the $^{228}$Th sources is listed in Table 6.5 and compared to the recalculated neutron activity from the 2014

data of the old sources with the same calculation method in good agreement with the new results. With about a five times higher measurement duration, a lower statistical uncertainty was achieved. The uncertainty on the efficiency in Equation 6.10 induced the systematic uncertainty on the emission rates.

| Sources | Duration | Rate [$10^{-7}\frac{n}{Bq \cdot s}$] |
|---|---|---|
| 2014 (orig.) | 11 days | $8.2 \pm 1.7$(stat.) $\pm 1.4$(sys.) [99] |
| 2014 (recalc.) | 11 days | $8.8 \pm 1.7$(stat.) $\pm 1.4$(sys.) |
| 2018 | 54 days | $7.8 \pm 0.5$(stat.) $\pm 1.1$(sys.) |

TABLE 6.5: Neutron emission rates comparison measured with the LiI(Eu) detector of the $^{228}$Th sources produced in 2018 and 2014 recalculated with the same method (bottom) and the original result (top) from [99].

This results in an order of magnitude lower neutron flux for these $^{228}$Th sources in comparison to a commercial source for which the neutron emission rate was measured in the past to be $7.5^{+2.5}_{-1.6} \cdot 10^{-6} \cdot \frac{n}{Bq \cdot s}$ [61, 99]. If commercial sources would be employed in GERDA, the emitted neutrons would generate $^{77}$Ge with background contributions in the region of interest, prior to PSD and LAr veto cuts, estimated in this previous analysis to be $2.97 \cdot 10^{-5}$ cts/(keV·kg·yr·kBq) [61]. This would amount to an induced background index when multiplying with the total activities of the new sources of $1.60^{+0.14}_{-0.13} \cdot 10^{-3}$ cts/(keV·kg·yr), which would be on the order of the background goal of GERDA Phase II. The order of magnitude lower neutron flux of the custom sources, however, reduces the otherwise problematic $^{77}$Ge background to a contribution to the background index of $10^{-4}$ cts/(keV·kg·yr) prior to analysis cuts, well below the background of GERDA Phase II. The neutron emission reduction of the custom sources was thus deemed a success and in January 2019 the new sources were installed as the main calibration sources for the GERDA experiment.

In the current planning, LEGEND-200 would employ a similar total amount of $^{228}$Th source activity for calibration, distributed among more sources. But due to the one order of magnitude lower background index goal of $10^{-4}$ cts/(keV·kg·yr) after LAr and PSD, this induced $^{77}$Ge background could possibly become a significant fraction of the background for LEGEND-200. This depends however greatly on the degree of background reduction achieved by the analysis cuts: In a separate study, conducted to measure the $^{77}$Ge background induced by cosmic muon interactions in GERDA, the combination of detector anti-coincidence,

PSD, LAr veto cuts reduced the spectral contribution of $^{77}$Ge at Q$_{\beta\beta}$ by an order of magnitude [107]. Active background reduction techniques could thus significantly suppress the $^{77}$Ge background index contribution down to $10^{-5}$ cts/(keV·kg·yr) and thus help achieve the desired background index for LEGEND-200.

### 6.2.3   Production & Characterisation Timeline

The full production cycle starting with first contacting the companies that could supply all the materials, until all the measurements were performed and the sources were installed in GERDA took two years. The primary reasons for the length were the intial delays to receive the quote from the Swiss liasion company Imatom for Eckert & Ziegler, the timing and scheduling to be able to work on a radioactive source involving several different institutions with their own schedules, and the bureaucratic complications that come with acquiring the rights to transporting radioactive materials. The detailed production timeline is given in Appendix C in Table C.1.

## 6.3   Conclusion and Outlook

The production of the four new $^{228}$Th calibration sources entailed the deposition of radioactive substance with 153.1 kBq of total activity of $^{228}$Th inside gold foils to be encapsulated into double-sealed stainless steel. The gold foil technique reduced the neutron emission of the sources by an order of magnitude in comparison to commercial sources, as demonstrated by LiI(Eu) measurements at LNGS. The activities of the sources were determined in the low background counting facility Gator to enable the scaling of calibration MC simulations of the GERDA array to calibration measurements. This allows for a better understanding of the GERDA background model and the estimation of the Full Energy Peak (FEP) and the Double Escape Peak (DEP) Pulse Shape Discrimination (PSD) efficiencies. The $^{228}$Th source were then installed into GERDA, serving as the main calibration sources for the germanium detectors of the experiment. The energy resolution estimation of the detectors for the final unblinding will be performed with calibration data gathered with these sources.

# Chapter 7

# Conclusion and Outlook

Neutrinoless double beta decay ($0\nu\beta\beta$) is a compelling avenue in modern physics to investigate the Majorana nature of the neutrino, the neutrino mass hierarchy, and the absolute mass scale. Searching for this decay, the GERDA experiment – based on an enriched germanium detector array directly submerged in a liquid argon cryostat – aims to achieve the lowest background and the highest sensitivity on the $0\nu\beta\beta$ decay half-life of $^{76}$Ge possible.

To achieve an ideal linear sensitivity scaling with exposure, the background index in the region of interest and the energy resolution must be optimised, while the active masses and thus exposure should be known to the best precision. The work in the scope of this thesis lead to advancement in all of these three key areas.

To help minimise the background, a background model for the natural non-enriched detectors, reaching much below the 565 keV main model threshold, was developed on the basis of a high quality natural detector dataset of 799 days of data. The natural detectors' order of magnitude lower $0\nu\beta\beta$ spectrum was thereby exploited to extract competitive $^{39}$Ar and $^{85}$Kr specific activity results and conduct a $^{214}$Bi $\gamma$-line study. The identification of the high voltage cables as the primary $^{214}$Bi background source location was performed as an input to the main background model.

Five germanium detectors of the new Inverted Coaxial (IC) type were characterised using $^{228}$Th and $^{241}$Am sources for the purpose of use in GERDA to gain

exposure and experience to employ them in large quantities in the next generation of $^{76}$Ge experiments, LEGEND. The Full Charge Collection Depths (FCCDs) of the detectors, describing the part of the n+ electrode wherein interactions induce no charge or only partial charge, were estimated with measurements of both source types. The Transition Layer simulations, that were used to achieve this, were verified through signal waveform pulse shape simulations, made possible through the development of a Pulse Shape Simulations framework. As a consequence of the FCCD results, the active volumina, active volume fractions, and active masses were determined.

Four new $^{228}$Th sources were produced to exhibit low neutron emission and to be used as calibration sources for the GERDA germanium detectors. The successful reduction of neutron emission of an order of magnitude in comparison to commercial sources was measured with a LiI(Eu) detector underground, showing that the neutron induced $^{77}$Ge background fulfil the background requirements of GERDA Phase II. The activities of the sources were determined inside the low background counting facility Gator, featuring a high purity germanium detector. The activities of the sources were determined in the low background counting facility Gator to enable calibration simulation scaling to calibration measurements to cross check the background model. After the characterisation of the $^{228}$Th sources, they were installed as the main calibration sources in GERDA.

In the final unblinding of GERDA experiment in 2020, the calibration data gathered with these sources will serve in the estimation of the energy resolution of the germanium detectors in the GERDA array. The exchange of the high voltage cables, the primary $^{214}$Bi emitters, in the latest upgrade of GERDA has the potential to improve the background index, while the active mass determination of the IC detectors will be used in the active exposure calculation of the IC detector dataset. LEGEND plans on using the produced sources as part of the primary calibration sources of the experiment and the characterised IC detectors will be employed in the search for the $0\nu\beta\beta$ decay.

# Appendix A

# Characterisation and Active Mass of IC Detectors
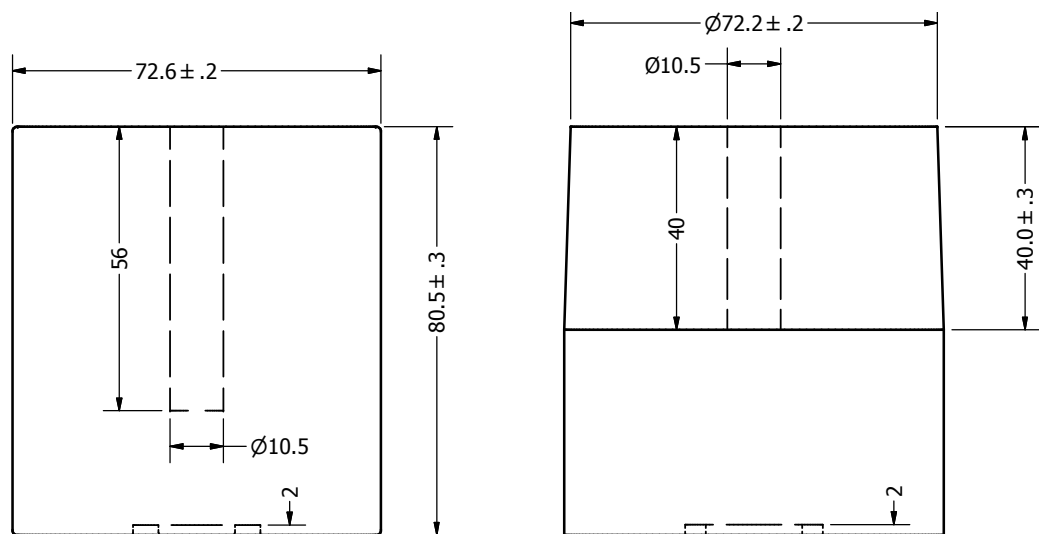


FIGURE A.1: Inverted coaxial (IC) detector schematics for IC48B (left) and IC50A (right) with precise dimensions and uncertainties, but varying for all detectors due to the imperfect nature of the crystal pulling process during production. The bored holes and grooves however are known to high precision. Note the tapered corners for IC50A. The dimensions are in mm.
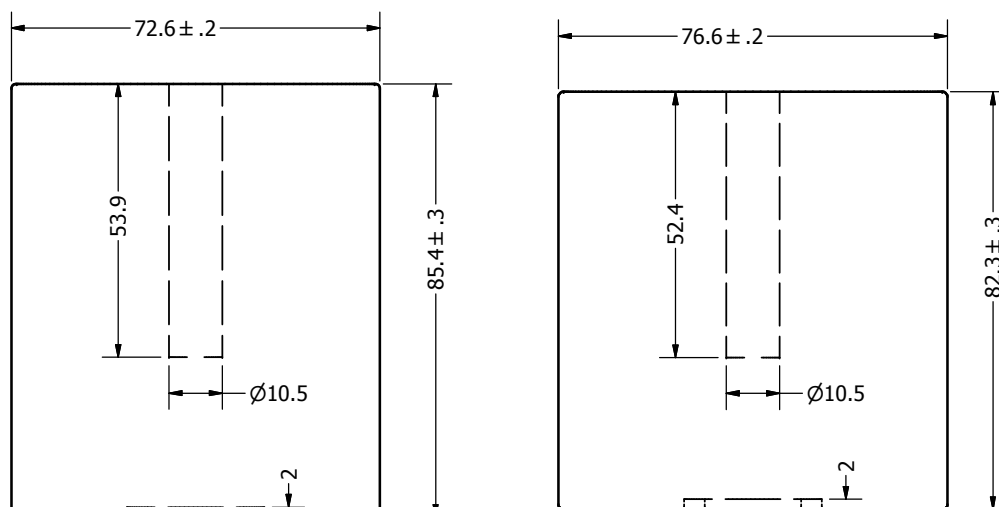
FIGURE A.2: Inverted coaxial (IC) detector schematics for IC50B (left) and IC74A (right) with precise dimensions and uncertainties, but varying for all detectors due to the imperfect nature of the crystal pulling process during production. The bored holes and grooves however are known to high precision. The dimensions are in mm.

# Appendix B

# Pulse Shape Simulation Framework

In the following is explained how Geoextractor operates as part of the PSS framework. Geoextractor loads the ROOT interpretable file as a TGeoManager Class Object and searches through the interlaced TGeoNodes and scans them for TGeoVolumes that match either natural or enriched germanium material definitions. The shape of these identified detector volumes and their position in absolute MaGe space is retrieved, accounting for programmed dead layer volumes, groove and point contact position, taper, and detector type. Consequently, Geoextractor is capable of autonomously searching through any geometry for GERDA or LEGEND.

Depending on the run options, shown in detail in Section B.1, Geoextractor creates the file output needed for the field simulations and is able to run the necessary libraries to generate the fields. Next, all the MaGe .ROOT files in the specified path are merged, the hit locations are transformed to the individual detector frames and then transferred to the charge carrier movement and charge induction libraries together with the energy deposition information. This can be done for all detectors in the .GDML file or for a detector subset with the detsettings option, ignoring hits in other detectors for better performance. Moreover, a new human-readable JavaScript Object Notation (JSON) based geometry description was developed to remove the definition redundancy when using all the programs in conjunction. MaGe was modified to replace the original matrix- and geometry-files and replace them with .JSON files, as described in Section B.1.

# B.1   Geoextractor Workflow

In the following, the general workflow of Geoextractor is described to connect MaGe simulations to the field and induction simulations of ADL and Siggen. The installation from github, from the repositories mmilor or mmpmu, in a directory of choice and the subsequent compile are run through the two commands

```
git clone git@github.com:mmilor/Geoextractor.git
cd Geoextractor
make
```

The working directory after installation already contains:

- The .GDML file *gdml.gdml*, suitable for GERDA Phase II, was created with the standard geometry- and matrix-files before the insertion of the IC detectors.

- The *detsettings.txt* file that contains additional information about the GERDA Phase II detectors. Any upgrade with addition channels, change of HV, etc., means that this file needs to be edited, but Geoextractor does not need to be recompiled.

The geometry and detector files for MaGe were changed to a new standardised .JSON formatting to be human-readable and consistent, e.g. for GD32C the part of the geometry-file is listed as

```
"42": {
"bulk-material": "EnrichedGe",
"cone": {
"height-mm": 5.5,
"position": "top",
"radius-mm": 30
},
"dead-layer": {
"bottom-thickness-nm": 910000,
"inner-thickness-nm": 590,
"material": "EnrichedGe",
"outer-thickness-nm": 910000,
"top-thickness-nm": 910000
},
```

```
"geometry -type ": 5,
"groove ": {
"depth -mm": 2,
"inner -radius -mm": 7.5,
"outer -radius -mm": 10.5,
"position ": "bottom "
},
"height -mm": 24.9,
"id": 42,
"name ": "GD32A",
"passivation -layer ": {
"material ": "EnrichedGe ",
"thickness -nm": 1000
},
"radius -mm": 33.13
}
```

The strings preceding the parameters are self-explanatory, including units, multiple parameters for the Dead Layer, and material. Only the strings *geometry type* is a reference to the Geant4 internally coded detector geometries. This is a big improvement from the original .dat files, which were exceedingly hard to edit. The positioning inside MaGe however still needs to be extracted and transformed with Geoextractor. The default MaGe input files are usually enough for the GERDA Phase II geometry. If a different arrangement of geometry- and matrix-file is desired, a new .GDML file can be produced by changing only three lines in *gdmlextractor.mac* to the desired new file names by

```
(...)
/MG/geometry/detector/geometryfile geometryfilename.json
/MG/geometry/detector/matrixfile matrixfilename.json
(...)
/MG/geometry/GDML/outputName extractedgdml
```

Then MaGe needs to be run with the macro. The edited *gdmlextractor.mac* file can, for example, be copied to the MaGe path and executed from there through

```
cd /path/to/MaGe
./MaGe gdmlextractor.mac
```

This produces, depending on how the macro was edited, the file *extractedgdml.gdml* in the MaGe folder. Geoextractor can link to the .gdml file with the

command: -g, –gdml PATH. Another possibility is to rename the default file in the Geoextractor folder and copy and rename your new .GDML file to *defaultg-dml.gdml* to automatically use this file without needing any options. Geoextractor can be run not only as a compiled standalone, but also directly as a CINT ROOT program. This helps in visually checking the .GDML file by using ROOT CINT with a BASH terminal and the command

```
root Geoextractor.cxx+(1)
```

An example of the visualisation of an extracted .GDML file is depicted in Figure 5.2. To use CINT also for the transformations, the shell variable $MC_DIR should be set to the directory of the .ROOT files, produced in MaGe, from which the hits should be extracted. This is done by

```
cd /path/to/MCSimulations
export MC_DIR=$(pwd)
cd /path/to/Geoextractor
```

It should be kept in mind that the files need to be simulated in MaGe with the same set of detector- and matrix-file configuration as the .GDML file itself. When in the Geoextractor directory, the program will be executed by simply evoking

```
root Geoextractor.cxx
```

In this configuration, Geoextractor will use default options and input files.

In compiled standalone mode, the options when running Geoextractor are as follows:

- -m, --mcdir PATH: Specify input path for ROOT files to be merged and used for extraction. Default: $MC_DIR shell variable.

- -a, --adl PATH: Specify output path for ADL files. Default: ./Output/adl

- -s, --siggen PATH: Specify output path for Siggen files. Default: ./Output/siggen

- -j, --json PATH: Specify output path for JSON files. Default: ./Output/json

- -f, --fields PATH: Specify output path for simulated fields with -a or -s specified library. Default: ./Output/fields

- -g, --gdml PATH: Specify path to GDML file. Default: ./defaultgdml.gdml

- -d, --detsettings PATH: Specify path to Detector Settings file. Default: ./detsettings.txt

- -x, --maxhits INT: Limit amount of hits per detector to be extracted and written to file to a fixed number. Default: no limit.

- -v, --vishits STRING: Visualise hit extraction with condition set by STRING. Example to show only events in detector 33: --v hits_iddet==33

- -n, --nohits: Skip all hit extraction, only extract geometry.

- -c, --checkgdml: Visualise .GDML file with OGL drivers. Best to use: root Geoextractor.cxx+(1)

- -h, --help: Show help message.

To extract only the geometries without any hits, use the command:

```
./Geoextractor --nohits
```

In order to extract hits out of .ROOT files, the directory of the files needs to be specified with either of the two options in order of priority:

- Via option: -m,--mcdir PATH
- Via shell variable $MC_DIR pointing to the directory

Using Geoextractor in conjunction with ADL 4 then allows the production of Tier1 output files. After downloading and installing ADL 4 through

```
git clone git@github.com:mppmu/ADL4.git
cd ADL4
make
```

Pulses are simulated after the necessary field simulations through Geoextractor by using

```
./SimulatePulse
```

This loops 1000 events, producing Tier1 output file of simulated pulse shapes. The Tier1 output can be run through the identical analysis chain as the data. Then the commands to start GELATIO to produce Tier2 files is as follows

```
sh LaunchExecModuleIni.sh Tier1.root
```

The workflow can then be enhanced through job scripts in the ADL4 folder to produce automatically a large quantity of PSS Tier1 files.

# B.2 ADL

The AGATA Detector simulation Library (ADL) is an existing software that was adapted for GERDA as ADL 3 [93].The program itself is C based and comprised of a library part capable to compute electric and weighting potentials, as well as electric fields for a specific detector geometry save them to .pa files. This dedicated file format stores the fields numerically in a gridsize up to a specified granularity. In the frame of this work, a gridsize of 0.01 mm was used consistently.

# Appendix C

# Production Timeline of the $^{228}$Th Calibration Sources

The Timeline of the full production organisation is given in the Table starting from the next page.

| Date | Event |
|---|---|
| March 2017 | Start to contact Eckert & Ziegler directly. Responsible person travelling for business. |
| March 2017 | Asked meteorological institute for leak test quote. Received it two weeks later. |
| April 2017 | E&Z claims they are only allowed to deal through Imatom with Swiss customers. |
| April 2017 | Promise of Imatom to send quote. |
| May 2017 | Imatom claim there are even more new legal conditions by E&Z, so it will take them even more time for the quote. |
| June 2017 | Imatom have finished the legalities and want some additional details of the source logistics route. |
| July 2017 | Imatom sends the first quote |
| July 2017 | Contacted Dr. Klaus Eberhardt from Mainz and Dr. Robert Eichler from PSI for source production work. Agreement and details being worked out. |
| August 2017 | Additional details need to be worked out which need to be added to the Imatom quote. |
| September 2017 | Gold foil arrives in Mainz. |
| September 2017 | E&Z prepare legal documents. Signing of several of them. |
| October 2017 | E&Z wants legal documents changed. |
| October 2017 | Asked Giovanni what took longest in last source production in order to accelerate current source production by removing possible bottlenecks. Meteorological institute turned out to take a very long time. |
| November 2017 | During GERDA meeting, discussion with Bernhard if sources could be tested in Heidelberg instead of meteorological institute to accelerate source production. Come to agreement that it is possible and accepted by LNGS. |
| November 2017 | Contact E&Z about changing of logistics route. Imatom has to change quote. |
| November 2017 | E&Z want even more legal documents not previously announced and change of receiving person specifically in Italy. Turns out in discussion involving Matthias Laubenstein as well, that it really needs to be the director of LNGS. |
| December 2017 - January 2018 | Organisation of these signatures and documents of the LNGS director and other responsible people by Matthias Laubenstein. |

| Date | Event |
|---|---|
| February 2018 | E&Z writes they are satisfied and start producing the Th solution. |
| February 2018 | Organisation of Heidelberg testing with Bernhard und Jochen Schreiner after encapsulation. |
| March 2018 | Confirmation that Heidelberg tests can be done and that paperwork is finished. |
| March 2018 | E&Z write they have produced the Th solution and can send it to Mainz. |
| June 2018 | First opportunity after solution arrival that worked for Dr. Robert Eichler and Dr. Klaus Eberhardt to be able to have facility space, facility availability and both can be present to work on the Th deposition in the gold foil. |
| 19. June 2018 | Finished work on gold foil deposition. Wrote E&Z that they can transport it to Braunschweig for encapsulation. |
| 26. Juli 2018 | E&Z finish encapsulation |
| 31. Juli 2018 | E&Z send encapsulated sources to Heidelberg |
| 01. August 2018 | Arrival of the encapsulated surces in Heidelberg |
| 03. August 2018 | Holiday season at MPIK Heidelberg; Tests delayed until September |
| 17. September 2018 | Jochen Schreiner starts with the Tests; due to high security measures estimates 3 weeks necessary |
| 3. October 2018 | Jochen Schreiner has finished the tests: 1 source failed the test due to welding |
| 3. October 2018 | Organisation with E&Z to retrieve the sources from MPIK and send 3 to LNGS, 1 to E&Z |
| October 2018 | Further documentation needed by E&Z for transportation |
| 8. November 2018 | 3 sources arrive at LNGS with Matthias Laubenstein |
| 14. November 2018 | Paperwork in person at LNGS to register source and transport sources underground |
| 15.-20. November 2018 | Underground work with sources in Gator: Gator activity measurements and LiI measurements |
| 16.-18. January 2019 | Installation of new sources into GERDA |

TABLE C.2: Timeline for the production and characterisation of the $^{228}$Th calibration sources for GERDA.

# *Acknowledgements*

I would like to express my gratitude to Prof. Dr. Laura Baudis for her guidance and help through her expertise, as well as the opportunity to be part of her group and a member of GERDA and LEGEND. At every step of the way I was surrounded by curious and forward looking minds everywhere. I've gained so much knowledge and experience, met and worked together with so many great people I feel blessed to call my friends.

I would like to give special thanks to Dr. Robert Eichler and Dr. Klaus Eberhardt for their help in the production of the $^{228}$Th calibration sources and for making it such a fun experience.

And finally, my amazing family and my wonderful wife for always encouraging and believing in me.

# List of Figures

# List of Tables

# Bibliography

[1] W. Pauli, *Niels Bohr and the Development of Physic*. McGraw-Hill, New York, 1955.

[2] C. L. Bennett et al., *Nine-year Wilkinson Microwave Anisotropy Probe (WMAP) Observations: Final Maps and Results*. The Astrophysical Journal Supplement Series, 208(2):20, 2013, URL http://stacks.iop.org/0067-0049/208/i=2/a=20.

[3] S. Davidson, E. Nardi, and Y. Nir, *Leptogenesis*. Physics Reports, 466(4-5):105–177, 2008, URL http://www.sciencedirect.com/science/article/pii/S0370157308001889.

[4] E. Majorana, *Teoria simmetrica dell'elettrone e del positrone*. Il Nuovo Cimento (1924-1942), 14(4):171–184, 1937, URL http://dx.doi.org/10.1007/BF02961314.

[5] M. Gonzalez-Garcia and M. Yokoyama, *Particle Data Group Review: Neutrino Mass, Mixing, and Oscillations*. Particle Data Group RPP 2018, 2018.

[6] The GERDA Collaboration, *The GERDA experiment for the search of $0\nu\beta\beta$ decay in $^{76}Ge$*. European Physical Journal C, 73:2330, Mar. 2013, 1212.4067.

[7] K. T. Knöpfle (GERDA), *Upgrade of the GERDA experiment*. PoS, TIPP2014:109, 2014.

[8] J. Schechter and J. W. F. Valle, *Neutrinoless double-$\beta$ decay in SU(2)× U(1) theories*. Phys. Rev. D, 25:2951–2954, Jun 1982, URL http://link.aps.org/doi/10.1103/PhysRevD.25.2951.

[9] M. Thomson, *Modern Particle Physics*. Cambridge University Press, New York, 2013.

[10] D. Galbraith and C. Burgard, *Standard Model of Particle Physics*. CERN, Webfest, 2012.

[11] H. Becquerel, *On the invisible rays emitted by phosphorescent bodies*. Comptes Rendus, 122:420, 1896.

[12] E. Rutherford, *Uranium radiation and the electrical conduction produced by it*. Phylos. Mag., 47:109–163, 1899.

[13] W. Pauli, *Brief an die Gruppe der Radioaktiven*. ETH, Zürich, 1930.

[14] E. J. Konopinski and H. M. Mahmoud, *The Universal Fermi Interaction*. Physical Review, 92:1045–1049, 1953.

[15] B. Pontecorvo, *Inverse beta processes and non-conservation of lepton charge*. ZETF, 34:172–173, 1958.

[16] F. Reines and C. L. Cowan, *Detection of the free neutrino*. Phys. Rev., 92:830–831, 1953.

[17] C. S. Wu et al., *Experimental Test of Parity Conservation in Beta Decay*. Physical Review, 105:1413–1415, Feb. 1957.

[18] M. Goldhaber et al., *Helicity of Neutrinos*. Phys. Rev., 109:1015–1017, Feb 1958, URL http://link.aps.org/doi/10.1103/PhysRev.109.1015.

[19] Y. Fukuda et al., *Evidence for Oscillation of Atmospheric Neutrinos*. Physical Review Letters, 81:1562–1567, Aug. 1998, hep-ex/9807003.

[20] Q. R. Ahmad et al., *Measurement of the Rate of Solar Neutrinos at the Sudbury Neutrino Observatory*. Physical Review Letters, 87(7):071301, Aug. 2001, nucl-ex/0106015.

[21] Z. Maki, M. Nakagawa, and S. Sakata, *Remarks on the Unified Model of Elementary Particles*. Progress of Theoretical Physics, 28(5):870–880, 1962.

[22] N. Cabibbo, *Unitary Symmetry and Leptonic Decays*. Physical Review Letters, 10:531–533, Jun. 1963.

[23] M. Kobayashi and T. Maskawa, *CP-Violation in the Renormalizable Theory of Weak Interaction*. Progress of Theoretical Physics, 49(2):652–657, 1973, URL http://ptp.oxfordjournals.org/content/49/2/652.abstract.

[24] C. Giunti and C. W. Kim, *Fundamentals of Neutrino Physics and Astrophysics*. Oxford University Press, GB, 2012.

[25] The T2K Collaboration, *Recent T2K Neutrino Oscillation Results*. TAUP Proceedings, TAUP 2019, 2019.

[26] M. Agostini, G. Benato, and J. A. Detwiler, *Discovery probability of next-generation neutrinoless double-β decay experiments*. Phys. Rev. D, 96:053001, Sep 2017, URL https://link.aps.org/doi/10.1103/PhysRevD.96.053001.

[27] I. Esteban et al., *NuFit 2017*. JHEP, 087, 2017.

[28] J. Engel and J. Mendez, *Status and Future of Nuclear Matrix Elements for Neutrinoless Double-Beta Decay: A Review*. Rept. Prog. Phys., 80(4):046301, 2017, 1610.06548.

[29] L. Baudis and A. Kish, *Dark matter candidates*. Experimental Astroparticle Physics Lectures, University of Zürich, 2015.

[30] N. Serra and O. Steinkamp, *Right-handed neutrinos*. Flavour Physics Lectures, University of Zürich, 2014.

[31] P. Higgs, *Broken symmetries, massless particles and gauge fields*. Physics Letters, 132–133, 1964.

[32] M. Fukugita and T. Yanagida, *Baryogenesis without Grand Unification*. Physics Letters B, 174(1):45 − 47, 1986, URL \color{blue}{http://www.sciencedirect.com/science/article/pii/0370269386911263}.

[33] M. Agostini et al., *Results on double beta decay with emission of two neutrinos or Majorons in $^{76}$Ge from GERDA Phase I*. The European Physical Journal C, 75(9):416, 2015, URL http://dx.doi.org/10.1140/epjc/s10052-015-3627-y.

[34] J. Kotila and F. Iachello, *Phase space factors for double-β decay*. Phys. Rev., C85:034316, 2012, 1209.5722.

[35] J. Barea, J. Kotila, and F. Iachello, *0νββ and 2νββ nuclear matrix elements in the interacting boson model with isospin restoration*. Phys. Rev. C, 91:034304, Mar 2015, URL http://link.aps.org/doi/10.1103/PhysRevC.91.034304.

[36] J. Albert et al., *Search for Neutrinoless Double-Beta Decay with the Complete EXO-200 Dataset*. Phys. Rev. Lett., 123(161802), 2019.

[37] A. Gando et al., *Search for Majorana Neutrinos near the Inverted Mass Hierarchy Region with KamLAND-Zen*. Phys. Rev. Lett., 117(082503), 2018.

[38] O. Azzolini et al., *Final result of CUPID-0 phase-I in the search for the Se-82 Neutrinoless Double Beta Decay*. Phys. Rev. Lett., 120(232502), 2018.

[39] C. Alduino et al., *First Results from CUORE: A Search for Lepton Number Violation via Neutrinoless Double Beta Decay of Te-130*. Phys. Rev. Lett., 120(232502), 2018.

[40] V. Guiseppe et al., *New results from the MAJORANA Demonstrator*. XXVIII Int. Conf. Neutrino Physics and Astrophysics, Heidelberg, Germany, 2018.

[41] LEGEND Collaboration et al., *The Large Enriched Germanium Experiment for Neutrinoless Double Beta Decay (LEGEND)*. AIP Conference Proceedings, 1894(1):020027, 09 2017, https://aip.scitation.org/doi/pdf/10.1063/1.5007652.

[42] The GERDA Collaboration et al. (GERDA), *Upgrade for Phase II of the Gerda experiment*. Eur. Phys. J., C78(5):388, 2018, 1711.01452.

[43] The GERDA Collaboration, *The background in the neutrinoless double beta experiment GERDA*. European Physical Journal C, 74(4):2764, 2014, 1306.5084.

[44] The GERDA Collaboration, *Results on Neutrinoless Double-$\beta$ Decay of $^{76}$Ge from Phase I of the GERDA Experiment*. Phys. Rev. Lett., 111:122503, Sep 2013, URL http://link.aps.org/doi/10.1103/PhysRevLett.111.122503.

[45] The GERDA Collaboration et al., *Background-free search for neutrinoless double-$\beta$ decay of $^{76}$Ge with GERDA*. Nature, 544:47, 2017, 1703.00570.

[46] The GERDA Collaboration et al. (GERDA), *Improved Limit on Neutrinoless Double-$\beta$ Decay of $^{76}$Ge from GERDA Phase II*. Phys. Rev. Lett., 120(13):132503, 2018, 1803.11100.

[47] M. Günther et al., *Heidelberg-Moscow $\beta\beta$ experiment with $^{76}$Ge: Full setup with five detectors*. Phys. Rev. D, 55:54–67, Jan 1997, URL https://link.aps.org/doi/10.1103/PhysRevD.55.54.

[48] C. E. Aalseth et al., *Recent results of the IGEX 76Ge double-beta decay experiment*. Physics of Atomic Nuclei, 63(7):1225–1228, Jul 2000, URL https://doi.org/10.1134/1.855774.

[49] M. The GERDA Collaboration, Agostini et al., *Probing Majorana neutrinos with double beta decay*. Science, 365(6460):1445–1448, 2019, https://science.sciencemag.org/content/365/6460/1445.full.pdf, URL https://science.sciencemag.org/content/365/6460/1445.

[50] The GERDA Collaboration et al., *GERDA results and the future perspectives for the neutrinoless double beta decay search using 76Ge*. International Journal of Modern Physics A, 33(09):1843004, 2018.

[51] Y. Akrami et al. (Planck), *Planck 2018 results. I. Overview and the cosmological legacy of Planck*. Planck, 2018, 1807.06205.

[52] E. Di Valentino, A. Melchiorri, and J. Silk, *Beyond six parameters: extending ΛCDM*. Phys. Rev., D92(12):121302, 2015, 1507.06646.

[53] J. Angrik et al., *KATRIN Design Report 2004*. FZKA Scientific Report, 7090, 2004, URL https://www.katrin.kit.edu/publikationen/DesignReport2004-12Jan2005.pdf.

[54] C. W. for the GERDA Collaboration, *Results and post-upgrade performance of GERDA Phase II*. TAUP 2019, Toyama, Japan, 2019.

[55] The LEGEND Collaboration, *The Large Enriched Germanium Experiment for Neutrinoless Double Beta Decay (LEGEND)*. TAUP Proceedings, TAUP 2017, 2017.

[56] G. Gilmore, *Practical Gamma-ray Spectrometry, 2nd Edition*. Wiley, UK, 2008.

[57] G. Douysset, T. Fritioff, C. Carlberg, I. Bergstrom, and M. Bjorkhage, *Determination of the Ge-76 double beta decay Q value*. Phys. Rev. Lett., 86:4259–4262, 2001.

[58] M. Agostini et al., *Signal modeling of high-purity Ge detectors with a small read-out electrode and application to neutrinoless double beta decay search in Ge-76*. Journal of Instrumentation, 6(03):P03005, 2011, URL http://stacks.iop.org/1748-0221/6/i=03/a=P03005.

[59] M. Berger et al., *ESTAR – Stopping-Power and Range Tables for Electrons*. NIST Standard Reference Database 124, 2005, URL http://www.nist.gov/pml/data/star/index.cfm.

[60] M. Agostini et al., *Pulse shape discrimination for* GERDA *Phase I data*. European Physical Journal C, 73:2583, Oct. 2013, 1307.2610.

[61] M. Tarka, *Studies of Neutron Flux Suppression from a $\gamma$-ray Source and the* GERDA *Calibration System*. PhD Thesis, University of Zürich, 2012.

[62] F. Froborg, *Calibration of Phase I of the* GERDA *Double Beta Decay Experiment*. PhD Thesis, University of Zürich, 2012.

[63] The Lund/LBNL Nuclear Data Search, *Table of Radioactive Isotopes*. Lund/LBNL Nuclear Data Website, 1999, URL http://nucleardata.nuclear.lu.se/toi/.

[64] GERDA Collaboration et al., *Modeling of GERDA Phase II data*. submitted to JHEP, arXiv:1909.02522, Sep 2019, 1909.02522.

[65] M. Agostini et al., *LArGe - Active background suppression using argon scintillation for the GERDA $0\nu\beta\beta$-experiment*. ArXiv e-prints, Jan. 2015, 1501.05762.

[66] M. Walter, *Background Reduction Techniques for the* GERDA *experiment*. PhD Thesis, University of Zürich, 2015.

[67] The GERDA Collaboration, *Limits on uranium and thorium bulk content in Gerda Phase I detectors*. Astroparticle Physics Journal, 91:15–21, 2017.

[68] M. Bauer et al., *MaGe: a Monte Carlo framework for the Gerda and Majorana double beta decay experiments*. Journal of Physics: Conference Series, 39:362–362, may 2006, URL https://doi.org/10.1088%2F1742-6596%2F39%2F1%2F097.

[69] CERN, *Geant4 – A Simulation Toolkit*. Geant4 Website, 2019, URL https://geant4.web.cern.ch/.

[70] A. Caldwell, D. Kollár, and K. Kröninger, *BAT – The Bayesian analysis toolkit*. Computer Physics Communications, 180(11):2197 – 2209, 2009, URL http://www.sciencedirect.com/science/article/pii/S0010465509002045.

[71] The GERDA Collaboration, *Results and Post-Upgrade Performance of GERDA Phase II*. TAUP Proceedings, TAUP 2019, 2019.

[72] N. Abgrall et al., *The processing of enriched germanium for the Majorana Demonstrator and Research and Development for a next generation double-beta decay experiment*. Nuclear Instruments and Methods in Physics Research Section A: Accelerators, Spectrometers, Detectors and Associated Equipment, 877:314 – 322, 2018.

[73] N. N. I. of Standards and Technology, *Stopping Power and Range Tables for Electrons, Protons and Helium*. NIST Website, 2019, URL https://physics.nist.gov/PhysRefData/Star/Text/ESTAR.html.

[74] P. Benetti et al., *Measurement of the specific activity of 39Ar in natural argon*. Nuclear Instruments and Methods in Physics Research Section A: Accelerators, Spectrometers, Detectors and Associated Equipment, 574(1):83 – 88, 2007.

[75] N. B. Schmidt, *Results on Neutrinoless Double Beta Decay Search in GERDA: Background Modeling and Limit Setting*. PhD Thesis, Technical University of München, 2014.

[76] R. Acciarri et al., *The WArP Experiment*. Journal of Physics: Conference Series, 308:012005, jul 2011, URL https://doi.org/10.1088%2F1742-6596%2F308%2F1%2F012005.

[77] M. G. Dunford, *A Search for the Neutrinoles Double Electron Capture of 36Ar and a Measurement of the Specific Activity of 39Ar in Atmospheric Argon with the DEAP-3600 Detector*. Ph.D. thesis, Carleton U. (main), 2018.

[78] H. Loosli, *A dating method with Ar-39*. Earth and Planetary Science Letters, 63(1):51 – 62, 1983.

[79] S. I. Sukhoruchkin and Z. N. Soroko, *Atomic Mass and Nuclear Binding Energy for Ar-39*. Landolt Bornstein, 2009, URL http://nucleardata.nuclear.lu.se/toi/.

[80] G. Zuzel et al., *The DarkSide Experiment: Present Status and Future*. Journal of Physics: Conference Series, 798:012109, jan 2017.

[81] D. Akimov et al., *New method of85Kr reduction in a noble gas based low-background detector*. Journal of Instrumentation, 12(04):P04002–P04002, apr 2017, URL https://doi.org/10.1088%2F1748-0221%2F12%2F04%2Fp04002.

[82] M. Salathe, H. Crawford, R. Cooper, and D. Radford, *Inverted Coaxial HPGe Segmented Point Contact Detector*. APS Division of Nuclear Physics Meeting Abstracts, PD.002, Sep. 2016.

[83] D. Radford, *A Novel Inverted-Coaxial Point-Contact Detector*. Symposium of the Sino-German GDT Cooperation, 2013.

[84] M. The GERDA Collaboration, Agostini et al., *Supplementary Materials for: Probing Majorana neutrinos with double beta decay*. Science, 365(6460):1445–1448, 2019, https://science.sciencemag.org/content/365/6460/1445.full.pdf, URL https://science.sciencemag.org/content/sci/suppl/2019/09/04/science.aav8613.DC1/aav8613_Agostini_SM.pdf.

[85] B. Lehnert, *Search for 2νββ Excited State Transitions and HPGe Characterization for Surface Events in GERDA Phase II*. PhD Thesis, Technical University of Dresden, 2015.

[86] M. Agostini et al. (GERDA), *Production, characterization and operation of $^{76}Ge$ enriched BEGe detectors in GERDA*. Eur. Phys. J., C75(2):39, 2015, 1410.0853.

[87] GERDA collaboration et al., *Characterization of 30 $^{76}Ge$ enriched Broad Energy Ge detectors for GERDA Phase II*. arXiv e-prints, arXiv:1901.06590, Jan 2019, 1901.06590.

[88] G. A. P. Cirrone et al., *Validation of the Geant4 electromagnetic photon cross-sections for elements and compounds*. Nucl. Instrum. Meth., A618:315–322, 2010.

[89] B. B. et al., *Pulse shape analysis and position determination in segmented HPGe detectors: The AGATA detector library*. P. Eur. Phys. J. A, 52, 2016.

[90] D. Radford, *Siggen – MaGe signal simulation software*. Siggen Library, 2019, URL radware.phy.ornl.gov/MJ/mjd_siggen.

[91] K. Panas, *Development of Pulse Shape Discrimination Methods as Tools for Background Suppression in High Purity Germanium Detectors used in the* GERDA *Experiment*. PhD Thesis, Jagiellonian University in Cracow, 2018.

[92] S. Akkoyun et al., *AGATA—Advanced GAmma Tracking Array*. Nuclear Instruments and Methods in Physics Research Section A: Accelerators, Spectrometers, Detectors and Associated Equipment, 668:26 – 58, 2012.

[93] M. Salathe, *Study on modified point contact germanium detectors for low background applications*. PhD Thesis, Ruperto-Carola-University of Heidelberg, 2015.

[94] J. D. Jackson, *Classical Electrodynamics*. Wiley, New York, NY, 1975.

[95] D. M. Young, *Iterative methods for solving partial difference equations of elliptical type*. PhD Thesis, Harvard University, 1950.

[96] Mihailescu, L. et al. , *The influence of anisotropic electron drift velocity on the signal shapes of closed-end HPGe detectors*. Nucl. Instruments Methods Phys. Res., 447, 2000.

[97] M. Omar and L. Reggiani, *Drift and diffusion of charge carriers in silicon and their empirical relation to the electric field*. Solid-State Electronics, 30(7):693 – 697, 1987, URL http://www.sciencedirect.com/science/article/pii/0038110187901067.

[98] J. B. et al., *Julia – The Julia Programming Language*. Julia Homepage, 2019.

[99] G. Benato, *Data Reconstruction and Analysis for the* GERDA *experiment*. PhD Thesis, University of Zürich, 2015.

[100] L. Baudis et al., *Production and characterization of228Th calibration sources with low neutron emission for GERDA*. Journal of Instrumentation, 10(12):P12005–P12005, dec 2015, URL https://doi.org/10.1088%2F1748-0221%2F10%2F12%2Fp12005.

[101] SARAD, *Thoron Scout for radon and thoron measurements*. SARAD Products, 2019, URL www.sarad.de.

[102] L. Baudis et al., *Gator: a low-background counting facility at the Gran Sasso Underground Laboratory*. Journal of Instrumentation, 6(08):P08010–P08010, aug 2011, URL https://doi.org/10.1088%2F1748-0221%2F6%2F08%2Fp08010.

[103] E. Aprile and XENON Collaboration, *Material radioassay and selection for the XENON1T dark matter experiment*. The European Physical Journal C, 77(12):890, Dec 2017.

[104] XENON Collaboration, *Lowering the radioactivity of the photomultiplier tubes for the XENON1T dark matter experiment*. The European Physical Journal C, 75(11):546, Nov 2015.

[105] Scionix Scintillation Detectors, *LiI(Eu) Detector*. Scionix Products, 2019, URL http://www.https://scionix.nl/.

[106] E. Aprile et al. (XENON100 Collaboration), *Response of the XENON100 dark matter detector to nuclear recoils*. Phys. Rev. D, 88:012006, Jul 2013, URL https://link.aps.org/doi/10.1103/PhysRevD.88.012006.

[107] C. Wiesinger, L. Pandola, and S. Schönert, *Virtual depth by active background suppression: revisiting the cosmic muon induced background of Gerda Phase II*. The European Physical Journal C, 78(7):597, Jul 2018, URL https://doi.org/10.1140/epjc/s10052-018-6079-3.